
Multiscale Simulation Methods for Polymers



TECHNISCHE
UNIVERSITÄT
DARMSTADT

Vom Fachbereich Chemie
der Technischen Universität Darmstadt

zur Erlangung des akademischen Grades eines
Doktor rerum naturalium (Dr. rer. nat.)

genehmigte

Dissertation

vorgelegt von

Hossein Ali Karimi Varzaneh, M.Sc of Physics

aus Esfahan, Iran

Berichterstatter:	Prof. Dr. Florian Müller-Plathe
Mitberichterstatter:	Prof. Dr. Nico van der Vegt Prof. David Brown (Universite de Savoie, France)
Eingereicht am:	23.05.2011
Mündliche Prüfung am:	04.07.2011

Darmstadt 2011

D 17

Summary

Computer simulations of condensed phases and biochemical systems have led to profound new insight into molecular-scale phenomena occurring in these complex systems. Many processes that occur in liquids, soft materials, and biochemical systems however occur over length and time scales that are well beyond the current capabilities of atomic-level simulations. In the field of polymers, there are many simulation techniques and models that span a range from the atomistic scale to the continuum. In recent years, much research has been focused on linking models of different length scales, especially from detailed, fully atomistic to mesoscopic scales and back. A common way of addressing this issue is to develop coarse-grained (CG) models from full-atomistic simulations by merging groups of chemically connected atoms into superatoms. This PhD thesis describes new developments in the field of CG simulations of polymers. In addition to CG simulations, atomistic molecular dynamics calculations are performed as well to study properties of polymers. The dissertation is organized as follows.

Chapter 1 gives a review of multiscale simulation methods that have been used to study polymers and a short overview of the different topics discussed in this dissertation.

Chapter 2 introduces a new molecular dynamics simulation package that has been developed for CG simulations with numerical potentials derived by the *Iterative Boltzmann Inversion* (IBI) method [Reith, D., Pütz, M., Müller-Plathe, F. *J. Comput. Chem.* **2003**, *24*, 1624.]. In this chapter the details of the algorithms, functional details, the implementation, user interfaces and file formats are described.

A key question for all coarse-graining methodologies is the degree of transferability of the resulting force field between various systems and thermodynamic conditions. Chapter 3 presents a detailed study of the transferability of a CG force field over different thermodynamic states based on the IBI method. The polymers studied here are polystyrene and polyamide-66 whose CG models differ in the chain length and in the number of atoms forming a bead. The influence of the temperature and the pressure on static, dynamic and thermodynamic properties is tested by systematically comparing the coarse-grain results with the atomistic ones. We find that the CG model for the polystyrene is transferable only in a narrow temperature range and fails to describe the change of the bulk density when the temperature is 80 K lower than the one used in the parameter optimization. On the contrary the polyamide-66 CG model turns out to be fully transferable between different thermodynamic conditions. This is checked either by changing the temperature or the pressure of the simulation. In this

case the CG model is able to follow all intra and inter structural rearrangements which are caused by temperature changes. To come to an additional result: At low temperatures the difference between the CG and atomistic dynamics is remarkable due to the presence of hydrogen bonds in the atomistic model. At high temperatures the speedup in the CG dynamics is strongly reduced leading to a CG diffusion coefficient that is only 6 times larger than the atomistic one. We also find that the polymer chain length does not affect the transferability of the force field.

To enhance our understanding of the temperature influence on the local and global dynamics of unentangled PA-66, we study in chapter 4 the hydrogen-bond dynamics and the thermodynamics of the bulk of polyamide-66 in a broad temperature range (300 K to 600 K) by molecular dynamics simulations. Our results show that different dynamic quantities (the structure relaxation time, the orientational time correlation function of the amide groups and the self diffusion coefficient) of unentangled polyamide-66 undertake a crossover transition in the same small temperature range (~ 413 K) above the experimental glass transition temperature (350 K). The data can be fitted to a Vogel-Fulcher-Tammann law for $T > 413$ K and to an Arrhenius equation for $T < 413$ K. Our results show that the global dynamics of polyamide-66 is intimately related to the relaxation of the hydrogen-bond network of the amide groups. The presence of a dynamic crossover at a temperature slightly higher than the glass transition is in agreement with more recent experimental data and with glass theories.

In chapter 5 we give a quantitative analysis of the hydrogen-bond dynamics and the thermodynamics in the CG model of polyamide-66. It turns out that this model is characterized by a weaker HB network than the atomic one. We show that the relaxation of the HB network and the diffusion of the polymer chains are coupled. Moreover, we find that the temperature-dependent scaling factor accounting for the fast dynamics of the CG model is strongly linked to the relaxation time of the HB at each temperature. On the basis of the mesoscale model developed for polyamide-66, we present a simple algorithm for reinserting the atomistic details which are neglected in the CG description. This topic is presented in chapter 5, too. The resulting CG and fine models are tested successfully against several structural properties including the number of hydrogen bonds.

In chapter 6 we discuss another challenge in computer simulations of polymers i.e. the initial sample preparation which is still a difficult task. A technique to prepare well-equilibrated polymer melts is presented in chapter 6. The method, named fine-graining, consists of two steps: the generation of continuum random walks characterized by different Kuhn lengths and the insertion of the atomistic units into the “parent” random walk chains. The procedure ensures a good equilibration at long as well as short length-scales and it is very easy to implement. Melts of polyethylene, atactic-polystyrene and polyamide-66 are equilibrated with this technique. Their long and short range structural properties are

successfully reproduced. This follows from a comparison with previous simulations and experimental data.

Chapter 7 finally outlines some perspectives for future research.

Zusammenfassung

Computer-Simulationen von kondensierten Phasen und biochemischen Systemen haben zu einem besseren Verständnis molekularer Prozesse in diesen komplexen Materialien geführt. Leider verlaufen viele Prozesse in Flüssigkeiten, weicher Materie und biochemischen Systemen auf einer Längen- und Zeitskala, die sich nicht mehr atomar auflösen lässt. Gebräuchliche Simulationsmethoden für Polymere decken den weiten Bereich von atomaren Skalen bis zu Kontinuums-Techniken ab. In den letzten Jahren gab es viele Forschungs-Aktivitäten, solche unterschiedlichen Längenskalen miteinander zu verbinden. Besonderes Interesse fand der Übergang von einer atomaren zu einer mesoskopischen Skala und umgekehrt. Dies ist z.B. mit Hilfe sogenannter "coarse grained" (CG) Methoden möglich, bei denen mehrere Atome zu einem "Superatom" zusammengefasst werden. Schwerpunkt der vorliegenden PhD-Arbeit ist die Entwicklung neuer CG-Methoden für Polymere. Um bestimmte Eigenschaften dieser Systeme genau zu untersuchen, wurden auch Molekular-Dynamik-Simulationen in einer atomaren Skala durchgeführt. Die vorliegende Arbeit ist in insgesamt sieben Kapitel aufgeteilt. Kapitel 1 gibt einen Überblick über Multiskalen-Simulationen an Polymeren und eine kurze Beschreibung der verschiedenen Schwerpunkte dieser Arbeit.

Kapitel 2 stellt ein neues Molekular-Dynamik-Paket vor, das speziell für CG-Rechnungen auf Basis numerischer Potenziale entwickelt wurde. Als Werkzeug wurde dabei das iterative Boltzmann-Inversions-Verfahren (IBI) verwendet. [Reith, D., Pütz, M., Müller-Plathe, F., *J. Comput. Chem.* **2003**, 24, 1624]. Sowohl die theoretischen Details dieser Methode als auch die Benutzer-Oberflächen und Formatierungen werden hier beschrieben. Entscheidend für den Erfolg von CG-Verfahren ist ihre Übertragbarkeit auf verschiedene Systeme und thermodynamische Bedingungen. Kapitel 3 gibt einen detaillierten Einblick in die Übertragbarkeit von CG-Kraftfeldern auf unterschiedliche thermodynamische Zustände. Die hier durchgeführten Rechnungen basieren auf der IBI Methode. Im Rahmen dieser Arbeit wurden Polystyrol und Polyamid-66 untersucht. Die CG-Ansätze beider Polymere unterscheiden sich sowohl in der Kettenlänge als auch in der Anzahl von Atomen in einer CG-Einheit. Atomare und CG-Simulationen wurden parallel durchgeführt, um den Einfluß der Temperatur und des Druckes auf statische, dynamische und thermodynamische Eigenschaften zu untersuchen. Dabei konnten wir zeigen, dass das für Polystyrol entwickelte CG-Modell nur innerhalb eines kleinen Temperaturbereichs übertragbar ist. Es versagt bei der Beschreibung der Änderung der Dichte, sobald die Simulationstemperatur mehr als 80 K kleiner ist als die Temperatur der Parameter-Optimierung. Im Gegensatz dazu lässt sich das CG-Modell für Polyamid-66 problemlos auf geänderte thermodynamische Bedingungen übertragen. Dies wurde sowohl für Temperatur- als auch

Druckänderungen gezeigt. Bei diesem Polymer konnte das CG-Modell Temperatur-abhängigen strukturellen Änderungen folgen. Anders verhält es sich im Fall des Diffusionskoeffizienten. Bei tiefen Temperaturen unterscheiden sich die atomare und die CG-Dynamik sehr stark. Verursacht wird dies durch die Wasserstoff-Brückenbindungen in der atomaren Simulation. Bei höheren Temperaturen ist die CG-Diffusion nur noch sechsmal schneller als die atomare. Unsere Untersuchungen haben gezeigt, dass die Länge der Polymerketten keinen Einfluß auf die Übertragbarkeit der Kraftfeld-Parameter hat.

In Kapitel 4 untersuchen wir die Dynamik und Thermodynamik der “Bulk“ Phase von Polyamid-66 in einem größeren Temperaturbereich (300 - 600 K) mithilfe von Molekular-Dynamik-Simulationen. Diese Untersuchungen sollen zu einem besseren Verständnis der lokalen und globalen Dynamik in nicht-verschlaufem PA-66 führen. Wir zeigen, dass unterschiedliche dynamische Eigenschaften (strukturelle Relaxationszeit, die Korrelationsfunktion für die Orientierung der Amid-Gruppen und der Selbst-Diffusionskoeffizient) von nicht-verschlaufem Polyamid-66 einen Phasenübergang in einem engen gemeinsamen Temperaturbereich (≈ 413 K) nahe legen. Diese Temperatur liegt ca. 60 Grad oberhalb der Glas-Temperatur von 350 K. Für $T > 413$ K können die Daten an das Vogel-Fulcher-Teichmann-Gesetz angefügt werden. Für $T < 413$ K folgen die Daten einem Arrhenius-Verlauf. Unsere Untersuchungen belegen, dass die globale Dynamik von Polyamid-66 eng mit der Relaxation der Wasserstoff-Brücken der Amid-Gruppen verbunden ist. Dieser dynamische Übergang bei einer Temperatur oberhalb des Glasübergangs stimmt sowohl mit neueren Experimenten als auch mit theoretischen Ansätzen für Gläser überein.

In Kapitel 6 geben wir eine quantitative Analyse der Dynamik der H-Brücken und der Thermodynamik von Polyamid-66 im Rahmen einer CG-Beschreibung. Die H-Brücken-Bindungen in diesem Modell sind schwächer als im Fall einer atomaren Beschreibung. Darüberhinaus zeigen wir, dass die Relaxation der H-Brückenbindungen und die Diffusion der Polymerketten gekoppelt ist. Wir haben ebenfalls gefunden, dass die Temperatur-abhängige Skalierung zur Berücksichtigung der schnellen Dynamik im CG-Modell bei jeder Temperatur stark an die Relaxationszeit der H-Brücken gekoppelt ist. Auf Basis eines mesoskopischen Modells für Polyamid-66 schlagen wir ein einfaches Verfahren für die Wiedereinführung atomarer Details vor, die in der CG-Beschreibung nicht berücksichtigt wurden. Dieses Thema wird ebenfalls in Kapitel 5 vorgestellt. Die entwickelten CG- und atomaren Modelle konnten erfolgreich an strukturellen Eigenschaften, z.B. der Anzahl der H-Brücken, getestet werden.

Kapitel 6 behandelt eine andere Herausforderung von Polymer-Simulationen, der Erzeugung einer relaxierten Startkonfiguration. Ein Ansatz dafür wird in diesem Kapitel beschrieben. Die vorgestellte Methode erfordert zwei Schritte. i.) Der Erzeugung von kontinuierlichen

Zerfallsbewegungen, die durch unterschiedliche Kuhn-Längen charakterisiert sind und ii.) dem Einsetzen der atomaren Fragmente in die Ausgangs-Ketten für diese Zufallbewegungen. Der vorgestellte Ansatz ermöglicht eine effiziente Relaxation sowohl für lange als auch kurze Zeit-Skalen und ist einfach zu implementieren. Schmelzen von Polyethylen, der ataktischen Phase von Polystyrol und Polyamid-66 werden mit diesem Ansatz equilibriert. Die Reproduktion ihrer lang- und kurzreichweitigen strukturellen Eigenschaften gelingt erfolgreich. Dies wird durch den Vergleich mit publizierten Simulationsdaten und Experimenten belegt.

Die Arbeit endet mit Kapitel 7, in dem mögliche Richtungen für zukünftige Arbeiten angeregt werden.

Summary	I
Zusammenfassung	IV
1. Introduction	10
1.1 Multiscale Simulation Methods for Polymers	10
1.2 Coarse-Grained Simulations: New Developments and Applications	16
1.3 Research Background	20
1.3.1 The Iterative Boltzmann Inversion Method	20
1.4 References.....	22
2. IBIsCO: A Molecular Dynamics Simulation Package for Coarse-Grained Simulation	25
2.1. Introduction	25
2.2. Molecular Dynamics Algorithms and Functionalities of IBIsCO	26
2.2.1. Force Field	26
2.2.2. Construction of Non-Bonded Interaction Neighbor List.....	28
2.2.3. Integration Schemes for the Equations of Motion.....	29
2.2.3.1. Leapfrog Scheme	29
2.2.3.2. Dissipative Particle Dynamics	30
2.2.3.3. Lowe-Andersen Scheme	31
2.2.4. Berendsen’s Thermostat and Barostat.....	32
2.2.5. Reverse Non-Equilibrium Molecular Dynamics (RNEMD).....	33
2.3. Parallelization Strategy	35
2.4. Interfaces and File Formats.....	36
2.4.1. Units.....	36
2.4.2. Input Files	37
2.4.3. Output Files.....	44
2.6. Summary	46
2.7. References.....	47
3. Transferability of Coarse-Grained Force Fields: The Polymer Case	48
3.1. Introduction.....	48
3.2. Mesoscale Models and Simulation Details	49
3.3. Results and Discussion	51
3.3.1. Force Field: Bond Potential and Intramolecular Distributions.....	51
3.3.2. Force Field: Nonbonded Interactions and Interchain Distributions	53
3.3.3. Static Properties	55
3.3.4. Dynamic Properties	59
3.3.5. Density Dependence of the Force Field	62
3.4. Conclusions.....	63
3.5. References.....	66
4. Hydrogen Bonding and Dynamic Crossover in Polyamide-66: A Molecular Dynamics Simulation Study	67
4.1. Introduction.....	67

4.2. Model and Simulation Details	69
4.3. Results and Discussion	71
4.3.1. Static Properties of Hydrogen Bonds	71
4.3.2. Dynamic Properties of Hydrogen Bonds.....	74
4.4 Conclusions.....	82
4.5. References.....	83
5. Fast Dynamics in Coarse-Grained Polymer Models: The Effect of the Hydrogen Bonds.....	85
5.1. Introduction.....	85
5.2. Coarse-Grained Model.....	86
5.3. Back-Mapping Procedure	88
5.4. Results and Discussion	91
5.4.1. Validation of the Back-Mapping Procedure.....	91
5.4.2. Chain Stiffness	94
5.4.3. Hydrogen Bond Analysis	96
5.5. Conclusions.....	101
5.6. References.....	103
6. Fine-Graining Without Coarse-Craining: An Easy and Fast Way to Equilibrate Dense Polymer Melts.....	105
6.1. Introduction.....	105
6.2. Computational Method	107
6.2.1. Continuum Random Walk.....	107
6.2.2. Reverse Mapping	108
6.2.3. Simulation Parameters	110
6.3. Results and Discussion	111
6.3.1. Polyethylene.....	111
6.3.2. Atactic-Polystyrene	116
6.3.3. Polyamide-66	122
6.4. Conclusions.....	125
6.5 References.....	127
7. Outlook.....	129
7.1. References.....	132
Appendix 1.....	133
Simulation Tools.....	136
Publications	137
Acknowledgements	138
Curriculum Vitae.....	139
Erklärung.....	140



Eidesstattliche Erklärung.....141

1. Introduction

1.1 Multiscale Simulation Methods for Polymers

Polymeric systems are characterized by a wide range of length scales that extend from Ångströms for the distance between the bonded atoms to at least the contour length of the chain on the order of micrometers. The corresponding time scales associated with motions on such length scales are even broader; bond vibrations occur on the scale of picoseconds (10⁻¹³ second) and chain relaxation and morphology formation can occur over seconds, minutes, or hours, depending on molecular weight, temperature and density. For this reason, an equally wide range of simulation methods at different levels of resolution and consequently including a different amount of degrees of freedom is employed to study them.¹

Quantum mechanical (QM) methods present the most detailed picture of the system by using different levels of approximations to solve the Schrödinger equation. A work by Martonak et al.² showed that even at room temperature, quantum effects are crucial to understanding the anisotropic thermal expansion of polyethylene crystals. The QM methods can be used only for very small length and time scales. However, they are extremely valuable to provide interaction energies etc. as parameters for interaction functions in classical simulation methods. Molecular dynamics (MD) simulation is a powerful technique for computing the equilibrium and dynamical properties of classical many-body systems.³ Over the last twenty years with rapid development of computers, polymeric systems have been the subject of intense study with MD simulations, but MD simulations using atomistic force fields are still unable to access the time scales necessary to achieve chain relaxation for polymeric systems of intermediate or high molecular weights.⁴ To equilibrate the dense polymeric systems with long chains advanced Monte Carlo (MC) methods have been developed.^{3,5} Nevertheless, the size of the systems that can be efficiently simulated is still limited by the performance of present-day computers.

In order to study polymeric systems, particularly their ability to self-assemble over tens or hundreds of nanometers, it is necessary to reduce the number of degrees of freedom. Simple generic models (such as bead-and-spring or lattice models) are found to be suitable to study scaling properties of macromolecular systems by reducing the computational complexity to the absolute minimum, namely connectivity and excluded volume plus some specific interactions, if needed.⁴⁻⁶ The bead-

spring models⁶ are the most elementary MD models where the individual polymer chain is modeled by mass points which repel each other to produce the excluded volume interaction, and they are connected along the chain by a spring to take care of the connectivity. These models have been used frequently to study the dynamics of short and long-chain polymer melts as well as relaxation properties of elastomers, i.e. cross linked polymer melts.^{7,8} However, for the complete understanding of polymer properties (such as viscosity or crystallization) both generic chain length and connectivity information and detailed material-specific information of the chemical composition are necessary. One approach to attain this goal is the development of “systematically coarse-grained” models, which can be used to predict the quantities for a specific material. The coarse-grained (CG) models allow an extremely simplified picture and interpretation of complex molecular phenomena by averaging over unessential atomic details. These models are obtained by lumping groups of chemically connected atoms into “superatoms” and deriving the effective CG interaction potentials from the microscopic details of the atomistic models. The mapping scheme relates the atomistic coordinates of a structure to the bead positions in the CG model. It is clear that there is no unique way to map a given set of atoms onto a coarser description. However, depending on the specific system and on the properties of the system that one wants to see reflected on the coarse level, one can define criteria to determine mapping points.

The developments of system-specific CG models for polymers is a very active research field, and depending on the way the effective CG potentials are derived and also on the degree of coarse-graining, various models and methods have been proposed in the literature.⁹⁻²⁸ One way to develop a CG models is using a structure based coarse-graining approach, where the direct link to the chemistry is achieved through structurally defined bonded and non-bonded effective CG potentials derived from the atomistic model. In this class of methods, the determination of interaction potentials for the CG model is based on the assumption that the total potential energy can be separated into bonded and non-bonded contributions. The bonded interactions derived such that the conformational statistics of a single molecule is represented correctly in the CG model. A very important criterion for a mapping scheme is its ability to decouple internal degrees of freedom so that the intramolecular (bonded) potentials can be separated into bond, angle and torsion terms. One option to derive the CG bonded potentials is to use the Boltzmann inversion to convert the distributions of interparticle distances or angles into the potentials. Another option is to determine analytical potentials that reproduce the probability distributions for the bonded part, for example by fitting the (multi-peaked) bonded distributions by a series of Gaussian functions which can then be inverted analytically resulting in smooth potentials and forces.²⁹ Similar to the bonded interaction functions, one has two options to derive the non-bonded potentials: either (1) to use analytical potentials and optimize the parameters of

a chosen analytical function by using a simplex algorithm^{30,31} to reproduce the structure of the atomistic system as accurately as possible;³² or (2) to use numerically derived tabulated potentials, which are designed such that the CG model reproduces the atomistic structure. In the first case, analytical potentials of various types can be used: the “normal” Lennard–Jones 12-6 potential is frequently used which is sometimes too repulsive for the CG soft beads,^{28,33} and for softer cases Lennard–Jones-type (e.g., 9-6 or 7-6),^{34,35} Buckingham or Morse potentials³⁶ are employed. However, slow convergence of the analytical potentials and the manual process of selecting a good functional form of the potential are disadvantages of this method.

Concerning the second option to generate numerically a tabulated potential that closely reproduces a given melt structure, the iterative Boltzmann inversion (IBI) method^{11,25,37} has been developed. The main feature of the method is the automatic and iterative way to determine the effective bead-bead interactions that match a set of structural quantities (such as intermolecular radial distribution functions, RDFs) calculated from a more detailed reference simulation model (i.e. atomistic). Henderson³⁸ proved that at a given density and temperature, there is a unique mapping between the radial distribution function and the intermolecular potential. Thus, a potential which reproduces the target RDF is a fixed point of the iteration and, if the algorithm converges, a valid solution for CG potential is obtained (for more details see the section **3.1. Research Background**). However, there can be limits to this approach because it is not always clear whether the chosen CG mapping scheme can converge to an optimal fit. According to the workflow to develop the CG force fields presented here one obtains potentials for bonded and non-bonded interactions at the same time based on the same atomistic simulation, thus there is no clear separation between the optimisation procedures for bonded and non-bonded interaction potentials. One can achieve this separation by deriving CG bond length, bond angle, and torsional distributions from the atomically detailed conformations sampled by a single (chain) molecule in vacuo, if the conformational sampling of the molecule in vacuo and in the bulk (or solution) phase does not differ substantially.³⁶ The IBI method has been used successfully for molecular liquids,³⁹ polymer melts,^{19,21,40} dendrimers,⁴¹ polymer solutions³⁹, polymer blends⁴² and ionic liquids.⁴³

The IBI method has the advantage that detailed structural information is included into the CG model. Since the radial distribution function incorporates temperature, density, composition, and other dependencies into the effective pair interaction, the resulting force field can have a severely limited range of applicability, and transferability of the CG force field is still a challenge.^{19,39} In chapter 3 we will discuss more about the transferability of CG force fields developed by IBI method.

Investigations of dynamic properties such as mean-squared displacement, diffusion constant, and Rouse-mode analysis necessitate the transition from unentangled to entangled motion for IBI force fields, and it turns out that such structure-based CG potentials can be used for a *qualitative* study of the dynamics of polymer systems.^{6,18} However, since many of the original degrees of freedom are removed in the CG description, the effective CG potentials are softer compare to the atomistic ones, and this results in a reduced effective friction between the beads. Thus, CG simulations cannot be used directly for a *quantitative* study of the dynamics. Of course, the three basic unit scales (particle mass, size, and energy scale) define a time scale in MD simulation of the CG systems, but the time in the CG description does not correspond to the real physical time of the underlying chemistry. One of the main problems of such CG models is the artificial dynamics, which is too fast compared to the reference systems.^{19,44} To re-establish the correct dynamics in CG simulations, different approaches have been proposed. Izvekov and Voth⁴⁵ proposed an approach within the coarse-graining framework of force matching (see below) which reproduce a correct dynamic in the CG simulation. However, in order to map the time accurately between the atomistic and the structure-based CG model one can use one of the following two methods: the first is to gauge the CG dynamics by equating a scalar dynamical quantity like the diffusion coefficient or the viscosity.^{19,44} The results of the CG model could thus be matched to the value from long atomistic MD runs or experiments. By doing this, only the asymptotic long time regime is being compared, and one hopes that one time-scaling factor covers all dynamical processes. In the case that we do have data from atomistic MD simulations, an alternative way to map the time is to match the mean-square displacement (MSD) of the monomers.^{21,40,46} The time scaling factor determines the real unit to which the CG time corresponds.

With the goal of providing a systematic multiscale approach to coarse-graining, Izvekov and Voth have introduced the multiscale coarse-graining (MS-CG) method (force matching method).^{47,48} In this method, the forces in the CG system are determined such that they are mapped to the sum of the forces in the corresponding atomistic system.⁴⁹⁻⁵¹ The MS-CG method has been applied to develop accurate CG models for peptides,^{52,53} pure bilayers,⁴⁷ mixed bilayers,⁵⁴ carbohydrates,⁵² simple fluids,^{45,48} ionic liquids,^{55,56} soot nanoparticles,⁵⁷ and even mixed- resolution models of transmembrane proteins.⁵⁸ The MS-CG theory can also serve as a basis for achieving more correct dynamical behavior (e.g., self-diffusion) in the CG model.⁴⁵ If no approximations are introduced into the method, the MS-CG variational principle provides a computational algorithm for determining the many-body CG free energy surface for a given atomically detailed model. The bonded parameters of the potentials developed by MS-CG method are found to be transferable to different temperatures, while the non-

bonded potentials are less. However, the MS-CG models are well transferable to different system sizes.⁵⁵

Concerning the different methods to obtain the interaction potentials between the CG beads the MARTINI force field in close connection with atomistic models has been developed; its philosophy of the coarse-graining approach is slightly different than the other methods.^{14,59} Instead of focusing on an accurate reproduction of structural details at a particular state point for a specific system, the aim is for a broader range of applications without the need to reparameterize the model each time by extensive calibration of the chemical building blocks of the CG force field against thermodynamic data. Currently, the MARTINI force field provides parameters for a variety of biomolecules, including many different lipids, cholesterol, and all amino acids. Properties accurately reproduced include structural,^{14,60,61} elastic,^{14,59} dynamic,¹⁴ and thermodynamic data.^{59,61,62} In order to parameterize the non-bonded interactions of the CG model, a systematic comparison to experimental thermodynamic data has been performed. Specifically, the free energy of hydration, the free energy of vaporization, and the partitioning free energies between water and a number of organic phases were calculated for each of the different CG particle types. To parameterize the bonded interactions, it uses structural data that are either directly derived from the underlying atomistic structure (such as bond lengths of rigid structures) or obtained from comparison to fine-grained simulations. In the latter procedure, the fine-grained simulations are first converted into a “mapped” CG simulation by identifying the center of mass of the corresponding atoms as the mapped CG bead. Second, the distribution functions are calculated for the mapped simulation and compared to those obtained from a true CG simulation. Subsequently the CG parameters are systematically changed until satisfactory overlap of the distribution functions is obtained. The potential range of applications of the CG model is very broad. There are, however, certain important limitations that should be kept in mind. For example, the model has been parameterized for the fluid phase. Thus properties of solids, such as crystal packing, are not expected to be accurate. In the other hand, both the gas and the solid phase appear somewhat too stable with respect to the fluid phase, and therefore the thermodynamic behavior of solid/fluid and gas/fluid interfaces should be interpreted with care, at least at the quantitative level.

An alternative way to develop a CG force field is a starting from dynamic properties of the system. In this case the Langevin-equation formalism^{6,63} is used to describe the dynamic evolution of the system, and the friction coefficients that partially slow down the dynamics, are determined from atomistic reference simulations using force-velocity and velocity-velocity correlation functions.^{16,45} This method is usually used to study complex liquids⁶⁴ or bio-systems.⁵⁴ In the same class of method fall also those that tune the friction coefficients until the dynamic properties match the atomistic

ones.¹⁵ In any case it is of interest to understand the physical origins of the acceleration of the CG dynamics for specific cases, to assess the methods mentioned above and gain a better understanding of the effect of coarse-graining on the dynamics of a system. However, this class of method could fail to reproduce the structure of the system.

There is currently much research being carried out to investigate, whether it is possible to derive coarse grained potentials that are both thermodynamically as well as structurally consistent with the underlying higher-resolution description. In recent work of Qian et al.⁶⁵ the dissipative particle dynamics⁶⁶ (DPD) and Lowe-Anderson⁶⁷ (LA) equation of motion have been applied in CG simulations to slow down the dynamics of the CG model obtained through IBI method. The simulation results showed that both DPD and LA can re-introduce friction into the system and compensate for the dynamical effects of coarse graining. Thus, the too fast dynamics of CG models in molecular dynamics can be corrected and can be slowed down to match reality. Empirical rules have been found for the control parameters (noise strength in DPD and bath collision frequency in LA) in CG simulation of liquid ethylbenzene⁶⁵. Further work needs to be done to establish how transferable these rules are among different systems.

The different simulation hierarchies (QM, atomistic MD and CG simulations) can be used to address phenomena or properties of a given system at several levels of resolution and consequently on several time and length scales. The easiest way to combine different simulation models on different scales is to treat them separately and sequentially by simply passing information (structures, parameters, energies etc.) from one level of resolution to the next. A step beyond these sequential schemes is represented by those approaches where the scales are coupled in a concurrent fashion within a unified computational scheme. In these approaches two levels of resolution are used at the same time in the simulation. A dual-scale approach already has been used to study the interaction between bisphenol-A-polycarbonate and a nickel surface.^{68,69} In this method, the regions with different resolutions are fixed and the exchange of particles among the different regions is not allowed. While this may not be a crucial point for hard matter, is certainly a strong limitation for soft matter, i.e. complex fluids, since relevant density fluctuations are arbitrary. An even more sophisticated multiscale approach allows to adaptively switch between resolution levels for individual molecules on the fly – for example depending on their spatial coordinates. Recently, such an adaptive resolution scheme (AdResS) has been developed in which molecules can freely exchange between a high-resolution and low-resolution region.⁷⁰⁻⁷² This very recent method, which so far has been used for liquid water⁷¹ and a polymer-solvent system,⁷² is of great interest in a much wider variety of systems.

The combination of CG simulation with an efficient back-mapping methodology (i.e. reintroduction of atomistic detail) is a powerful tool to efficiently simulate long time-scale and large length-scale processes in soft matter where in the end one can obtain well-equilibrated atomistic structures. The resulting structures can be directly compared to experimental data or they can be used in further computations, for example to determine dynamic data (e.g. the permeabilities of small molecules in large polymeric systems). Additionally, the combination of CG simulations, where the CG model is based on an underlying atomistic description, with a back-mapping procedure can be further employed to validate the atomistic force field on time and length scales not accessible to atomistic simulations. In general the back-mapping procedure has no unique solution since every CG structure corresponds to an ensemble of atomistic microstates. Therefore, one needs to find one representative all-atom structure, with the correct statistical weight of those degrees of freedom that are not resolved in the CG description. Several slightly different strategies to reintroduce atomistic detail into a CG structure have been presented.^{7,73,74} The general strategy is to use reasonably rigid all-atom chain fragments – corresponding to a single or a small set of CG beads – which were taken from a correctly sampled distribution of all-atom chain structures. An alternative way in the case of more flexible low-molecular weight molecules could be the restraining atomistic coordinates into the CG structure to avoid the atomistic structure to deviate too strongly from the CG reference. The back-mapping strategy will be explained in more details in chapter 5 for a CG model of polyamide-66.

The key motivation for CG molecular modeling and simulation thus primarily derives from the need to bridge the atomistic and mesoscopic scales. Typically, there are two to three orders-of-magnitude in length and time separating these regimes. At the mesoscopic scale, one sees the emergence of important phenomena (e.g., self-assembly in biomolecular or soft matter systems). CG simulations, especially as they seek to make increasing contact with experimental results on complex systems, can therefore play a significant role in the exploration of mesoscopic phenomena and, in turn, of the behavior of real biomolecular and materials systems. The emerging challenges to the CG approach and possible future developments of this field will be discussed in chapter 7.

1.2 Coarse-Grained Simulations: New Developments and Applications

This PhD thesis describes several new developments of coarse-grained models and their applications in the computer simulations of polymers. Firstly, the current coarse-graining strategy, iterative Boltzmann inversion (IBI) and the corresponding workflow have been implemented into a new program package IBISCO, which is especially tailored to CG simulations. Secondly, this thesis

addresses the problem of model transferability, i.e. if and how far can a coarse-grained model developed at one thermodynamic state (temperature, pressure, composition) be used at another state. This is analysed for the examples of two different polymers, polyamide-66 and atactic polystyrene. With this validation of the CG approach completed, the CG model was, thirdly, employed to study the effects of hydrogen bonds on the long-time dynamics of polyamide-66. Finally, we developed and tested a new method “fine-graining without coarse-graining” for the preparation of atomistic conformations directly from random walks, i.e. without a preceding simulation of a coarse-grained model. This “backmapping” strategy is directed at future simulations where one is only interested in a relaxed atomistic conformation for further analysis, but not in the long-range properties of the polymer itself. In the next paragraphs, we give a short overview for each part.

Based on the CG simulations which have been performed in our group, and in order to validate the workflow of developing CG models using the IBI method, we feel the need to provide a detailed description of the IBIsCO code, which is a program package specially developed for CG simulations using Gaussian potential functions and/or tabulated interaction potentials derived by the IBI approach. Various standard ensembles (*NVT*, *NPT*, and *NVE*) are available in IBIsCO. The techniques of dissipative particle dynamics⁶⁶ (DPD) and Lowe-Andersen⁶⁷ (LA) equations of motion are also embedded in IBIsCO. Besides their use as thermostats for the generation of a canonical ensemble, DPD and LA can also be used as techniques to compensate the effects of lost degrees of freedom in CG models on the dynamics: they slow down the too fast dynamics in CG models due to the softness and the lack of friction.⁶⁵ Chapter 2 describes the basic MD algorithms, the capabilities and usage of IBIsCO.

A key question in the CG simulations is the degree of transferability of the resulting coarse-grained force fields between various molecular systems and different thermodynamic conditions (temperature, pressure, concentration). Intrinsicly, the coarse-grained force field cannot be rigorously transferable because, by removing the atomistic detail, the interactions between particles in the system have been averaged out in ways that are different depending on the given conditions. In other words, the effect of removing the same degrees of freedom can be, and generally is, different at different temperatures, densities or environments. In Chapter 3, we focus on a the IBI coarse-graining method, which has been successfully applied to a wide range of macromolecular systems.^{12,20,33,41,75} The purpose is to test whether the IBI-generated CG force field developed at one set of condition is specific to these conditions, or whether it can be transferred to other situations and over what range. The transferability is an important point in the CG simulations because, if in practice, it is given over a

certain range the computational effort for the necessary atomistic reference simulations would be considerably reduced.

The amorphous polymers studied here are two common synthetic polymers: atactic polystyrene (a-PS) and polyamide-66 (PA-66). They are modelled by different degrees of coarse-graining and have different chain lengths. The effect of temperature and pressure on static, dynamic and thermodynamic properties is tested by comparing systematically the coarse-grained results with the atomistic ones. We find that the CG model describing the a-PS is transferable only in a narrow range of temperature and it fails in describing the bulk density when the temperature is 80 K lower than the one where it was optimised. On the contrary, the PA-66 CG model turns out to be fully transferable between different thermodynamic conditions (temperature range of 300-600K). The transferability is checked for both temperature and pressure variations. We find that, in this case, the CG model is able to follow all the intra and inter structural rearrangements caused by the temperature changes.

A second CG model for a-PS (different mapping scheme), proposed later by Qian et al.³⁹, shows to be transferable over different temperatures and different chain lengths. These results show that the transferability of the CG force field developed by the IBI method depends strangely on the location of the superatom within the real monomer, the number of degrees of freedom removed during the CG procedure and the polymer under investigation.

Concerning the transferability of CG force field for polyamide-66 to different temperatures, we explore different thermodynamic and structural properties of the system at different temperatures. The hydrogen bonding (HB) is one of the intermolecular interactions that most influences the dynamics of molecular systems, being responsible for the structure, function, and dynamics of many chemical systems from inorganic to biological compounds.⁷⁶ Due to the simplification of the coarse-grained models, the atoms directly involved in the HB (oxygen, nitrogen or fluorine as hydrogen bond donors and acceptors) as well as the hydrogen atom itself are usually “coarse-grained away”, i.e. lumped together with other atoms into beads. Several models have been developed to describe HB especially in studying protein folding⁷⁷ and have met with different success. Similar types of study have not been carried out for synthetic macromolecules although also in their case the presence of the HBs affects strongly their conformation, chemical-physical properties, crystallization, self-assembly behaviour and many other global properties. It is therefore particularly interesting to see whether and how the features owed to the hydrogen bonds are preserved in the CG model, in which they are only present in an effective and averaged way. In addition, the possibility of correctly describing the HB dynamics using a CG model would be of great importance for further improvements of CG force fields.

In polyamides, nearly all the amide groups, that are separated by a sequence of methylene groups, are hydrogen-bonded.⁷⁸ The large number of hydrogen bonds forms an extended three-dimensional network whose dynamic rearrangement influences several properties of the material such as the glass transition temperature and the melting point. For these reasons, understanding the thermal mechanical properties of polyamides by studying the thermal stability of hydrogen bonds has been a popular topic in previous research.⁷⁸⁻⁸² In Chapter 4, we first analyze in detail the effect of temperature on the local and global dynamics of unentangled PA-66 using atomistic molecular dynamics simulations. The local dynamics is mainly investigated by looking at the HB dynamics and calculating the hydrogen-bond relaxation time and lifetime by means of specific correlation functions. The influence of the relaxation of the HB network on the global dynamics of the polymer is also analyzed. Our results show that the global dynamics of polyamide-66 is intimately related to the relaxation of the hydrogen-bond network formed among the amide groups. Then, in chapter 5 we study a CG model of the same PA-66 system focusing on the dynamics (and thermodynamics) of the HB. The ability of the CG model to capture correctly the dynamics of the hydrogen-bond network at different temperatures is tested. To address this issue we use the same correlation functions which have been employed in the analysis of hydrogen bond dynamics in atomistic simulations. From a quantitative analysis of the hydrogen bonds dynamics and thermodynamics it turns out that the CG model is characterized by a weaker HB network than the corresponding atomic model. We show that the relaxation of the HB network and the diffusion of the polymer chains are coupled. Moreover, we find that the temperature-dependent scaling factor, which accounts for the fast dynamics of the CG model, is strongly linked to the relaxation time of the HB at each temperature.

Many features of polymers including their viscoelastic behavior depend on the fact that the monomers are bonded together and form a specific topology. The chain connectivity makes the conformational space to be sampled very broad and characterized by a complex energy landscape. Therefore, specific simulation techniques must be developed in order to efficiently explore the conformation space and to gain information about the structure and dynamics of a polymer melt, avoiding the system being trapped in the neighborhood of the initial configuration.

Chapter 6 presents a new and easy procedure to quickly equilibrate entangled linear polymers. The method proposes the use of a reverse-mapping (or fine graining) technique to generate an atomistic polymer structure directly from a generic polymer model. This method (here called “fine-graining”) requires only two steps: the generation of a random walk (representing the average conformational state of a generic polymer chain in a melt) and the subsequent insertion of the atomistic details following the trace of the random walk. After inserting the missing atoms into the generic

polymer structure, few simulation steps are further required to re-form backbone bonds among the monomers and to relax (locally) the newly formed atomic polymer chains. The method is applied to three types of amorphous polymer melts: polyethylene (PE), atactic polystyrene (a-PS) and polyamide-66 (PA-66). Results of global properties (radius of gyration, end-to-end distance, radial distribution functions) and local structure (distribution of dihedral angles, local reorientation of bonds) can be successfully compared with those obtained from other methods presented in literature and with experimental data. The procedure ensures a good equilibration at long as well as short length-scales and is very easy to implement.

Chapter 7 closes this thesis with an outlook on the future development of the molecular dynamics and coarse-grained simulations of polymers.

1.3 Research Background

1.3.1 The Iterative Boltzmann Inversion Method

Since all the coarse-grained (CG) potentials presented in this thesis are developed on the basis of the iterative Boltzmann inversion (IBI) method, we briefly explain this strategy in this section. The first assumption is that the total potential energy U^{CG} can be separated into bonded/covalent and non-bonded contributions

$$U^{CG} = \sum U_b^{CG} + \sum U_{nb}^{CG} \quad (1-1)$$

where U_b^{CG} and U_{nb}^{CG} represent the bonded and non-bonded part of the potential, respectively.

The bonded interactions are derived such that the conformational distribution P^{CG} , which is characterized by specific CG bond lengths r between adjacent pairs of CG beads, angles θ between neighbouring triplets of beads and torsions φ between neighbouring quadruplet of beads respectively, i.e. $P^{CG}(r, \theta, \varphi)$, in the CG simulation is reproduced. If one assumes that the different internal CG degrees of freedom are uncorrelated, $P^{CG}(r, \theta, \varphi)$ factorizes into independent probability distributions of bond, angle and torsional degrees of freedom

$$P^{CG}(r, \theta, \varphi) = P^{CG}(r)P^{CG}(\theta)P^{CG}(\varphi) \quad (1-2)$$

To obtain the bonded potentials, the individual distributions $P^{CG}(r)$, $P^{CG}(\theta)$ and $P^{CG}(\varphi)$ are first fitted by a suitable sum of Gaussians functions and then Boltzmann inverted. It should be noted that the bond length and bond angle probability distributions are normalized by taking into account of the corresponding metric, namely r^2 for bond lengths and $\sin(\theta)$ for bending angles. Probably due to

the stiffness of the bonded interactions, this direct Boltzmann inversion of the atomistic distributions gives CG potentials, which lead to CG distributions matching the atomistic ones.

Non-bonded interactions are derived as effective non-bonded potentials $U_{nb}^{CG}(r)$ from a given target intermolecular radial distribution function (RDF) $g^{target}(r)$ obtained from atomistic reference simulations or experimental data. First a reasonable initial guess is needed. It can be obtained by directly Boltzmann-inverting the RDF (which is a probability distribution):

$$F(r) = -k_B T \ln g^{target}(r) \quad (1-3)$$

It is important to notice that $F(r)$ is a free energy and not a potential energy. However, it is usually sufficient as an initial guess, $U_{nb,0}^{CG}(r)$, for the iterative procedure. Simulating the system with $U_{nb,0}^{CG}(r)$ now yields a corresponding RDF $g_0^{CG}(r)$, which is different from the $g^{target}(r)$. Therefore, the CG potential needs to be improved, and this can be done by adding to $U_{nb,0}^{CG}(r)$ a correction term $-k_B T \ln[g_0^{CG}(r)/g^{target}(r)]$. This step is iterated

$$U_{nb,i+1}^{CG}(r) = U_{nb,i}^{CG}(r) + k_B T \ln \left(\frac{g_i^{CG}(r)}{g^{target}(r)} \right) \quad (1-4)$$

until the reference $g^{target}(r)$ is reproduced and the potential is stationary, $U_{nb,i+1}^{CG}(r) = U_{nb,i}^{CG}(r)$. The convergence can be measured quantitatively by evaluating the following error function:

$$f_{target} = \int w(r) (g_i^{CG}(r) - g^{target}(r))^2 dr \quad (1-5)$$

where $w(r) = \exp(-r/\sigma)$ is a weighting function to penalize more strongly deviations at small distances.

Since the IBI method, eq 1-3, has no obvious way in which the system energy or pressure influence the value of the potential at a particular distance, the following approach can be used to add this information. Adding to the non-bonded potential a weak linear potential term ΔV , which goes to zero at the cutoff and whose slope is positive or negative (V_0), does not change significantly the RDFs produced by the model, but changes the pressure down or up, respectively. The so-called ramp correction is of the form

$$\Delta V = V_0 \left(1 - \frac{r}{r_{cutoff}} \right) \quad (1-6)$$

This correction can be inserted into the Boltzmann-inversion iterations, to adjust the pressure to the target value.

1.4 References

- (1) Kremer, K. *In Proceedings of the International School of Solid State Physics - 34th Course: Computer Simulations in Condensed Matter: from Materials to Chemical Biology*, Binder, K.; Ciccoti, G. ed.; Erice, 2006.
- (2) Martonak, R.; Paul, W.; Binder, K. *J. Chem. Phys.* **1997**, *106*, 8918.
- (3) Harmandaris, V. A., Mavrantzas, V. G., *Molecular Dynamic Simulations of Polymers. In Simulation Methods for Polymers*, Theodorou, D. N.; Kotelyanski, M. ed.; Marcel Dekker: New York, 2004.
- (4) Baschnagel, J.; Binder, K.; Doruker, P.; Gusev, A. A.; Hahn, O.; Kremer, K.; Mattice, W. L.; Müller-Plathe, F.; Murat, M.; Paul, W.; Santos, S.; Suter, U. W.; Tries, V. *Adv. Polym. Sci.* **2000**, *152*, 41.
- (5) Binder, K. *Monte Carlo and Molecular Dynamics Simulations in Polymer Science*; Oxford University Press: New York, 1995.
- (6) Kremer, K.; Grest, G. S. *J. Chem. Phys.* **1990**, *92*, 5057.
- (7) Auhl, R.; Everaers, R.; Grest, G. S.; Kremer, K.; Plimpton, S. J. *J. Chem. Phys.* **2003**, *119*, 12718.
- (8) Grest, G. S.; Kremer, K. *Phys. Rev. A* **1986**, *33*, 3628.
- (9) Praprotnik, M.; Delle Site, L.; Kremer, K. *Annu. Rev. Phys. Chem.* **2008**, *59*, 545.
- (10) Izvekov, S.; Parrinello, M.; Burnham, C. J.; Voth, G. A. *J. Chem. Phys.* **2004**, *120*, 10896.
- (11) Luybartsev, A. P.; Laaksonen, A. *Phys. Rev. E* **1995**, *52*, 3730.
- (12) Spyriouni, T.; Tzoumanekas, C.; Theodorou, D.; Müller-Plathe, F.; Milano, G. *Macromolecules* **2007**, *40*, 3876.
- (13) Nielsen, S. O. S., G.; Klein, M. *J. Chem. Phys.* **2005**, *123*, 124907.
- (14) Marrink, S. J.; de Vries, A. H.; Mark, A. E. *J. Phys. Chem. B* **2004**, *108*, 750.
- (15) Padding, J. T.; Briels, W. J. *J. Chem. Phys.* **2002**, *117*, 925.
- (16) Li, X. J.; Kou, D. Z.; Rao, S. L.; Liang, H. *J. Chem. Phys.* **2006**, *124*, 204909.
- (17) Haliloglu, T. M., W. L. *J. Chem. Phys.* **1998**, *108*, 6989.
- (18) Sun, Q.; Faller, R. *Macromolecules* **2006**, *39*, 812.
- (19) Carbone, P.; Karimi-Varzaneh, H. A.; Chen, X.; Müller-Plathe, F. *J. Chem. Phys.* **2008**, *128*, 064904.
- (20) Milano, G.; Müller-Plathe, F. *J. Phys. Chem. B* **2005**, *109*, 18609.
- (21) Harmandaris, V. A.; Adhikari, N. P.; van der Vegt, N. F. A.; Kremer, K. *Macromolecules* **2006**, *39*, 6708.
- (22) Larson, R. G. *Mol. Phys.* **2004**, *102*, 341.
- (23) Fukunaga, H.; Takimoto, J.; Doi, M. *J. Chem. Phys.* **2002**, *116*, 8183.
- (24) Reith, D.; Meyer, H.; Müller-Plathe, F. *Macromolecules* **2001**, *34*, 2335.
- (25) Reith, D.; Pütz, M.; Müller-Plathe, F. *J. Comput. Chem.* **2003**, *24*, 1624.
- (26) Tschöp, K. K. W.; Batoulis, J.; Bürger, T.; Hahn, O. *Acta Polym.* **1998**, *49*, 61.
- (27) Paul, W.; Binder, K.; Kremer, K.; Heermann, D. *Macromolecules* **1991**, *24*, 6332.
- (28) Abrams, C.; Kremer, K. *Macromolecules* **2003**, *36*, 260.
- (29) Milano, G.; Goudeau, S.; Müller-Plathe, F. *J. Polym. Sci. Pol. Phys.* **2005**, *43*, 871.
- (30) Meyer, H.; Biermann, O.; Faller, R.; Reith, D.; Müller-Plathe, F. *J. Chem. Phys.* **2000**, *113*, 6264.
- (31) Press, W. H.; Teukolsky, S. A.; Vetterling, W. T.; Flannery, B. P. *Numerical recipes in C. The art of scientific computing.*; Cambridge University Press, 1992.

- (32) Nielsen, S. O.; Lopez, C. F.; Srinivas, G.; Klein, M. L. *J. Chem. Phys.* **2003**, *119*, 7043.
- (33) Queyroy, S.; Neyertz, S.; Brown, D.; Müller-Plathe, F. *Macromolecules* **2004**, *37*, 7338.
- (34) Meyer, H.; Müller-Plathe, F. *Macromolecules* **2002**, *35*, 1241.
- (35) Harmandaris, V. A.; Reith, D.; van der Vegt, N. F. A.; Kremer, K. *Macromol. Chem. Phys.* **2007**, *208*, 2109.
- (36) Peter, C.; Delle Site, L.; Kremer, K. *Soft Matter* **2008**, *4*, 859.
- (37) Reith, D.; Meyer, H.; Müller-Plathe, F. *Comput. Phys. Commun.* **2002**, *148*, 299.
- (38) Henderson, R. L. *Phys. Lett. A* **1974**, *49*, 197.
- (39) Qian, H.-J.; Carbone, P.; Chen, X.; Karimi-Varzaneh, H. A.; Liew, C. C.; Müller-Plathe, F. *Macromolecules* **2008**, *41*, 9919.
- (40) Harmandaris, V. A.; Kremer, K. *Macromolecules* **2009**, *42*, 791.
- (41) Carbone, P.; Negri, F.; Müller-Plathe, F. *Macromolecules* **2007**, *40*, 7074.
- (42) Sun, Q.; Faller, R. *J. Chem. Theory Comput.* **2006**, *2*, 607.
- (43) Karimi-Varzaneh, H. A.; Carbone, P.; Bhargava, B. L.; Balasubramanian, S.; Müller-Plathe, F. *unpublished*.
- (44) Chen, X.; Carbone, P.; Cavalcanti, W. L.; Milano, G.; Müller-Plathe, F. *Macromolecules* **2007**, *40*, 8087.
- (45) Izvekov, S.; Voth, G. A. *J. Chem. Phys.* **2006**, *125*, 151101.
- (46) Leon, S.; van der Vegt, N. F. A.; Delle Site, L.; Kremer, K. *Macromolecules* **2005**, *38*, 8078.
- (47) Izvekov, S.; Voth, G. A. *J. Chem. Phys. B* **2005**, *109*, 2469.
- (48) Izvekov, S.; Voth, G. A. *J. Chem. Phys.* **2005**, *123*, 134105.
- (49) Noid, W. G.; Chu, J.-W.; Ayton, G.S.; Krishna, V.; Izvekov, S.; Voth, G. A.; Das, A.; Anderson, H.C. *J. Chem. Phys.* **2008**, *128*, 244114.
- (50) Noid, W. G.; Chu, J. W.; Ayton, G. S.; Voth, G. A. *J. Phys. Chem. B* **2007**, *111*, 4116.
- (51) Noid, W. G.; Liu, P.; Wang, Y.; Chu, J.-W.; Ayton, G.S.; Krishna, V.; Izvekov, S.; Anderson, H.C.; Voth, G. A. *J. Chem. Phys.* **2008**, *128*, 244115.
- (52) Liu, P.; Voth, G. A. *J. Chem. Phys.* **2007**, *126*, 045106.
- (53) Zhou, J.; Thorpe, I. F.; Izvekov, S.; Voth, G. A. *Biophys. J.* **2007**, *92*, 4289.
- (54) Izvekov, S.; Voth, G. A. *J. Chem. Theory Comput.* **2006**, *2*, 637.
- (55) Wang, Y.; Izvekov, S.; Yan, T.; Voth, G. A. *J. Phys. Chem. B* **2006**, *110*, 3564.
- (56) Wang, Y.; Voth, G. A. *J. Am. Chem. Soc.* **2005**, *127*, 12192.
- (57) Izvekov, S.; Violi, A.; Voth, G. A. *J. Phys. Chem. B* **2005**, *109*, 17019.
- (58) Shi, Q.; Izvekov, S.; Voth, G. A. *J. Phys. Chem. B* **2006**, *110*, 15045.
- (59) Marrink, S. J.; Risselada, H. J.; Yefimov, S.; Tieleman, D. P.; de Vries, A. H. *J. Phys. Chem. B* **2007**, *111*, 7812.
- (60) Baron, R.; Trzesniak, D.; de Vries, A. H.; Elsener, A.; Marrink, S. J.; van Gunsteren, W. F. *Chem. Phys. Chem.* **2007**, *8*, 452.
- (61) Monticelli, L.; Kandasamy, S.; Periole, X.; Larson, R. G.; Tieleman, D. P.; Marrink, S. J. *J. Chem. Theory Comp. In press* **2008**.
- (62) Marrink, S. J.; Mark, A. E. *Biophys. J.* **2004**, *87*, 3894.
- (63) Schneider, J.; Hess, W.; Klein, R. *J. Phys. A* **1985**, *18*, 1221.
- (64) Jiang, W.; Wang, Y. T.; Yan, T. Y.; Voth, G. A. *J. Phys. Chem. C* **2008**, *112*, 1132.
- (65) Qian, H.-J.; Liew, C. C.; Müller-Plathe, F. *Phys. Chem. Chem. Phys.* **2009**, *11*, 1962.
- (66) Groot, R. D.; Warren, P. B. *J. Chem. Phys.* **1997**, *107*, 4423.
- (67) Lowe, C. P. *Europhys. Lett.* **1999**, *47*, 145.
- (68) Abrams, C. F.; Delle Site, L.; Kremer, K. *Phys. Rev. E* **2003**, *67*, 021807.
- (69) Delle Site, L.; Leon, S.; Kremer, K. *J. Am. Chem. Soc.* **2004**, *126*, 2944.
- (70) Praprotnik, M.; Delle Site, L.; Kremer, K. *J. Chem. Phys.* **2005**, *123*, 224106.

-
- (71) Praprotnik, M.; Matysiak, S.; Delle Site, L.; Kremer, K.; Clementi, C. *J. Phys. Condens. Mater* **2007**, *19*, 292201.
- (72) Praprotnik, M.; Delle Site, L.; Kremer, K. *J. Chem. Phys.* **2007**, *126*, 134902.
- (73) Karimi-Varzaneh, H. A.; Carbone, P.; Müller-Plathe, F. *J. Chem. Phys.* **2008**, *129*, 154904.
- (74) Santangelo, G.; Di Matteo, A.; Müller-Plathe, F.; Milano, G. *J. Phys. Chem. B* **2007**, *111*, 2765.
- (75) Meyer, H.; Müller-Plathe, F. *J. Chem. Phys.* **2001**, *115*, 7807.
- (76) Steiner, T. *Angew. Chem., Int. Ed.* **2002**, *41*, 48.
- (77) Sancho, D. D.; Rey, A. *J. Comput. Chem.* **2007**, *28*, 1187.
- (78) Murthy, N. S. *J. Polym. Sci., Part B: Polym. Phys.* **2006**, *44*, 1763.
- (79) Garcia, D.; Starkweather, H. W. *J. Polym. Sci., Polym. Phys. Ed.* **1985**, *23*, 537.
- (80) Bessler, E.; Bier, G. *Makromol. Chem.* **1969**, *122*, 30.
- (81) Trifan, D. S.; Terenzi, J. F. *J. Polym. Sci.* **1958**, *28*, 443.
- (82) Schroeder, L. R.; Cooper, S. L. *J. Appl. Phys.* **1976**, *47*, 4310.

2. IBIsCO: A Molecular Dynamics Simulation Package for Coarse-Grained Simulation

2.1. Introduction

The computer simulation technique has been proven to be a very powerful tool in the research field of polymer and biomolecular systems.^{1,2} However, due to the long chain characteristics and complicate molecular structures of polymers or biomolecules, many properties or phenomena occur over the length and time scales which are not accessible to straightforward atomistic-level simulations. One way to circumvent this problem is to reduce the number of degrees of freedom by using either a general coarse-grained (CG) model, or to develop system-specific CG models. One of the popular methods to develop system-specific CG model is the *Iterative Boltzmann Inversion* (IBI) approach³, which starts with the potential of mean force as guess potential, and then optimizing the potentials iteratively until the reference structure distribution, either from atomistic simulation or experiment, is retrieved. The final optimized potential can be in a tabulated form (non-bonded or bonded interactions) or Gaussian function (bonded interactions). The details of IBI method are referred to Ref. 3.

Recently, different coarse-grained models have been developed successfully in our group for molecular liquid⁴, ionic liquid⁵, polymer melts^{4,6,7}, dendrimer⁸, and polymer solution⁴ using IBI³ approach. Extensive coarse-graining simulations also have been performed on these models under both equilibrium^{7,9} and non-equilibrium¹⁰ conditions. One of the main challenges of such CG models is the artificially too fast dynamics which mainly arises from the effect of reduced degrees of freedom in the system. To overcome this problem and to have the correct dynamics in the CG simulation different approaches have been proposed.^{11,12} The techniques of pair-wise Langevin-type dissipative particle dynamics¹³ (DPD), and Lowe-Andersen¹⁴ (LA) equations of motion can be used to enhance the frictions between particles, hence, to slow down the particle mobility. Both of them have been used successfully for the simulation of coarse-grained ethyl-benzene liquid, polystyrene oligomer melt¹², and ionic liquid⁵ in our group.

Based on the CG simulations which have been performed in our group, and in order to validate the workflow of developing CG models using IBI method, we feel the need to provide a detailed description of the IBIsCO code, which is a parallelized program package using MPI, specially developed for the CG simulations using Gaussian functions or tabulated interaction potentials derived

from IBI approach. Various ensembles (NVT, NPT, and NVE) are valid in IBIsCO. The techniques of dissipative particle dynamics¹³ (DPD) and Lowe-Andersen¹⁴ (LA) equations of motion are also embedded in IBIsCO. Both of the DPD and LA can introduce frictions into system to compensate the effects of lost degrees of freedom in CG models, hence, slow down the too fast dynamics in CG simulation induced by softness and less friction in the CG representation¹². In addition, they can also be used as thermostats to perform the simulation in canonical ensemble. Moreover, a novel approach, so-called Reverse Non-equilibrium Molecular Dynamics²¹ (RNEMD) simulation technique is also implemented in IBIsCO, with the combination of DPD and LA equations of motion; one can calculate the viscosity or study the structure alternations under non-equilibrium condition.

This article describes the basic MD algorithms, the capabilities and usage of IBIsCO.

2.2. Molecular Dynamics Algorithms and Functionalities of IBIsCO

2.2.1. Force Field

Similar to the atomistic force fields, the system energy in the coarse-grained model is divided into various partial energy contributions, as expressed:

$$V = V_{bond} + V_{angle} + V_{torsions} + V_{nonbonded} \quad (2-1)$$

where V_{bond} , V_{angle} and $V_{torsion}$ correspond to the bonded part (bond, angle and torsion interactions) of the potential, and $V_{nonbonded}$ represents the non-bonded potential.

Bonded Potential. In IBIsCO, there are two options to define the bonded interactions. One possibility is to prepare a file called *Gaussian*, which specifies the Gaussian functions parameters that fit to the bond lengths and angle distributions¹⁵ (format of the *Gaussian* file is given in the section **2.4.2 Input Files**); the second option is to prepare tabulated potentials for bond and angle interactions following the IBI procedure. The strategy to calculate the potential and force during the simulation is the same for both options. Potential tables/Gaussian parameters in *Gaussian* file are saved/transformed to intrinsic arrays (potential tables) in the code. Tables for the forces are constructed at the same time. During the simulation, the interaction potentials or forces are calculated from such intrinsic potential/force tables with linear interpolation according to the separation between atom pair.

In the *Gaussian* file, a multi peaked distribution of a structural parameter θ (bond or angle) is approximated by a sum of n Gaussian functions characterized by the center position (θ_{ci}), the total area (A_i), and the width (w_i):

$$P(\theta) = \sum_{i=1}^n \frac{A_i}{w_i \sqrt{\pi/2}} \exp\left(-2 \frac{(\theta - \theta_{ci})^2}{w_i^2}\right) \quad (2-2)$$

Given a distribution $P(\theta)$ of a structural parameter θ , the corresponding potential is derived by a simple Boltzmann inversion of $P(\theta)$. The corresponding potential, $V(\theta)$ obtained by Boltzmann inversion is written as follows:

$$V(\theta) = -k_B T \ln \sum_{i=1}^n \frac{A_i}{w_i \sqrt{\pi/2}} \exp\left(-2 \frac{(\theta - \theta_{ci})^2}{w_i^2}\right) \quad (2-3)$$

where k_B is the Boltzmann constant and T is the temperature.

If we define $g_i(\theta) = \frac{A_i}{w_i \sqrt{\pi/2}} \exp\left(-2 \frac{(\theta - \theta_{ci})^2}{w_i^2}\right)$, the potential can be written in a more compact form:

$$V(\theta) = -k_B T \ln \sum_{i=1}^n g_i(\theta) \quad (2-4)$$

For the bond potentials, it is possible to derive similar equation:

$$V(l) = -k_B T \ln \sum_{i=1}^n g_i(l) \quad (2-5)$$

where l is the bond length.

Non-bonded Potential. In IBIsCO, there is no any specific analytical function to calculate the non-bonded interactions. All the non-bonded interactions are treated as tabulated potentials as a function of distance (r), and they have to be prepared as input files for different type of non-bonded interactions in the system.

Forces. The bonded and non-bonded forces are calculated by the numerical derivate of the potentials:

$$F(x_i) = -\left(\frac{V(x_{i+1}) - V(x_{i-1})}{x_{i+1} - x_{i-1}}\right)\Big|_{x=l,\theta,r} \quad (2-6)$$

where x corresponds to l , θ and r for bond, bend and non-bonded potentials, respectively. i is the position index of tabulated point. For the treatment of intra-molecular non-bonded interactions, IBIsCO has two options, excluding either 1-4 or 1-5 interactions which are separated by 3 or 4 successive bonds. This is defined by the keyword of **Non-Bonded** in *control* file (see section **Input Files**).

2.2.2. Construction of Non-Bonded Interaction Neighbor List

Both of the Verlet neighbour list and link-cell list techniques¹⁶ have been used in IBIsCO to minimize the CPU time expended on the calculation of non-bonded potentials and forces. The standard Verlet neighbour list technique is used to construct neighbour list for small boxes. When the simulation volume domain size of each processor in every direction is bigger than three times of the neighbour list cutoff radius R_L (defined by the keyword of `Neighbor_list_cutoff` in *control* file), the link-cell neighbour list technique will be used to construct the neighbour list. The simulation area in every processor is split into small cells with lattice size of R_L , then the searching of the particle neighbours are restricted to those particles in the same cell and those in the half (13 in 3D) of the nearest neighbouring link cells. Details of this technique are referred to Ref. ¹⁶. The neighbour list array is updated every a few time steps in the simulation, which is defined by the keyword of `Update_neighbour_list` in *control* file. Reassignment of the particles to the processors is also done with the same frequency.

The general flowchart of IBIsCO is shown in Figure 2.1.

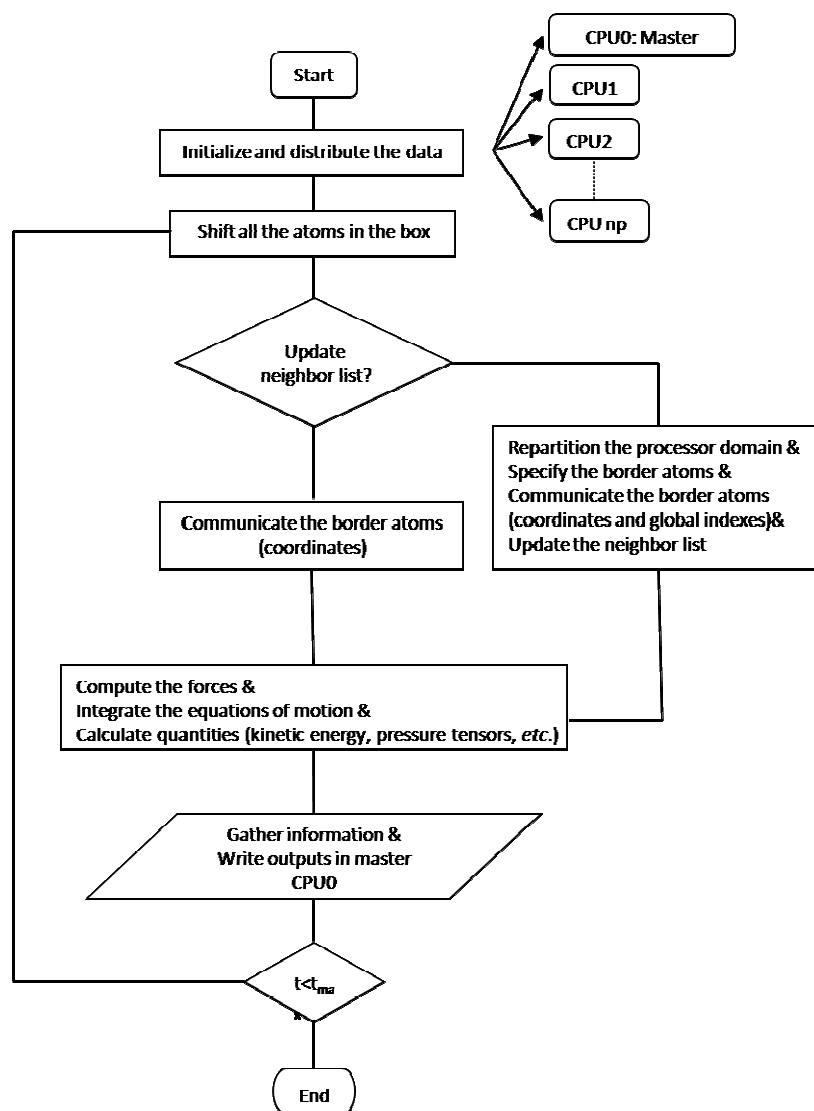


Figure 2.1. The flowchart of the IBIsCO program.

2.2.3. Integration Schemes for the Equations of Motion

IBIsCO offers three different algorithms for the integration of the equations of motion. The basic leapfrog algorithm is used for the conventional MD simulation. On the other hand, since IBIsCO is developed for the coarse-graining simulation, dissipative particle dynamics¹³ (DPD) and its alternative, the Lowe-Andersen¹⁴ (LA) equations of motion which are suitable on the CG level are also embedded in IBIsCO.

2.2.3.1. Leapfrog Scheme

In leapfrog scheme¹⁶, the particle velocity \mathbf{v} and position \mathbf{r} are updated as following,

$$\mathbf{v}_i(t + \frac{\Delta t}{2}) = \mathbf{v}_i(t - \frac{\Delta t}{2}) + \Delta t \frac{\mathbf{f}_i(t)}{m_i} \quad (2-7)$$

$$\mathbf{r}_i(t + \Delta t) = \mathbf{r}_i(t) + \Delta t \mathbf{v}_i(t + \frac{\Delta t}{2}) \quad (2-8)$$

where Δt is the time step, m_i is mass of atom i , and \mathbf{f}_i corresponds to the force exerting on the atom i . Velocities are evaluated at half steps, and positions and forces are calculated at full steps. Velocity at the current time step $\mathbf{v}_i(t)$ is calculated from:

$$\mathbf{v}_i(t) = (\mathbf{v}_i(t - \frac{\Delta t}{2}) + \mathbf{v}_i(t + \frac{\Delta t}{2}))/2 \quad (2-9)$$

2.2.3.2. Dissipative Particle Dynamics

In DPD simulation, besides the conventional conservative interactions between particles (described by eq 2.1), a pair-wise dissipative force (eq 2.10) and a random force (eq 2.11) are also acting on interacting pairs:

$$\mathbf{F}_{ij}^D = -\gamma w^D(r_{ij})(\mathbf{v}_{ij} \cdot \mathbf{e}_{ij})\mathbf{e}_{ij} \quad (2-10)$$

$$\mathbf{F}_{ij}^R = \sigma w^R(r_{ij})\theta_{ij}\Delta t^{-1/2}\mathbf{e}_{ij} \quad (2-11)$$

where $\mathbf{e}_{ij} = \mathbf{r}_{ij}/r_{ij}$ is the unit vector along the connecting line between the particles i and j , $\mathbf{v}_{ij} = \mathbf{v}_i - \mathbf{v}_j$ is their relative velocity, γ (kg s⁻¹) and σ (N s^{1/2}) are strengths of dissipative force and random forces, respectively, and $w^D(r)$ and $w^R(r)$ are weighting functions for these forces; θ_{ij} is a uniformly distributed random variable with zero mean and unit variance, which is independent on different pairs of particles and different time steps.¹³ The dissipative force is proportional to the relative velocity of the interacting particle pair, which mimics the friction between particles and accounts for energy dissipation, while the random force compensates for the degrees of freedom removed by coarse-graining, and acts as a heat source. According to the fluctuation dissipation theorem, the dissipative and random forces are coupled together by the relations $w^D(r) = [w^R(r)]^2 = w(r)$ and $\sigma^2 = 2\gamma k_B T$, and they form a thermostat of temperature T .¹³ Since noise and friction are coupled, only one of the parameters can be adjusted independently. In IBIsCO, the noise strength σ is set as an input parameter. Dissipative and random forces act only between particles within a cutoff radius of r_c . Their pairwise nature together with the short cutoff ensure the local momentum conservation, leading to correct long-

range hydrodynamics.¹⁷ Note here, there are two options for the weighting function $w(r)$ in IBIsCO, one is a linear and the other one is a step function as following:

$$w(r) = (1 - r/r_c)^2 \quad (2-12)$$

$$w(r) = 1 \quad (2-13)$$

To solve the stochastic equations of motion, IBIsCO is using a modified velocity-Verlet algorithm¹³:

$$\begin{aligned} \mathbf{r}_i(t + \Delta t) &= \mathbf{r}_i(t) + \Delta t \mathbf{v}_i(t) + 1/2(\Delta t)^2 \mathbf{f}_i(t) / m_i \\ \tilde{\mathbf{v}}_i(t + \Delta t) &= \mathbf{v}_i(t) + \lambda \Delta t \mathbf{f}_i(t) / m_i \\ \mathbf{f}_i(t + \Delta t) &= \mathbf{f}_i(\mathbf{r}(t + \Delta t), \tilde{\mathbf{v}}(t + \Delta t)) \\ \mathbf{v}_i(t + \Delta t) &= \mathbf{v}_i(t) + 1/2\Delta t(\mathbf{f}_i(t) + \mathbf{f}_i(t + \Delta t)) / m_i \end{aligned} \quad (2-14)$$

where an intermediate velocity $\tilde{\mathbf{v}}$ is predicted for the calculation of dissipative forces (eq 2.10). The particle velocities are updated in the last step. \mathbf{f}_i is the total force on particle i including the non-bonded and bonded forces (eq 2.1), the dissipative (eq 2.10) and the random (eq 2.11) forces. The empirical integration constant λ is chosen to be 0.65 according to Ref. ¹³.

2.2.3.3. Lowe-Andersen Scheme

The Lowe-Andersen technique¹⁴ is an alternative to DPD based on the idea of Andersen's thermostat. It also conserves local linear momentum. Instead of using explicit friction and noise as in DPD, the relative energy of particle pairs within a certain cutoff is dissipated by periodically resampling from a Maxwell-Boltzmann distribution with a chosen "bath collision" frequency. This is done by adding random velocities along the connecting line between the particles:

$$\begin{aligned} \mathbf{v}_i &= \mathbf{v}_i + M_{ij} [\xi_{ij} \sqrt{k_B T_0 / M_{ij}} - \mathbf{v}_{ij} \cdot \mathbf{e}_{ij}] \mathbf{e}_{ij} / m_i \\ \mathbf{v}_j &= \mathbf{v}_j - M_{ij} [\xi_{ij} \sqrt{k_B T_0 / M_{ij}} - \mathbf{v}_{ij} \cdot \mathbf{e}_{ij}] \mathbf{e}_{ij} / m_j \end{aligned} \quad (2-15)$$

where $M_{ij} = m_i m_j / (m_i + m_j)$ is the reduced mass of the particle pair; m_i and m_j are the mass of particles i and j , respectively; \mathbf{e}_{ij} is the unit vector along the connecting line; ξ_{ij} is a Gaussian random variable of zero mean and unit variance generated by an algorithm from Ref. ¹⁸; T_0 is the system temperature, and k_B is the Boltzmann constant. By construction, the total momentum of the particle pair is conserved, therefore LA is also locally momentum-conserving and Galilean-invariant.

In LA scheme, the interaction with the heat bath is described by a Langevin equation for relative velocities rather explicit random and friction forces. Since there is no velocity-dependent dissipative force, the equations of motion can be solved by a standard velocity-Verlet algorithm, as used in literature,^{14,19} or the leap-frog scheme which is used in IBIsCO. At every time step, for each

pair of close particles, a new relative velocity is generated from a Maxwell distribution $\xi_{ij}\sqrt{k_B T_0 / M_{ij}}$ with a probability of $\Gamma / \Delta t$ (1/ps). The new relative velocity acts along the connecting line between centers of the particles (eq 2.15). The scheme in detail is as following:

- (i) $\mathbf{f}_i(t) = \mathbf{f}_i(\mathbf{r}(t))$
- (ii) For each pair of particles for which $r_{ij}(t) < r_c$
 - (a). Generate $\xi_{ij}\sqrt{k_B T_0 / M_{ij}}$ from a Maxwell distribution with a probability of $\Gamma / \Delta t$
 - (b). $\mathbf{v}_i = \mathbf{v}_i + M_{ij}[\xi_{ij}\sqrt{k_B T_0 / M_{ij}} - \mathbf{v}_{ij} \cdot \mathbf{e}_{ij}]\mathbf{e}_{ij} / m_i$
 - (c). $\mathbf{v}_j = \mathbf{v}_j - M_{ij}[\xi_{ij}\sqrt{k_B T_0 / M_{ij}} - \mathbf{v}_{ij} \cdot \mathbf{e}_{ij}]\mathbf{e}_{ij} / m_j$
- (iii) $\mathbf{v}_i(t + \frac{\Delta t}{2}) = \mathbf{v}_i(t - \frac{\Delta t}{2}) + \Delta t \frac{\mathbf{f}_i(t)}{m_i}$
- (iv) $\mathbf{r}_i(t + \Delta t) = \mathbf{r}_i(t) + \Delta t \mathbf{v}_i(t + \frac{\Delta t}{2})$ (2-16)

The probability $\Gamma / \Delta t$ corresponds to a collision frequency which is controlled by a uniform random number u between zero and one. This random number is independent for different particle pairs and different times. For every close pair of particles ($r_{ij}(t) < r_c$), a random number u , smaller than preset value of Γ will designate a new relative velocity to the particles from a Maxwell distribution.

2.2.4. Berendsen's Thermostat and Barostat

Berendsen's algorithm²⁰ is used in IBIsCO to perform constant-temperature and constant-pressure MD simulations. The temperature scaling factor δ (eq 2.17) is used for a uniform scaling of the atom velocities, and the pressure scaling factor μ (eq 2.18) for a uniform scaling of the atom positions and box lengths:

$$\delta = \left[1 + \frac{\Delta t}{\tau_T} \left\{ \frac{T_0}{T(t - \Delta t)} - 1 \right\} \right]^{1/2} \quad (2-17)$$

$$\mu = \left\{ 1 + \frac{\Delta t}{\tau_P} \beta [P(t) - P_0] \right\}^{1/3} \quad (2-18)$$

where $T(t - \Delta t)$ and $P(t)$ are the instantaneous temperature and pressure of the system, T_0 and P_0 are the corresponding values for the bath, τ_T and τ_P are the coupling time which determines the frequency of

the system reacts to a deviation of T or P from target bath values, and β is the isothermal compressibility.

2.2.5. Reverse Non-Equilibrium Molecular Dynamics (RNEMD)

For details of the RNEMD method we refer the reader to Ref ²¹. Here we just give a brief description of the essential steps. The RNEMD is currently implemented in IBIsCO only for the viscosity calculation, since it has been proven very efficient on that ^{10,22}. One can also use it to calculate more properties, such as Soret effect ²³ and thermal conductivity. ²⁴ The viscosity is calculated as the ratio of a transverse momentum flux and a shear field:

$$j_z(p_x) = -\eta \frac{\partial \bar{v}_x(z)}{\partial z} \quad (2-19)$$

where $j_z(p_x)$ is the transverse momentum flux transported in the z direction, the shear field is defined as the velocity gradient along the z direction, $\frac{\partial \bar{v}_x(z)}{\partial z}$, and η is the shear viscosity. Note that the momentum flux can also be calculated by the off-diagonal component of the stress tensor σ_{xz} .

In RNEMD method, the typical cause-and-effect picture in conventional non-equilibrium MD simulation is reversed: the effect, the momentum flux is imposed by swapping the particle velocities as the cause; the cause, the velocity gradient or the shear rate is obtained during simulation as the effect. Two symmetric Couette flows are obtained with shear flow in x direction and velocity gradient in z direction. The whole procedure of this method is described as following:

- (1) The simulation box along the z direction is divided into N (even) slabs, and labeled from $n = 1$ to $n = N$ in a bottom-to-up sequence. The flow on the box boundary (in slab 1 and slab N) is supposed to be in the $+x$ direction, whereas the flow in the middle of the box (slab $n = M = N/2 + 1$) is in the $-x$ direction.
- (2) To achieve the above condition, the atom in the 1st slab with the largest velocity component in the $-x$ direction and the atom in the M slab with the largest velocity component in the $+x$ direction are identified. The two atoms must have the same mass.
- (3) Finally the v_x components of the two atoms are exchanged. Since the two involved atoms have the same mass, this unphysical momentum swap procedure conserves both linear momentum and kinetic energy of the system as a whole. At the same time, the potential energy, hence, the total energy of the system is also conserved, because the positions of the atoms are not changed.

The above procedure is repeated during the simulation periodically with a preset frequency (every W time steps). A schematic picture of this method is shown in Figure 2.2. The total momentum P_x transferred from the $n = M$ slab to the bottom slab $n = 1$ is the summation of the amount transferred in each velocity swap Δp_x which is precisely known. Hence, the momentum flux can be calculated by

$$j(p_x) = \frac{P_x}{2tA} = \frac{\sum \Delta p_x}{2tA} \quad (2-20)$$

where t is the simulation time, $A = L_x L_y$ is the area of xy plane, the factor 2 arises from the periodicity in z direction.

In the steady state, the rate of momentum transferred unphysically by momentum swaps is equal to that of momentum flowing back through the fluid by friction as depicted in Figure 2.2. The induced momentum current gives rise to a velocity profile in the box (see Figure 2.2). The flow velocity component in each slab, $\langle v_{x,i} \rangle$, is determined by averaging over all the particles in the slab. If the momentum flux is not too large, a linear velocity profile would be obtained and velocity gradient $\langle \partial v_x(z) / \partial z \rangle$ can be calculated by a linear regression. In IBIsCO, the exchanged momentum is accumulated during the simulation, and the momentum flux is calculated from the average of cumulative value. The velocity profile in each slab is also calculated from the time average of cumulative information, $\langle v_x(z) \rangle$, where $\langle \rangle$ denotes the time average. Afterward, the velocity gradient is obtained from this averaged $\langle v_x(z) \rangle$ profile with linear regression. The viscosity is then given by eq 2.19. Its error can be estimated from the errors in the velocity gradient and the momentum flux using the rules for error propagation.

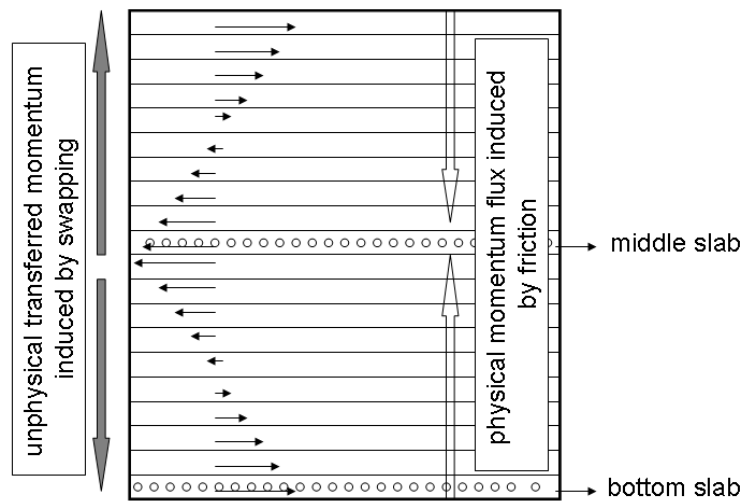


Figure 2.2. A schematic view of the periodic simulation box in the RNEMD simulation.

2.3. Parallelization Strategy

IBIsCO is parallelized in the base of a 3-dimensional (3D) form of volume domain decomposition method.²⁵⁻²⁸ The method has been used extensively for different MD simulation codes.²⁹⁻³² Readers are referred to Ref³³ for the details. In this part we just present the essentials which have been used in IBIsCO. The inter-CPU communication is implemented using MPI.

A schematic flow chat is shown in Figure 2.1. After the simulation starts, every processor is reading the input files, the particles within the primary MD simulation box are mapped onto the processors according to their coordinates (x, y, z). Every particle has a global index as specified in the initial *coordinate* file, and it receives a local index in each processor in the residing order in the processor. The number of processors in every direction is specified in the *control* file by keywords of NPX, NPY and NPZ, they determine the simulation domain volume size that each processor is responsible for. The total number of processor one needs is ($NP = NPX \times NPY \times NPZ + 1$). One extra processor is responsible for collecting the total information of the whole simulation box and writing the outputs. In this initialize step, all the processors record the connectivity information between atoms according to their global index. Lists of all the possible bonds, angles, and torsions (if they are included in the *interaction* file) are created at this step for all the processors. During the simulation, when a particle is crossing the border between two processors, the original processor only needs to send the global index of the particle to the neighbor processor which the particle is moving to, and then the new processor will know all the information related to the connectivity of this new coming particle. The second step is to shift all the atoms into the simulation box, to repartition the simulation volume domain, to communicate the border region between neighboring processors, and update the interaction neighbor list according to the updating frequency specified in *control* file for each processor. After this step, each processor computes the interaction potentials and forces, integrates the equations of motion, updates particles coordinates and velocities, and calculates the quantities like temperature and pressure tensors. Finally, all the information from all simulation processors are gathered in *Master* processor and this *Master* processor will write the simulation outputs.

Figure 2.3 shows a schematic communication scheme which is used in IBIsCO. The interactions in the border region between two processors are calculated in one of them. For instance, in Figure 2.3, the interaction between particle i and j in the border region between processor P5 and P7, and the interaction between particle i and k in the border region between processor P5 and P8, are both

calculated in processor P5. The information of particle j and k (global indexes and coordinates of the particles) are sent from processor P7 to P5, and from P8 to P5 respectively. Afterward, the interactions between $i-j$ and $i-k$ pairs are calculated in processor P5. Finally, the interaction potentials and forces between pairs $i-j$ and $i-k$ are send back to P7 and P8 respectively by P5. Based on this idea, each processor receives half of the total border region from its neighbouring processors. For instance, for the processor P5 in Figure 2.3, it only receives border region from processors P6, P7, P8, and P9 (the shadowed region). Then the interactions between all the residing atoms in this processor and the interactions exerting from border atoms in shadowed region on residing atoms are calculated in this processor. Afterwards, the interactions on border atoms from reside atoms are send back to corresponding processors where the border atoms come from (reside).

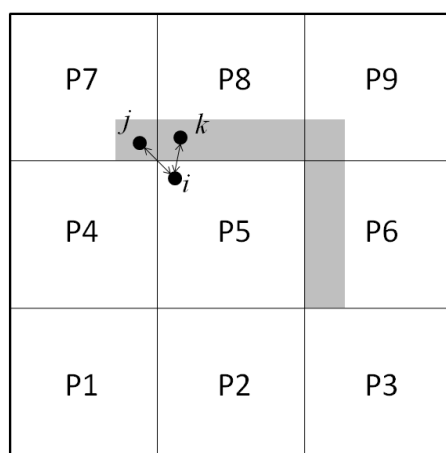


Figure 2.3. A schematic illustration of the volume domain decomposition scheme and the communication scheme between neighboring processors on one a dimensional system.

2.4. Interfaces and File Formats

2.4.1. Units

The units of the different parameters in IBIsCO are summarized in Table 2.1. During the simulation steps, the program is using a set of reduced units. The basic choice for the reduced units (indicated by an asterisk) is the following: (i) unit of length is taken as one nanometre (Rscale), (ii) $k_B \times 300$ ($\text{m}^2\text{kg/s}^2$) as unit of energy (Escale), where k_B is Boltzmann constant and (iii) atomic mass of carbon as the unit of mass (Mscale), and from these basic units all other units follow (time (t), pressure (P) and temperature (T)).

$$t^* = \frac{k_B}{Escale} t$$

$$P^* = \frac{1000 \times Rscale^3}{Escale} P \quad (2-21)$$

$$T^* = \frac{1}{Rscale} \sqrt{\frac{Escale}{Mscale}} T$$

Table 2.1. Units of various physical quantities in IBIsCO.

Parameter	Unit
Length	Nanometre (nm)
Volume	Cubic nanometre (nm^3)
Angle	Degree
Time	Pico-second (ps)
Energy	kJ/mol
Mass	g/mol
Velocity	nm/ps
Temperature	Kelvin (K)
Pressure	kPa
Mass density	kg/m^3

2.4.2. Input Files

There are three main input files (*control*, *interaction* and *coordinate*), which program needs for any simulation. The format of these files is given in the following. Lines starting with hash (#) are regarded as comment lines, and they must be kept, and all items are free-format then spacing is not so important.

a) *control* file. This is the file that contains the general parameters for the simulation (ensemble, thermodynamic conditions, number of atoms, timesteps, etc.). An example of a *control* file is shown in Figure 2.4.

Following are the keywords currently supported in IBIsCO:

Ensemble: one of the following character strings: NVE, NVT, NPT, LA, or DPD. This keyword specifies the ensemble of the MD simulation. There are currently five options: NVE (micro canonical), NVT (canonical), NPT (isobaric-isothermal) ensembles, LA (Lowe-Andersen), and DPD (dissipative particle dynamics).

Temperature: initial temperature in Kelvin (1 floating-point number). Note that this temperature is used for thermostat and also for calculating the forces and potentials by Boltzmann inversion.

Pressure: initial pressure in kPa (target pressure in NPT ensemble) (1 floating-point number).

Natoms: total number of atoms in the system (1 integer number).

Nsteps: total number of time steps of the simulation (1 integer number).

DT: time step in fs (1 floating-point number).

TAUT: thermostat coupling time in ps (1 floating-point number).

TAUP: pressure relaxation time in ps (1 floating-point number).

BETA: isothermal compressibility (1/kPa) (1 floating-point number).

Cutoff: the cutoff distance for the non-bonded interactions in nm (1 floating-point number).

Neighbor_list_cutoff: the distance in nm up to which pairs of particles are included in the neighbor list (1 floating-point number).

Update_neighbor_list: number of time steps between updating the neighbor list (1 integer number).

Nsampling: number of time steps between printouts of the instantaneous values (1 integer number).

Ntrajectory: number of time steps between output of the coordinates, velocities, etc. to trajectory file (1 integer number). For contents of the trajectory file, see the next section.

Halt_Drift: number of time steps between resetting the total linear momentum of the system to zero (1 integer number). This control keyword is not needed for DPD and Lowe-Andersen simulation.

Naverage: number of time steps between calculation of running averages and printout of the restart file (1 integer number).

Non-Bonded: (the value is equals to either '4' or '5', 1 integer number). IBIsCO provides two possible treatments of the non-bonded interaction pairs within the same molecule: non-bonded interactions between atoms separated by more than two bonds ('1..4' interactions and beyond) or three bonds ('1..5' interactions and beyond) are treated explicitly. The value of '4' stands that '1..4' interactions and beyond are treated, and the value of '5' stands for treatment of '1..5' interactions and beyond.

Interaction: (it's either 'GAUSSIAN' or 'TABLE', one character string). IBIsCO provides two options to define the bond and bending interactions. One possibility is to prepare a *Gaussian* file and

specify the Gaussian functions that are fitting to the bond length and angles distributions; the other possibility is to prepare the tabulated numerical potentials for bond and bending interactions.

N.B. The potential is made from a distribution by Boltzmann inversion. In the inversion, the temperature (as specified in the *control* file) is used. This means that, with the GAUSSIAN option, simulation at different temperatures have different potential energy functions for the bonded interactions, if the same distribution is used as input. To avoid this, one must use the tabulated potentials.

Reset_velocities: (it's either 'YES' or 'NO', one character string). The value of 'YES' will let IBIsCO to initialize the particle velocities according to a Maxwell-Boltzmann distribution; 'NO' will let IBIsCO to read the velocities from the coordinate file.

Weight_type: (it's either 'Linear' or 'Step', one character string). This keyword specifies the type of weighting functions (linear and step) in DPD simulation as indicated in eq 2.12 and eq 2.13, respectively.

ISEED: seed of random number generator in DPD/LA simulation (1 integer number).

sigma: noise strength (σ in eq 2.11) for the DPD simulation (1 floating-point number).

LAFREQ: collision frequency (Γ in eq 2.16-(ii)-(a)) in Lowe-Andersen simulation (1 floating-point number).

DPD_cutoff: cutoff distance for DPD interactions (eq 2.10 and eq 2.11) in nm. The maximum value is the cutoff distance for the non-bonded interactions.

RNEMD: (it's either 'YES' or 'NO', one character string). This is the keyword for the viscosity calculation by RNEMD method, the value of 'YES' will switch on the viscosity calculation; 'NO' will switch off this functionality.

T_EQ: number of time steps needed before a stable state to be reached in RNEMD simulation (1 integer number). The flow profiles (the velocity and the transferred momentum) in RNEMD simulation will be re-accumulated after T_EQ time steps for the viscosity calculation.

Num_RNEMD_slab: number of slabs in RNEMD simulation (1 integer number).

Num_RNEMD_exchange: number of time steps between swaps of the velocities in RNEMD simulation (1 integer number).

Num_RNEMD_prof: number of time steps between recording the flow profiles (density, temperature, and velocity) in slabs in RNEMD simulation (1 integer number).

Num_RNEMD_trj: number of time steps between calculating and recording the velocity gradient and the viscosity in RNEMD simulation (1 integer number).

NPX: number of processors in *x* direction.

NPY: number of processors in y direction.

NPZ: number of processors in z direction.

In this program, one of the processors is assigned to write the output files. Then total number of processors that one needs to run the program will be $NPX \cdot NPY \cdot NPZ + 1$.

Boundary: This program is using a domain decomposition strategy to distribute the system between the processors. To calculate the non-bonded interaction, each processor needs to receive the boundary region from neighbor processors. In this case the width of boundary region is the cutoff for the non-bonded interactions, but some time after mapping from atomistic to coarse-graining super atoms are so far, and to calculate the bonded part of forces and potentials (angle and torsion) one needs to use a bigger number for boundary width to receive all information from neighbor processors.

END: no data, it terminates reading the *control* file.

Ensemble	NVT	(NVE, NVT, NPT, LA, DPD) ILA:Lowe-Andersen, DPD:standard DPD
Temperature	400	(Temperature (K))
Pressure	101.3	(Pressure (kPa))
Natoms	6000	(Number of atoms)
Nsteps	3000000	(Number of time steps)
DT	5	(Time step in fs)
TAUT	0.1D0	(Temperature relaxation time in ps)
TAUP	1.0D0	(Pressure relaxation time in ps)
BETA	1.0D-6	(Isothermal compressibility (1/kPa))
Cutoff	1.1	(The cutoff distance for non-bonded interaction in nm)
Neighbour_list_cutoff	1.2	(The cutoff distance in nm)
Update_neighbour_list	5	(Number of time steps between neighbour list updates)
Nsampling	2000	(Number of time steps between sampling the system quantities)
Ntrajectory	4000	(Number of time steps between storing configuration in trajectory file)
Halt_Drift	1000	(Interval at which the net drift of the system is reset to zero)
Naverage	4000	(Number of time steps between storing average data and restart file)
Non-Bonded	4	(Use non-bonded potatial on 1..4 OR 1..5 pairs and beyond. 4=1..4, 5=1..5)
Interaction	TABLE	(type of bonded (bond and bending) interactions? GAUSSIAN/TABLE)
Restart_velocities	NO	(Do you want to restart the initial velocities (use Boltzmann distribution)? YES or NO)
Weight_type	STEP	(Linear (1-r/rcut) or step = 1, default is Linear, type of weighting function for DPD)
ISEED	1234	(seed for the random number generator in DPD/LA simulation: an integer number)
sigma	8.0	(noise strength in DPD simulation)
LAFREQ:	0.005	(Gamma, collision frequency in LA simulation)
DPD_cutoff	1.1	(cutoff distance for DPD forces: random force and dissipative force)
RNEMD	YES	(Do you want to perform RNEMD simulation to calculate viscosity? YES/NO)
T_EQ	500000	(time steps need to be excluded before starting the viscosity calculation)
Num_RNEMD_slab	20	(number of slabs in RNEMD simulation)
Num_RNEMD_exchange	400	(time steps between the velocity swaps in RNEMD simulation)
Num_RNEMD_prof	401	(time steps between recording profiles in slabs)
NUM_RNEMD_trj	401	(time steps between recording flux, velocity gradient, and viscosity in md.ntr file)
NPX	2	(Number of processors in X direction)
NPY	2	(Number of processors in Y direction)
NPZ	2	(Number of processors in Z direction)
Boundary	1.3	(Width of the boundary region to communicate , Boundary >=Cutoff)
END		

Figure 2.4. A schematic view of the *control* file.

b) *interaction* file. This file defines the types of beads (atoms), bonds, angles, torsion angles and non-bonded interactions involved in the system. The atoms are defined in the sequence of atom type (an integer number), atom label (a character string), and mass of the atom (a floating-point number) in lines, one line for one atom type. The bonded (bonds, angles, and torsions) and non-bonded

interactions are defined in lines by the involved atom types followed by the file name which contains the tabulated potentials (if tabulated potentials are used), one line for one type of interaction. An example of an *interaction* file is shown in Figure 2.5. Following is the details of the record lines in the *interaction* file:

1. Arbitrary title.
2. The number of different atom types (1 integer number) followed by the keyword of `No._of_different_atom_types` which must not be changed.
3. Comment line.
4. The atom type (1 integer number), followed by atom label (character string) and mass of the atom (in g/mol) (1 floating-point number), one atom type in every line.
5. The number of different types of bonds (1 integer number) followed by the keyword of `No._of_different_types_of_bonds`, this keyword must not be changed.
6. Comment line.
7. The atom types (2 integer numbers) involved in each type of bond, followed by the name of the file which contains the tabulated bond potential in case the tabulated form are used for bond potentials.
8. The number of different types of bond angles (1 integer number) followed by the keyword of `No._of_different_types_of_bond_angles`, the keyword must not be changed.
9. Comment line.
10. The types of three successive connecting atoms (3 integer numbers) involved in each angle type, followed by the name of the file which contains the tabulated angle potential in case the tabulated form are used for angle potentials.
11. The number of different types of torsions (1 integer number) followed by the keyword of `No._of_different_types_of_torsions`, the keyword must not be changed.
12. Comment line.
13. The types of four successive connecting atoms (4 integer numbers) involved in one torsion angle type, followed by the name of the file which contains the tabulated torsion potential.
14. The number of non-bonded interactions (1 integer number) followed by the keyword of `No._of_non-bonded_interactions`, the keyword must not be changed.
15. Comment line.
16. The types of the two atoms (2 integer numbers) involved in the non-bonded interaction followed by the name of tabulated potential file.

```

# ***** CG Of Hexane
2   No._of_different_atom_types
# **** Type      Label      Mass/(g/mole)
1       CH3      15.023475
2       CH2      14.01565
2   No._of_different_types_of_bonds (Distance:nm, Potential:kJ/mol)
# **** Type_1    Type_2      pot_file
1       2        a.pot
2       2        a.pot
2   No._of_different_types_of_bond_angles (Angle:Degree, Potential:kJ/mol)
# **** Type_1    Type_2      Type_3      pot_file
1       2        2        a-b.pot
2       2        2        a-b.pot
2   No._of_different_types_of_torsions (Angle:Degree, Potential:kJ/mol)
# **** Type_1    Type_2      Type_3      Type_4      pot_file
1       2        2        2        a-b-b.pot
2       2        2        2        a-b-b.pot
3   No._of_non-bonded_interactions (Distance:nm, Potential: kJ/mol)
# **** Type_1    Type_2      nb_pot_file
1       1        aa.pot
2       2        bb.pot
1       2        ab.pot

```

Figure 2.5. A schematic view of the *interaction* file.

c) *coordinate* file. This file defines the initial coordinates, the initial velocities of the atoms, and the connectivity between them. Figure 2.6 shows an example of a *coordinate* file. The *coordinate* file contains following records:

1. Comment.
2. Time: previous simulated time (in ps).
3. Comment.
4. Box length for x, y, and z directions in nm.
5. Comment (5 lines).
6. Total number of molecules.
7. Total number of atom in the molecule, a comment (*Atoms_in_Molecule_No.*) and then index of the molecule.
8. For each atom in the molecule, the index of the atom, type of the atom (correspond to the atom type in the *interaction* file), number of atoms connected to this one, coordinate (S_x , S_y , S_z), velocity (V_x , V_y , V_z) and indices of the connected atoms are given (the connectors (bonds) are specified twice: one time for each of the two atoms forming the connection).

```

# **** Hexane ****
Time 0 (ps)
# **** Box Length(X, Y, Z in nanometer) ****
6.0000 6.0000 6.0000
# ****
# **** Record for each atom is in the form:- ****
# **** Index Atom_Type No._of_bonds X Y Z (coords.in nm) ****
# **** Vx Vy Vz (in nm/ps) Indices_of_bonded_atoms ****
# ****
800 Total_No._of_molecules
6 Atoms_in_Molecule_No. 1
1 1 1 0.111082 -3.045910 -2.397419
1.907472E-002 3.0036425E-002 8.420741E-002 2
2 2 2 0.252678 -3.062108 -2.453072
8.328355E-002 -6.4783196E-002 -0.103215 1 3
3 2 2 0.257372 -3.174310 -2.556983
-4.967674E-002 6.488832E-002 0.123231 2 4
4 2 2 0.404221 -3.201894 -2.589903
6.464772E-002 -0.135925 -2.918269E-002 3 5
5 2 2 0.412020 -3.345546 -2.641982
-5.252666E-002 -3.901252E-002 -0.108607 4 6
6 1 1 0.342372 -3.340562 -2.778119
3.707173E-002 7.767803E-003 0.118587 5
6 Atoms_in_Molecule_No. 2
7 1 1 -0.609211 0.470645 0.143018
-6.744394E-002 -2.842826E-002 0.126888 8
...

```

Figure 2.6. A schematic view of the *coordinate* file.

d) *gaussian* file. As mentioned in the section **2.2.1. Force Field**, in IBIsCO, there are two possibilities to define the bond and angle potentials. User can prepare a file called *Gaussian*, which specify the Gaussian parameters (center, total area, and width) have been fitted to the bond lengths and angle distributions¹⁵ (see eq 2.2), or preparing tabulated potentials. Figure 2.7 shows an example of *Gaussian* file. First line of the file is a command line. In second line there are two numbers correspond to total number of lines for the Gaussian parameters of bonds and angles, respectively. For every bond and after that for every angle, the fitting parameters for the Gaussian function are reported. For every Gaussian function, the area (A_i), the width (w_i), and the center of the function (x_i , in Angstrom for bond and in degree for angel distributions) are given in order. The integer number after these values in the same line represents the corresponding order of the bond or angle in the *interaction* file.

```

# line 1:total number of parameter for bonds and angles, line 2:A1 of typ1, line3:W1 of typ1, line4:Xc1 of typ1 and so on...
36 42
0.40838 1 1-2 A1 BOND 1
0.30498 1 1-2 w1
3.02997 1 1-2 x1
0.59862 1 1-2 A2
0.1528 1 1-2 w2
3.25252 1 1-2 x2
0.44847 2 1-3 A1 BOND 2
0.39472 2 1-3 w1
3.50029 2 1-3 x1
0.56877 2 1-3 A2
0.16471 2 1-3 w2
3.6961 2 1-3 x2
.....
.....
0.90725 1 1-2-1 A1 ANGLE 1
52.47201 1 1-2-1 w1
150.9128 1 1-2-1 x1
0.26872 1 1-2-1 A2
9.0752 1 1-2-1 w2
173.4175 1 1-2-1 x2
.....
.....

```

Figure 2.7. A schematic view of the *gaussian* file.

2.4.3. Output Files

There are four major output files (*restart*, *timestep*, *md.out*, and *md.trj*). The *restart* file (in the same format of *coordinate* file) records the particle coordinates and velocities during the simulation for restarting the simulation in case one needs to continue the simulation after the termination of the simulation. It is updated in the simulation every **Naverage** (keyword in the *control* file) time steps.

timestep is the file recording some instantaneous quantities, such as temperature, pressure, energies, box size, density of the system, etc. An example can be found in schematic view of Figure 2.8. The information in this file is updated according to the value of keyword **Nsampling** in the *control* file. All the different quantity values at every **Nsampling** time step are accumulated in *md.out* file one by one with the time sequence. Through the information in *md.out* file, one can monitor the simulation by plotting the quantity values with respect to time.

Step:	1000	
Simulated time:	16230.000000000000	
Total energy:	56414.99213350948	56167.01517088554
Potential energy:	31208.29141341465	31256.08372286729
Kinetic energy:	25206.70072009484	24910.93144801825
Nonbonded energy:	-58539.01035039913	-58315.57830596859
Bond energy:	11853.30677181228	11898.47774619121
Angle energy:	77893.99499200149	77673.18428264471
Torsion energy:	0.000000000000000	0.000000000000000
Temperature:	505.4016070693079	499.4713480048978
Pressure:	1113.258481197264	411.4062351588300
Pressure(x):	1981.277895772100	-76.14742684805717
Pressure(y):	-482.079001038712	669.5585678904297
Pressure(z):	2840.576548858404	640.8075644341185
Pressure(xy):	-348.9951344660246	32.24683712571166
Pressure(xz):	-2214.205343084349	-294.6902826409719
Pressure(yz):	-3101.320658296319	-423.5260413151674
Box volume:	710.7451394412875	710.5795527805291
Box length(x):	8.924241195668259	8.923548026601150
Box length(y):	8.924241195668259	8.923548026601150
Box length(z):	8.924241195668259	8.923548026601150
Mass density:	974.5329010766106	974.7600658593728

Figure 2.8. A schematic view of the *timestep* file.

The trajectory of the simulation is recorded in binary *md.trj* file. The detailed formats and content of this file are the same as YASP³⁴ trajectory file. The readers are referred to YASP³⁴.

Besides the four main output files, there are two additional output files for the RNEMD simulation. They are *md.ntr* and *md.prf*. Schematic views of these two files are shown in Figure 2.9 and Figure 2.10, respectively. There are 8 columns in *md.ntr* file (Figure 2.9), as indicated in the first comment line: the 1st column records the time steps, the 2nd column the corresponding simulation time in picoseconds, the 3rd column the instantaneous momentum flux induced by momentum swaps at the current time step, the 4th column the running average of momentum flux, the 5th column the velocity gradient resulted from linear regression of instantaneous flow velocity profile, the 6th column the velocity gradient from accumulated flow velocity profile, the 7th column the viscosity value calculated from column 3 and 5 using eq 2.19, and the last 8th column the viscosity value from column 4 and 6. All the units of different values in this file are indicated in the first column line in parenthesis, time in (s), flux in (kg. m⁻¹ s⁻²), velocity gradient in (s⁻¹), and viscosity in (cP).

In the *md.prf* file (Figure 2.10), the first line is the comment line to indicate the content of each column. The running average profiles of velocity in *x* direction $v_x(r_z)$ (nm/ps), temperature profile $T(r_z)$ (K) and density profile $\rho(r_z)$ (kg.m⁻³) in each slab after every Num_RNEMD_prof (keyword in

control file) time steps are recording in this file. The corresponding time step (1 integer number) is recorded in the first line after the string of 'STEP': for each record.

1Tsteps,	2Time(ps),	3C_Flux(kg/(m.s ²)),	4Flx(kg/(m.s ²)),	5C_Vgrad(s ⁻¹),	6Vgrad(s ⁻¹),	7C_Visc(cP/mPa.s),	8Visc(cP)
201	0.10050E+1	0.15985E+07	0.15985E+07	-0.14524E+10	-0.14524E+10	0.11006E+01	0.11006E+01
402	0.20100E+1	0.14631E+07	0.15308E+07	-0.23411E+09	-0.84323E+09	0.62495E+01	0.18154E+01
603	0.30150E+1	0.14045E+07	0.14887E+07	-0.79053E+08	-0.58851E+09	0.17767E+02	0.25296E+01
804	0.40200E+1	0.18410E+07	0.15768E+07	0.31065E+09	-0.36372E+09	-0.59265E+01	0.43352E+01
1005	0.50250E+1	0.12054E+07	0.15025E+07	-0.89232E+09	-0.46944E+09	0.13509E+01	0.32007E+01
1206	0.60300E+1	0.14310E+07	0.14906E+07	0.14736E+10	-0.14559E+09	-0.97109E+00	0.10238E+02
1407	0.70350E+1	0.18615E+07	0.15436E+07	-0.40801E+09	-0.18308E+09	0.45624E+01	0.84311E+01
1608	0.80400E+1	0.14379E+07	0.15304E+07	0.75757E+08	-0.15073E+09	-0.18980E+02	0.10153E+02
1809	0.90450E+1	0.16651E+07	0.15453E+07	0.51663E+08	-0.12824E+09	-0.32229E+02	0.12050E+02

Figure 2.9. A schematic view of the *md.ntr* file.

1Slab,	2Rz (nm),	3Vx_prof (nm/ps),	4Temp (K),	5Density (kg/m ³)
STEP: 201				
1	-0.71521778E+01	0.60125281E+01	0.39257731E+03	0.99979524E+03
2	-0.63993170E+01	0.42920007E+01	0.39438580E+03	0.10283476E+04
3	-0.56464562E+01	0.16937409E+02	0.41390358E+03	0.99248623E+03
4	-0.48935954E+01	-0.15806490E+02	0.38141246E+03	0.10327723E+04
5	-0.41407345E+01	-0.55153685E+01	0.38667839E+03	0.10366102E+04
6	-0.33878737E+01	0.43296228E+01	0.40947722E+03	0.10290811E+04
7	-0.26350129E+01	-0.13350337E+02	0.41571489E+03	0.10123358E+04
8	-0.18821521E+01	-0.21810705E+00	0.39291578E+03	0.10207452E+04
.....				
.....				
18	0.56464562E+01	-0.50462303E+01	0.40611340E+03	0.10525485E+04
19	0.63993170E+01	0.25779055E+02	0.36421399E+03	0.10445794E+04
20	0.71521778E+01	-0.77566024E+01	0.38985590E+03	0.10079111E+04
STEP: 402				
1	-0.71521778E+01	0.16050990E+02	0.39899188E+03	0.97138962E+03
2	-0.63993170E+01	0.43672105E+01	0.44799296E+03	0.10243630E+04
3	-0.56464562E+01	0.11197691E+02	0.41865788E+03	0.98828158E+03
4	-0.48935954E+01	-0.18273914E+02	0.40528753E+03	0.10287143E+04
5	-0.41407345E+01	-0.46908008E+01	0.39683218E+03	0.10286410E+04
6	-0.33878737E+01	0.12638402E+02	0.42631918E+03	0.10371970E+04
.....				

Figure 2.10. A schematic view of the *md.prf* file.

2.6. Summary

Details of the MD algorithms, functionalities, user interface, and file formats of the IBIsCO program (version 1.0) have been described in this article. We have found the current version of IBIsCO program a valuable tool in our research especially in coarse-graining simulations of molecule liquid and polymer systems.

2.7. References

- (1) Kremer, K.; Müller-Plathe, F. *Molecular Simulation* **2002**, *28*, 729.
- (2) Praprotnik, M.; Site, L. D.; Kremer, K. *Ann. Rev. Phys. Chem.* **2008**, *59*, 545.
- (3) Reith, D.; Pütz, M.; Müller-Plathe, F. *J. Comput. Chem.* **2003**, *24*, 1624.
- (4) Qian, H.-J.; Carbone, P.; Chen, X.; Karimi-Varzaneh, H. A.; Liew, C. C.; Müller-Plathe, F. *Macromolecules* **2008**, *41*, 9919.
- (5) Karimi-Varzaneh, H. A.; Carbone, P.; Bhargava, B. L.; Balasubramanian, S.; Müller-Plathe, F. *unpublished*.
- (6) Milano, G.; Müller-Plathe, F. *J. Phys. Chem. B* **2005**, *109*, 18609.
- (7) Carbone, P.; Varzaneh, H. A. K.; Chen, X.; Müller-Plathe, F. *J. Chem. Phys.* **2008**, *128*, 064904.
- (8) Carbone, P.; Negri, F.; Müller-Plathe, F. *Macromolecules* **2007**, *40*, 7044.
- (9) Karimi-Varzaneh, H. A.; Carbone, P.; Müller-Plathe, F. *J. Chem. Phys.* **2008**, *129*, 154904.
- (10) Chen, X.; Carbone, P.; Cavalcanti, W. L.; Milano, G.; Müller-Plathe, F. *Macromolecules* **2007**, *40*, 8087.
- (11) Izvekov, S.; Voth, G. A. *J. Chem. Phys.* **2006**, *125*, 151101.
- (12) Qian, H.-J.; Liew, C. C.; Müller-Plathe, F. *Phys. Chem. Chem. Phys.* **2009**, *11*, 1962.
- (13) Groot, R. D.; Warren, P. B. *J. Chem. Phys.* **1997**, *107*, 4423.
- (14) Lowe, C. P. *Europhys. Lett.* **1999**, *47*, 145.
- (15) Milano, G.; Goudeau, S.; Müller-Plathe, F. *J. Polym. Sci., Part B: Polym. Phys.* **2005**, *43*, 871.
- (16) Allen, M. P.; Tildesley, D. J. *Computer Simulation of Liquids*; Clarendon: Oxford, 1987.
- (17) Pagonabarraga, I.; Hagen, M. H. J.; Frenkel, D. *Europhys. Lett.* **1998**, *42*, 377.
- (18) Frenkel, D.; Smit, B. *Understanding Molecular Simulation: From Algorithms to Applications*; Academic: Boston, 1996.
- (19) Chen, L.-J.; Lu, Z.-Y.; Qian, H.-J.; Li, Z.-S.; Sun, C.-C. *J. Chem. Phys.* **2005**, *122*, 104907.
- (20) Berendsen, H. J. C.; Postma, J. P. M.; Gunsteren, W. F. v.; DiNola, A.; Haak, J. R. *J. Chem. Phys.* **1984**, *81*, 3684.
- (21) Müller-Plathe, F. *Phys. Rev. E* **1999**, *59*, 4894.
- (22) Bordat, P.; Müller-Plathe, F. *J. Chem. Phys.* **2002**, *116*, 3362.
- (23) Zhang, M.; Müller-Plathe, F. *J. Chem. Phys.* **2006**, *125*, 124903.
- (24) Terao, T.; Müller-Plathe, F. *J. Chem. Phys.* **2005**, *122*, 081103.
- (25) Smith, W. *Theor. Chim. Acta* **1993**, *84*, 385.
- (26) Pinches, M. R. S.; Tildesley, D. J.; Smith, W. *Molecular Simulation* **1991**, *6*, 51.
- (27) Rapaport, D. C. *Phys. Rev. A* **1987**, *36*, 3288.
- (28) Fincham, D. *Molecular Simulation* **1987**, *1*, 1.
- (29) Todorov, I. T.; Smith, W.; Trachenko, K.; Dove, M. T. *J. Mater. Chem.* **2006**, *16*, 1911.
- (30) Berendsen, H. J. C.; Spoel, D. v. d.; Drunen, R. v. *Comput. Phys. Commun.* **1995**, *91*, 43.
- (31) Brown, D.; Clarke, J. H. R.; Okuda, M.; Yamazaki, T. *Comput. Phys. Commun.* **1993**, *74*, 67.
- (32) Brown, D.; Clarke, J. H. R.; Okuda, M.; Yamazaki, T. *Comput. Phys. Commun.* **1994**, *83*, 1.
- (33) Brown, D.; Minoux, H.; Maigret, B. *Comput. Phys. Commun.* **1997**, *103*, 170.
- (34) Müller-Plathe, F. *Comput. Phys. Commun.* **1993**, *78*, 77.

3. Transferability of Coarse-Grained Force Fields: The Polymer Case

3.1. Introduction

An interesting question for all coarse-graining methodologies is the degree of transferability of the resulting force field between various systems and thermodynamic conditions. Here we present a detailed study of the transferability over different thermodynamic states of a coarse-grained (CG) force field developed using the *Iterative Boltzmann Inversion* method.¹ In this approach the coarse-grained force field is developed from static properties extracted from atomistic simulations performed on systems of small size. Distributions of bond distances, angles, torsions (when necessary), and radial distribution functions, are subjected to a *Boltzmann inversion* to find the corresponding potentials of mean force (PMF). For the PMF to become the effective pairwise potential used in the simulation, it must be *optimized* against the atomistic distributions through an iterative process (*Iterative Boltzmann Inversion* or IBI).¹ This approach restricts the effective coarse-grained interactions between the particles (or beads) to the thermodynamic conditions (temperature and pressure) at which the atomistic reference system has been simulated. Then, intrinsically, the CG potentials can not be transferable. The aim of chapter is to test whether the CG potential (IBI force field) is related to these simulation conditions, and to check its thermodynamic transferability. Such transferability is a key point in the CG simulations because, if the transferability over a certain range is given in practice, the computational effort necessary in the preliminary stage of the atomistic simulation would be considerably reduced.

In the literature, two attempts of using IBI force field mapped at a specific temperature in a broader range of them have been reported. They lead to opposite results: Vettorel and Meyer² faced the problem in studying the crystallization of a coarse-grained model of polyethylene where each chain was composed by 22 monomers. The effect of the temperature changes in the model has been checked by looking at the different effective potentials and monitoring their behaviour as the temperature is modified. They found that the binding potential is temperature independent, while the potentials of mean force obtained by direct *Boltzmann inversion* of the angle distributions depend on the temperature chosen for the mapping. However after the iterative procedure that leads to the *optimized* potentials, the mismatch tends to disappear. Similar results were obtained for the nonbonded interactions. These observations allowed the authors to use the same potential for studying the

crystallization of polyethylene. Ghosh and Faller³ investigated a small organic glass former (ortho-terphenyl) using a mesoscale model composed only by a single interaction centre. The authors used the same IBI potential at different temperatures, and compared the resulting structural properties (in their case only the radial distribution function) with the corresponding atomistic ones. In this way they found that the coarse-grained potential depends not only on the structure but implicitly also on the temperature at which it has been optimized. The two studies differ in the size of the beads (much smaller in the polyethylene case) and in monitoring the temperature effect: Vettorel checks how the shape of the potential function changes and Ghosh monitors how the use of the same potential affects the static properties.

The way the IBI force field is developed makes it capable to keep the identity of the underlying chemistry, but relates it to the simulation conditions at which it has been developed. To investigate the transferability of the IBI force field, we choose the strategy followed by Ghosh comparing the CG structural and dynamical properties with the atomistic reference calculations. Moreover, we investigate if the degree of coarse-graining (how many real atoms per bead) and the size of the macromolecule can affect the transferability. We analyze the polymer case investigating bulk of polystyrene and polyamide-66 whose coarse-grained models differ in the chain length and in the number of atoms lumped in one bead. The effect of temperature and pressure on static, dynamic and thermodynamic properties is tested by comparing systematically the coarse-grain results with the atomistic ones. The comparison is made more interesting by the different chemical and physical properties of the two polymers.

3.2. Mesoscale Models and Simulation Details

In this study, the atactic-PS chain is coarse-grained according to the mesoscale model described in ref.⁴ In this scheme, the bead centre of mass is located on the methylene group (Figure 3.1a) and the beads are identified looking at the relative configuration of two adjacent asymmetric carbon atoms (-CHR- groups). When two consecutive chiral carbon atoms have the same absolute configurations, the bead is called M (meso); if they are different the bead will be labelled R (racemo). In this way, the model is able to account for the tacticity of the polymer chain, and it accurately describes static properties of melt in a broad range of molecular weight.⁵ The atomistic simulations used as references are carried on using the TraPPE united atoms model which reproduces the density of PS over a range of temperatures.⁶ The simulation box, in the coarse-grained and the atomistic stage, is composed by 45 chains, each chain 10 monomers long.

The mesoscale model used for PA-66 involves beads smaller than for PS. The amide function plus one methylene group has been replaced by one bead (labelled A) while two beads (called M3), located respectively at the second and fifth carbon of the hexamethylene unit, are used to describe the aliphatic chain, finally, a third type of bead (M2) is located at the centre of mass of the remaining two central methylene units of the tetramethylene unit (Figure 3.1b). The atomistic simulations are carried out using the force field and following the computational details reported in ref.⁷ The atomistic and coarse-grained simulation boxes are composed by 24 chains each 20 monomers long. So the PS coarse-graining scheme aggregates 8 heavy (non-hydrogen) atoms into one bead, whereas in the PA-66 scheme one bead represents between 2 and 4 heavy atoms.

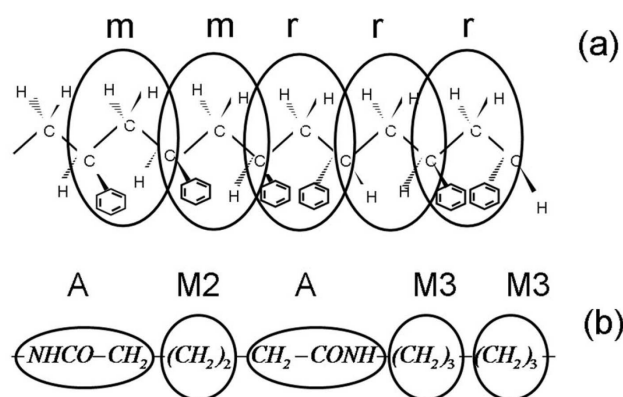


Figure 3.1. Schematic CG mapping scheme. a) polystyrene b) polyamide-66.

One of the aims of this section is to check the transferability of the IBI force field from the temperature where it was developed to another temperature. To address this issue the atomistic and the CG systems are subjected to a continuous cooling at constant pressure. The PA-66 is cooled from 600 K to 300 K with a rate of 0.27 K/ps; while the PS is cooled from 500 K to 300 K with, due to the shorter chain length, a slightly faster rate (0.56 K/ps). At each temperature the production run is of ~35 ns for the atomistic simulations and of ~70 ns for the CG simulations. For developing the IBI force field, we choose one temperature (500 K) for PS and two (300 K and 400 K) for PA-66 and, for the CG simulations, we use the same IBI force field during the entire cooling procedure. Intramolecular distributions, intermolecular radial distribution functions (RDFs), the specific volume (V_{sp}), and the self diffusion coefficients are then extracted at different temperatures from the atomistic NPT trajectories and used as targets for checking the CG results. The time step for the atomistic simulations is 2 fs, while for the CG simulations a time step of 7 fs is used. To keep the temperature constant in the CG simulations we use the Berendsen thermostat with a coupling time of 0.1 ps. The pressure (1 atm) is coupled with a berendsen manostat with a coupling time of 5 ps. The atomistic simulations are run

using the YASP molecular package,⁸ while the CG simulations are carried out with our program IBIsCO,⁹ a MPI parallel software.

As said before, for PA-66 we develop the IBI force field at two temperatures (300 K and 400 K), that are below and above, respectively, the experimental glass transition temperature, and we label the two force fields PA300 and PA400, respectively. For the PS only one force field is developed at 500 K (PS500).

3.3. Results and Discussion

3.3.1. Force Field: Bond Potential and Intramolecular Distributions

In the CG potential usually the torsional component is not included. This approximation has been shown to be suitable for the PS model used in the present paper.⁴ Similar checks have been done on PA-66 calculating, according to the proposed CG scheme, the distributions of the dihedral angles between the beads. The resulting histograms are flat enough to predict a torsional potential so weak as to be neglected. The bonded part is thus reduced to stretching and bending potentials between the bonds connecting the beads. Hereafter, when we will speak about bonds, angles or torsions we will refer only to those connecting beads and not atoms.

In order to test the IBI force field transferability, distributions of distances and angles are monitored with the temperature changes; then, the results obtained by the atomistic and coarse-grain simulations are compared.

The trend with the temperature of the distributions of the angle M3-M3-A extracted from the atomistic trajectories for the PA-66 model is shown in Figure 3.2a. Not surprisingly, for lower temperatures the distributions become sharper showing that the number of populated conformational states decreases when the temperature decreases. Although we are looking at angle distributions, speaking of conformers is appropriate because these angles encompass atomistic torsions. It is worth to notice that same behaviour found in the atomistic simulations is reproduced by the CG simulations even if the CG potential exhibits slightly broader distributions at high temperatures (Figure2b).

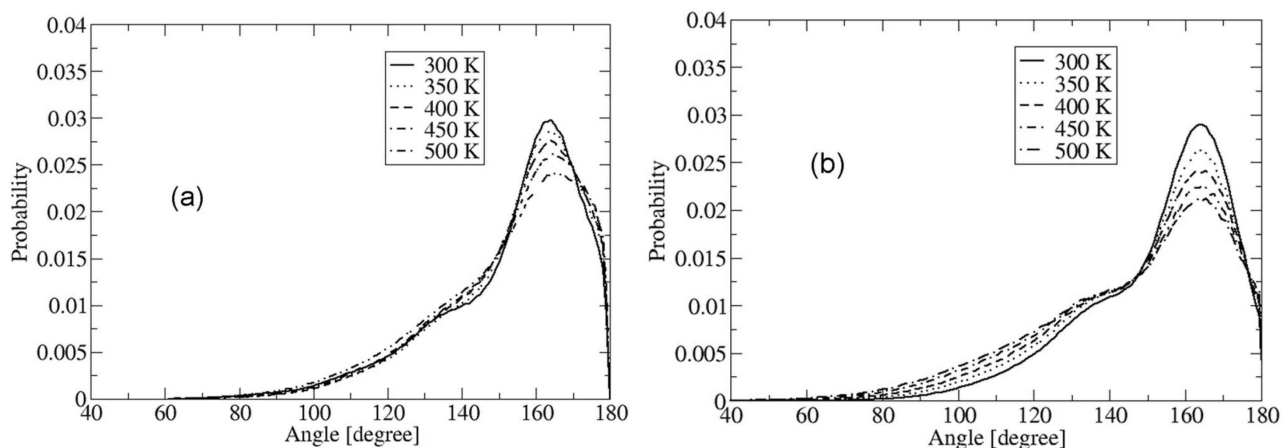


Figure 3.2. Polyamide-66: Distribution of M3-M3-A angle at different temperatures from: a) atomistic simulations; b) CG simulations (PA300).

We compare directly the angle distributions obtained from the two simulations at a temperature ($T=500$ K) far from the *optimization* one in Figure 3.3. It is shown that the distribution of one angle of the PA-66 backbone extracted from the atomistic simulations matches very good with that obtained from the CG trajectory run at 500 K with the two IBI force fields (PA300 and PA400). Same good agreement can be observed for the other angles at different temperatures.

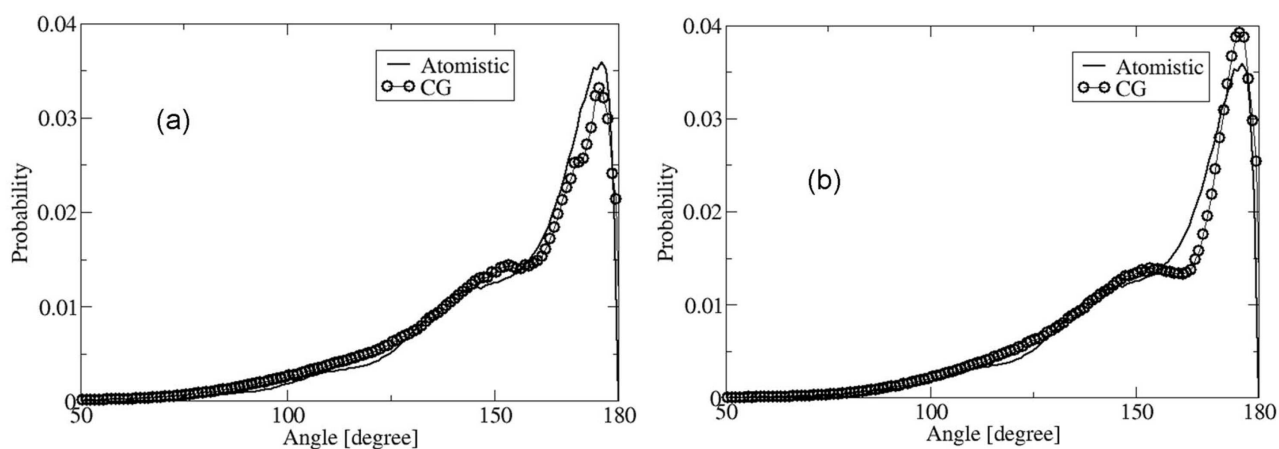


Figure 3.3. Comparison between atomistic-CG distributions for the angle M3-M3-A in PA-66 ($T=500$ K) a) using the PA300 force field, b) using the PA400 force field.

Since the coarse-graining scheme for PS involves larger beads than PA-66, the angle distributions between them are little affected by the temperature changes. In Figure 3.4a the atomistic distributions of the MMM angle of the PS model are reported at different temperatures. For temperatures greater than 400 K, no differences are visible in the atomistic distribution, but for temperatures lower than 400 K the major peak (at 120 degree) becomes sharper and only this state is fully populated. The behaviour is quite different if we look at the same distribution extracted from the

CG trajectories run with the PS500 force field. The trend is in the right direction: lower temperatures give sharper distributions, but at 350 K, the shoulder at 160 degree is still visible, showing that the CG model is not able to capture small intramolecular structural changes (Figure 3.4b).

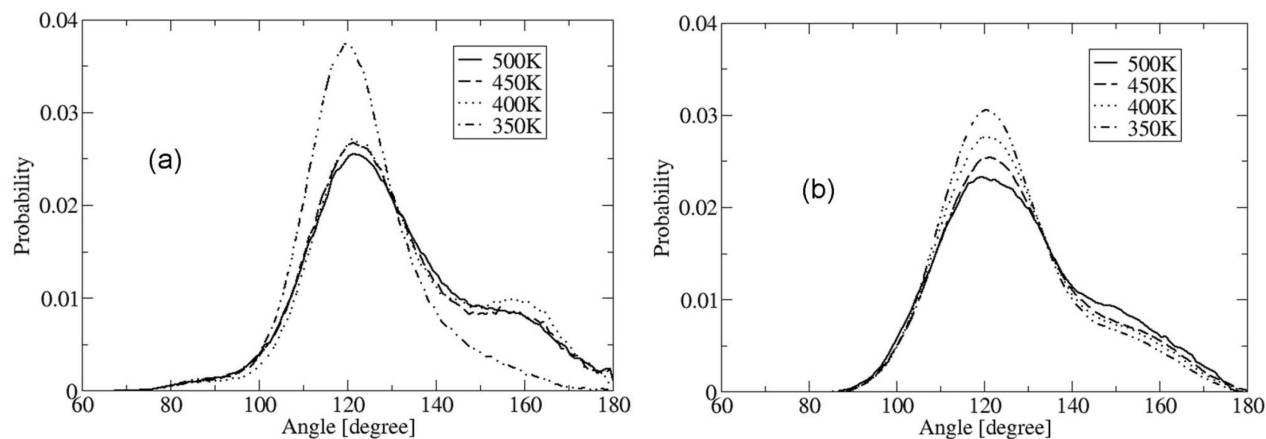


Figure 3.4. Comparison between the M-M-M angle distribution for PS obtained from: a) atomistic simulations; b) CG simulations.

The different behaviour of the two polymer models becomes also evident looking at the distribution of the bond distances. As for angles, PA-66 bond distances are influenced by the temperature changes while the longer PS bonds are very little affected. The changes in the distance distributions, as well in those of the angles, are well described by both PA IBI force fields (PA300 and PA400) (not shown).

3.3.2. Force Field: Nonbonded Interactions and Interchain Distributions

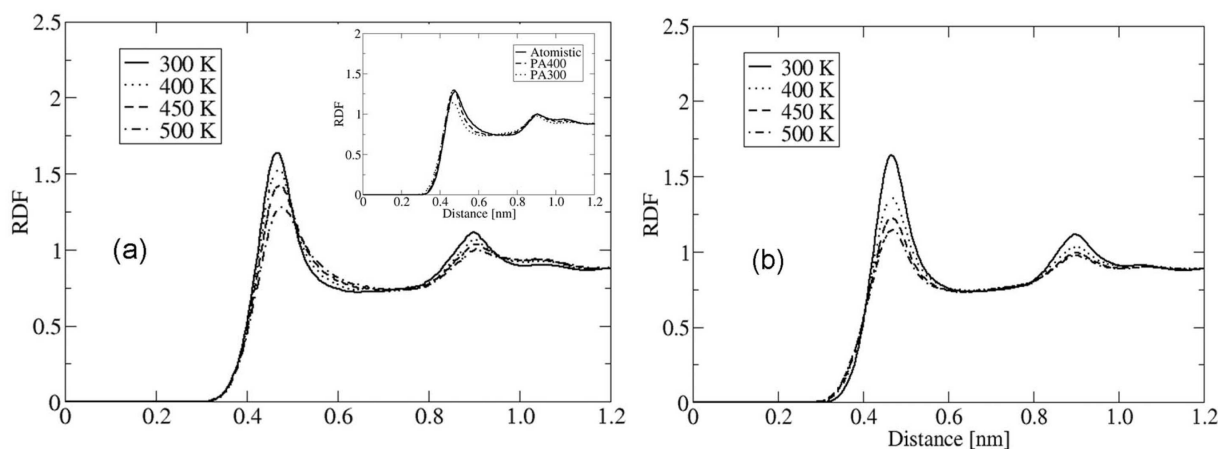


Figure 3.5. Radial distribution functions between the A beads for the PA-66 model, as obtained from a) atomistic simulations, b) CG simulations (PA300). The inset shows the matching between the atomistic and CG A-A (PA300 and PA400) radial distribution function at 500 K.

The nonbonded part of the IBI force field is built starting from the interchain pair correlation functions (RDF) among every type of bead pairs. In the atomistic simulations of PA-66, it is observed that, with increasing temperature, the first two peaks of the amide-amide (A-A) RDF decrease in height and broaden slightly toward larger distances (Figure 3.5a). This change can be the indication of the breaking of the hydrogen bonds among the amide groups.¹⁰ Same behaviour is found in the CG simulations for both IBI potentials (Figure 3.5b where only the results corresponding to the PA400 force field are reported), showing that the CG model has in its structural properties the “memory” of the presence of hydrogen bonds. Moreover, a direct comparison between the atomistic and CG RDFs extracted from the trajectories run at 500 K, shows an acceptable agreement for all the nonbonded interactions, especially using the PA400 force field (inset Figure 3.5b).

Monitoring the RDFs of polystyrene as a function of temperature, a change in the structure is evident for temperatures below 400 K. Figure 3.6 shows the RR-RDF calculated at different temperatures. Looking at the atomistic results (Figure 3.6a), it is clear that at 400 K a minor change in structure begins, which becomes more evident at 350 K. This change is observed also for the other two nonbonded interactions (MR, MM, not shown). On the contrary, the calculations performed on the CG trajectories show that, although the IBI potential is able to reproduce some features (for example, the small peak at about 0.4 nm appears at 400 K in both simulations), for temperatures below 400 K atomistic and CG RDFs are strongly different (Figure 3.6b). In order to understand the nature of the structural changes occurring when the temperature decreases and to investigate the deficiencies of the CG model, we calculate the X-ray structure factor (S_q) at 500 K and 350 K comparing the spectra with the experimental results. The experimental X-ray scattering pattern of atactic polystyrene is mainly characterized by two peaks: one at around $q=0.75 \text{ \AA}^{-1}$ (called “polymerization peak”) and a second one laying at higher q (around 1.4 \AA^{-1}), called “amorphous peak”. One of the striking features of polystyrene is that the “polymerization peak” has unexpected temperature behaviour: it increases in intensity when temperature increases. Molecular dynamic calculations have clarified the nature of this phenomenon.¹¹ It has been shown that the “polymerization peak” is primarily due to the intermolecular backbone-backbone correlations, while the “amorphous peak” is mainly due to intermolecular phenyl-phenyl correlations and to an important intramolecular (nearly temperature independent) phenyl-phenyl and phenyl-backbone interactions. When the temperature increases the phenyl-phenyl intermolecular component shifts to lower q increasing the polymerization peak intensity. Hence, the anomalous temperature dependence of the “polymerization peak” is not indicative of increasing order with increasing temperature, but only of a shifting to lower q of that part of the amorphous peak which is due to the intermolecular interactions.¹¹ The results of the calculations performed on the atomistic trajectories agree with the experimental data showing an increase of the “polymerization peak”

(around 0.75 \AA^{-1}) and a shift to lower q for the “amorphous peak” when the temperature rises. On the contrary, the X-ray pattern calculated from the CG trajectory run at 500 K shows the “polymerization peak” at $q=0.75 \text{ \AA}^{-1}$, but it does not present the “amorphous peak” at higher q . Moreover the X-ray spectrum calculated from the CG simulation at 350 K displays peaks that cannot be assigned (inset of Figure 3.6a). The explanation for these results lies in the different interactions responsible to the different peaks: the “polymerization peak” is mainly due to the backbone-backbone interactions which are, at the *optimization* temperature, well described in the CG model (the IBI potentials are developed starting from the RDFs for the methylene groups present in the main chain), while the phenyl-phenyl interactions, responsible of the “amorphous peak” are only partially considered indirectly in the inter-RDFs. When the temperature decreases (350 K), the IBI potential fails in describing the backbone-backbone interactions (as it will be clearly shown investigating the trend of the density see next section “Static properties”) and none of the peaks in the X-ray spectrum can be assigned.

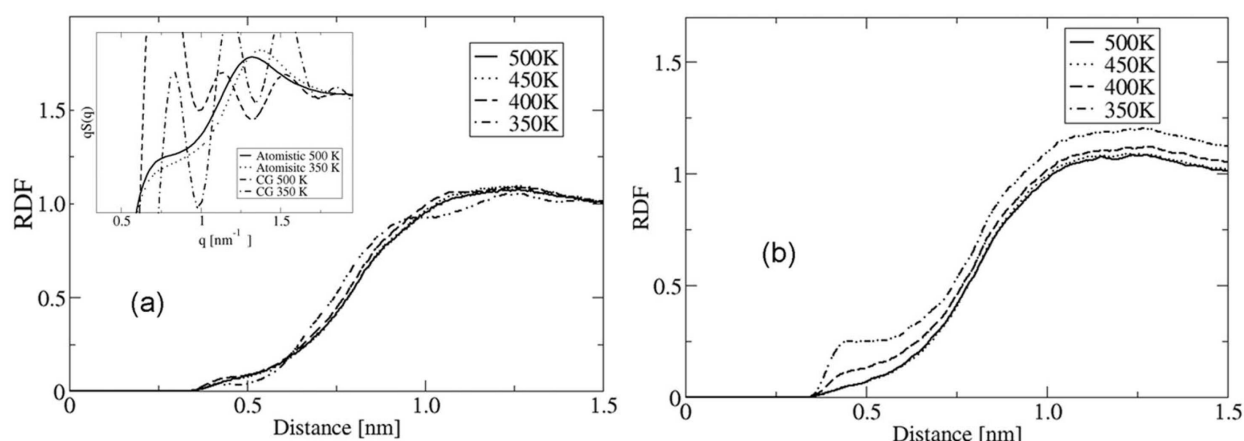


Figure 3.6. Radial distribution functions between the M beads for PS model calculated from the a) atomistic; b) CG (PS500) simulations. The inset shows the structure factor calculated at two different temperatures from the atomistic and CG simulations of PS.

3.3.3. Static Properties

In the previous paragraphs, we have investigated how closely the IBI force field is able to reproduce, at different temperatures, the structural features on which its development was originally based. We have found that for PS the transferability is allowed in a smaller temperature range than for PA-66 in whose case the IBI potential is able to describe correctly the structural properties in the entire range of temperatures under investigation (300-600K). Now we want to test the reliability of the IBI force field in describing static properties such as gyration radius, end to end distance, but also phase transition temperature like the glass transition temperature.

A common way to validate polymer model is to calculate from the trajectories the change of the density with the temperature. Plotting the inverse of the density (specific volume) as a function of temperature is the usual way to calculate the glass transition temperature (T_g). The specific volume (V_{sp}) changes almost linearly with the temperature and, in the vicinity of the transition temperature, an evident variation in the slope of the interpolating lines occurs. This slope represents the thermal expansion coefficient (α) of the material respectively in the glass and in the rubber phase. An interesting point is to check if the IBI force field is able to describe correctly the glass phase transition. For PA-66 both potentials give a T_g of ~ 380 K in reasonable agreement, considering the coarser model, with the experimental value of ~ 330 K and the atomistic simulation results of ~ 330 K.⁷ The corresponding thermal expansion coefficients (in the glassy and in the melt phase) is related to the response of the material to the temperature changes. The values of thermal expansion coefficients (α), the density, and other properties of the polyamide are reported in Table 3.1 and compared with available experimental values. We observe that both CG and atomistic densities are in agreement with the experimental ones.

Table 3.1. Dynamic and static properties for PA-66 and PS as obtained by the atomistic and CG simulations. For PA-66 all CG results are obtained using the PA400 force field. Similar results are obtained using PA300. The temperature of the analysis is reported in parenthesis.

	PA66			<i>a</i> -PS		
	Expt.	Atomistic	CG ^a	Expt.	Atomistic	CG
Density (g/cm ³)	1.07–1.1 (573–533 K) ^b	1.1 (300 K)	1.09 (300 K)	0.96 (500 K) ^c	0.96 (500 K)	0.95 (500 K)
Density (g/cm ³)	0.96 (550 K) ^b	0.98 (550 K)	0.99 (550 K)
R_g (Å)	27 ^d	30.47 ± 0.04 (300 K)	26.76 ± 0.09 (300 K)	5.8 ^e	6.46 ± 0.04 (500 K)	5.11 ± 0.09 (500 K)
End-to-end distance (nm)	6.4 ^d	7.41 ± 0.03 (300 K)	6.20 ± 0.05 (300 K)	...	1.40 ± 0.05 (500 K)	1.30 ± 0.04 (500 K)
α_{rubber} (K ⁻¹)	5.9 × 10 ^{-4f}	5.4 × 10 ^{-4g}	4.1 × 10 ⁻⁴	5.6 × 10 ⁻⁴	5.7 × 10 ⁻⁴	...
α_{glass} (K ⁻¹)		2.8 × 10 ^{-4g}	1.9 × 10 ⁻⁴			
T_g (K)	330 ^f	330 ^e	380	370 ^h	360	...
D (cm ² /s)	...	1.8 × 10 ⁻⁸ (500 K)	4.7 × 10 ⁻⁷ (500 K)	...	1.3 × 10 ⁻⁶ (500 K)	7.0 × 10 ⁻⁵ (500 K)

^a The CG data are calculated using the force field optimized at 400 K (namely PA400). Very similar results are obtain using the force field PA300 with the exception of the diffusion coefficient that is $5.5 \cdot 10^{-7}$ cm²/s (see text)

^b Ref. ¹²

^c Ref. ¹³

^d Ref. ¹⁴

^e Gyration radius measured for M_w smaller than the simulated one. Ref. ¹⁵

^f Ref. ¹⁶

^g These data are reported in Ref.⁷ from which we took the force field parameters

^h Ref. ¹²

The same procedure for checking the transferability of the IBI potential is followed for the PS. Decreasing the temperature, the CG density does not increase linearly, but for temperatures above 430 K it oscillates around the initial value of 0.95 g/cm^3 corresponding to 500 K. This value of density is acceptable for such range of temperatures and it is within the experimental error. For temperatures below 430 K the density starts to decrease monotonically quite slowly reaching a value of 0.88 g/cm^3 at 350 K (see Figure 3.7). This unphysical temperature-dependence of the density (for temperatures lower than 430 K) may be attributed to two factors both related to the dimension of the bead. Firstly, as it is pointed out in the previous paragraph, the backbone-backbone interactions are not sufficiently accurate to follow the structural changes occurring when the temperature decreases. As a matter of fact, although the mapping scheme used in the present case is very efficient in describing the structure of PS at the *optimization* temperature (500 K),⁴ the model averages in only one interaction type (MM, MR or RR depending on the stereochemistry of the dyad) many degrees of freedom (like the phenyl-phenyl interactions) which become important when the temperature decreases. The second reason may lie in the beads's shape. Because the CG force field is developed starting from the radial distribution functions the beads are all described by spheres and, in the particular case of PS, all the beads have also same dimension and mass. This approximation neglects, for instance, the phenyl rings reorientation that assumes more importance in decreasing the temperature. We have to point out, anyway, that the qualitatively wrong temperature-dependence of the density for temperatures lower than 430 K, cannot be considered a peculiar trend of the CG model and it does not give any particular information. With the sole purpose to check the change of the density with the temperature, we develop for the PS a CG force field *optimized* at 350 K (below the glass transition temperature). We find that the density again does not follow the correct trend when the temperature is too far from the *optimization* one. In this case, anyway, the density oscillates around its initial value within the entire temperature range (300-500 K). This result suggests that no explanations for the qualitatively wrong trend of the density found in applying the PS500 force field at temperatures lower than 430 K can be drawn. Moreover, it is worth to notice that, since the CG force field turns out to be density dependent, in the temperature range where the density is wrong the pressure calculated using the virial formula cannot be considered correct.

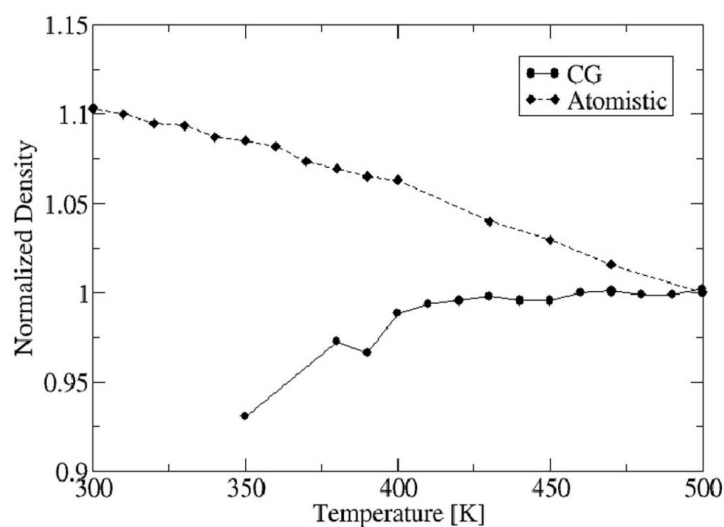


Figure 3.7. Density change with the temperature for the atomistic and CG simulations of PS. The density values have been normalized with respect to the reference value at 500 K.

The reliability of the atomistic simulations is a crucial point in the development of the IBI force field. To avoid any possible errors, we monitor the density change as a function of the temperature. The TraPPE force field turns out to be a reliable atomistic force field. The resulting T_g is ~ 360 K against an experimental value of ~ 370 K, and the thermal expansion coefficient calculated in the melt phase is $5.7 \cdot 10^{-4} \text{ K}^{-1}$ closely matching the experimental value of $5.8 \cdot 10^{-4} \text{ K}^{-1}$.¹² All other structural parameters calculated from the atomistic simulations are in agreement with the experimental values (see Table 3.1) and with previous simulations results.⁴

These results show that the IBI force field of PS is a reliable force field at the temperature at which it has been developed (*optimization* temperature, 500 K) and over a small temperature range of about 80 K below. In order to check whether the limited transferability of the CG force field for PS is further affected by the polymer chain length (the chain length of PS model is shorter than the PA one), we double the molecular weight of the original chain, and we study the behaviour of the longer chain (20 monomers), subjected to the same cooling scheme used for the shorter one. We find similar trend for the density as in the case of the shorter chain: it oscillates around the initial value above a temperature of ~ 430 K, and then decreases slowly. The insensitivity of the volumetric behaviour of PS to its molecular weight, agrees with previous simulation studies conducted on unentangled PS melt (up to 30 monomers each chains)⁴ which showed that PS of such chain length behaves already Gaussian.

3.3.4. Dynamic Properties

The IBI potential is developed starting from *structural* data so that such force field reproduces naturally static properties very well. The possibility to describe with the same accuracy the dynamic behaviour of polymer melts (for instance, the zero-shear viscosity)¹⁷ is a target yet to be achieved. The reason is a “soft” CG potential from whose minima the molecules can easily escape. The soft potential is the main reason of the faster dynamics of the CG models compared with the atomistic ones.

We analyze the dynamic properties of our CG model PA-66 with a two-fold aim: firstly to check if the IBI force field describes correctly the dynamical behaviour and the change of dynamic properties (for instance the self-diffusion coefficient D) as a function of the temperature, secondly to check if the size of the beads (the degree of coarse-graining) has an influence on the speed-up of the CG dynamics. We calculate the centre-of-mass diffusion coefficient D ($6D = \lim_{t \rightarrow \infty} \frac{d}{dt} \langle |R(t) - R(0)|^2 \rangle$) of PA-66 at all simulated temperatures. A comparison of the atomistic and CG diffusion coefficients for PA-66 is reported in Figure 3.8. The behaviour of D with temperature is examined in Figure 3.8a where it is shown that the atomistic as well as the CG simulations exhibit the same trend typical of the Arrhenius law, $D \cong \exp(-E_A/k_B T)$, with the temperature. It must be noted, anyway, that the decrease of D with T increasing is faster in the atomistic simulations than in the CG one. In order to verify that the dynamics of the CG model is well described at the *optimization* temperature, we use only the IBI potential developed at 400 K because the D calculated at 300 K (below the T_g) is effected by a big error. The Rouse model predicts for unentangled polymer a linear dependence of D with the chain length. Since the chain length of the PA-66 model is already very close to the entanglement one,¹⁴ to verify the Rouse picture we half the chain length and on this new model we run CG MD simulations at 400 K. We find $D = (3.9 \pm 1.3) \cdot 10^{-7} \text{ cm}^2/\text{s}$ for the shorter chains (10 monomers) and $D = (1.9 \pm 0.7) \cdot 10^{-7} \text{ cm}^2/\text{s}$ for the original model (20 monomers), results that agree well with the Rouse prediction. The ability of the IBI potential to depict correctly the dynamics of polymer melt at temperatures higher than the *optimization* one can be checked exploiting again the Rouse theory. Thus, we check the slope of the MSD (calculated for the M2 beads sited in the central part of the polymer chain) along the time for the simulation run at 500 K. We find that, for both the IBI force fields, the PA-66 model follows the Rouse theory and, monitoring the MSD, it is possible to identify the three typical diffusive regimes: the ballistic one at shortest time, followed by the subdiffusive regime and, at largest time, by the free diffusion regime. These results prove that the dynamics of the CG models can be well described using the Rouse theory at the *optimization* and at higher temperature.

In Figure 3.8b the ratio among the CG and atomistic D is reported at different temperatures. This ratio represents the *scaling factor* necessary to rescale the fast dynamics of the CG model to the atomistic one. Two important results are visible in the Figure: first the diffusion coefficients calculated using both IBI force fields are much higher than the corresponding atomistic ones for temperatures lower than 400 K, becoming very similar when temperature exceeds 500 K. This indicates that the *scaling factor* accounting the faster CG dynamics is temperature dependent. The explanation for such dependence may be ascribed to two different factors: At low temperature (400 K) the dynamics of the atomistic systems is dominated by the presence of hydrogen bonds between the amide groups. Experimentally, indeed, it has been found that for temperature below 500 K, when the crystal phase is present, the amide hydrogen bonds are relatively immobile, reducing drastically the chain mobility.¹⁸ Although our atomistic simulations do not show any crystalline phase, the presence of the hydrogen bonds can be roughly estimated with simple geometrical analyses. We base our H-bond analysis on two criteria: the distance between the oxygen (acceptor) and the hydrogen bonded to a nitrogen (donor) being smaller than 0.3 nm and the life time of the O...H pair distance. We consider hydrogen bonded the O...H couple whose distance is less than 0.3 nm for a time longer than 600 ps. Following this criteria we find that H-bonds are present in the atomistic systems at 400 K but not at 500 K. Thus, we impute the faster CG dynamics found at low temperature to the lack of hydrogen bonds between the amide groups. More analysis on the effect of H-bonds on the dynamics of the atomistic and the CG model of PA-66 is given in chapters 4 and 5.

At high temperature (higher than 500 K) the *scaling factor* decreases further and converges to a value of ~ 6 (for the PA400 force field) for temperatures higher than 550 K. In this case the small *scaling factor* and its convergence at high temperature may be due to the little relevance that the details of the potential energy surface takes in increasing the temperature, when only the free volume and the non-crossability of the polymer chains matter. Unfortunately, to determine this temperature *a priori*, knowing the number of atoms lumped in one bead is not of trivial solution.

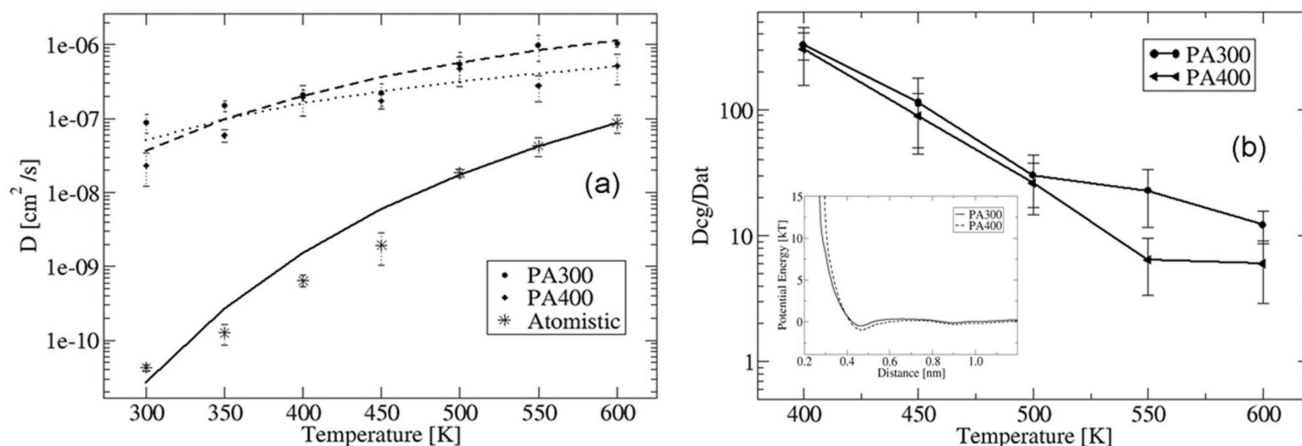


Figure 3.8. PA-66 self diffusion coefficients (with their errors) as a function of the temperature. The lines represent the Arrhenius plot fitting the: atomistic (solid line), PA400 CG (dashed line), PA300 CG (dotted line) results; b) temperature dependence of the ratio between atomistic and CG diffusion coefficients for PA-66. The inset underlines the difference in softness of the two force fields PA400 and PA300 in the case of A-A interactions.

The second important observation is that the two IBI force fields have a different dynamics: the one optimized at 300 K (PA300) is always slightly faster than the one optimized at 400 K (PA400). This difference in speed arises from the shape of the potential functions (see inset Figure 3.8b). The potential obtained by the Boltzmann inversion procedure (the first guess of the iterative process) is roughly the mirror image of the corresponding RDF: higher peaks in the RDFs cause deeper holes in the potentials. Even if the RDFs calculated at 300 K have peaks higher than the ones calculated at 400 K, the corresponding optimized potential is softer (inset of Figure 3.8b). The initial guess function (the directed inverted RDF) is indeed a PMF containing the many-body cooperative effects arising from the packing of particles in the materials. The iterative process suppresses the entropy part and converts the PMF in a pure *potential* enables of following the dynamics of the system at different temperatures.

In the case of PS we find another interesting result. We compare D calculated using the CG force field reported in Ref.⁴, with the one calculated with our IBI potential (PS500). Both force fields give at 500 K a similar diffusion coefficient: $\sim 1.2 \cdot 10^{-4} \text{ cm}^2/\text{s}$ from Ref.⁴ and $0.7 \cdot 10^{-4} \text{ cm}^2/\text{s}$ from PS500. This result shows that, for the same CG mapping scheme, force fields developed independently (both following the *Iterative Boltzmann Inversion* procedure) and whose shape differs, give similar static and dynamic properties at sufficiently high temperatures, where the global chain architecture matters but energetic details do not.

Although a direct comparison between PS and PA-66 behaviour is quite difficult due to their different chemical nature, it is worth noting that if we compare the D of the two CG models at a temperature enough high and equally far away from their respective T_g (i.e. at 500 K for PS and 520 K

for PA-66), the CG PS turns out to have a bigger *scaling factor* (~55) than the CG PA-66 (~26 at 500 K and ~6 at 550 K). This result may be related to the dimension of the beads. The polyamide is, indeed, described by a quite detailed CG model in which the biggest bead contains 7 atoms (the smallest 4), while a polystyrene bead contains 18 atoms. As it was found for the static properties, the chain length does not affect this result. We have already shown, indeed, that the zero shear viscosity of low molecular weight PS is linearly dependent on the molecular weight (Rouse behaviour).¹⁷ Then for unentangled chains the *scaling factor* turns out to be chain-length independent.

3.3.5. Density Dependence of the Force Field

At temperature and density where the force field is developed (*optimization* conditions), the IBI force field is tuned to reproduce the atomistic pressure. The pressure is optimised by adding a weak linear potential term to the attractive long-range part, the so-called ramp potential. An interesting further check is whether the IBI potential is capable to reproduce the compressibility of the material, where the isothermal compressibility is defined as

$$K_T = -\frac{1}{V} \left(\frac{\partial V}{\partial P} \right)_T \quad (3-1)$$

where V is the volume of the simulation box, T is the temperature and P is the pressure. To address this issue, we perform simulations in NPT ensemble varying only the pressure and monitoring the resulting density. In Figure 3.9 we present the densities obtained applying different pressures on PS and PA-66 models. The simulations are carried out for the two CG models at the corresponding *optimization* temperatures: 500 K for PS and 400 K for PA-66 using the IBI force field PA400. For PA-66 we do not perform any simulations at 300 K because this temperature is well below the T_g , and the material is already in the glass phase. For PS, it is clear from the Figure that, even if the IBI potential has been subjected to a pressure optimisation, varying the pressure it fails to reproduce the correct compressibility. This confirms once more that the coarse-grained model of PS is much softer than to the atomistic one. This result is consistent with low viscosity values predicted for the CG model.¹⁷ The deviations from the atomistic trend for PA-66 are less marked and the finer model of PA-66 turns out to be again better transferable.

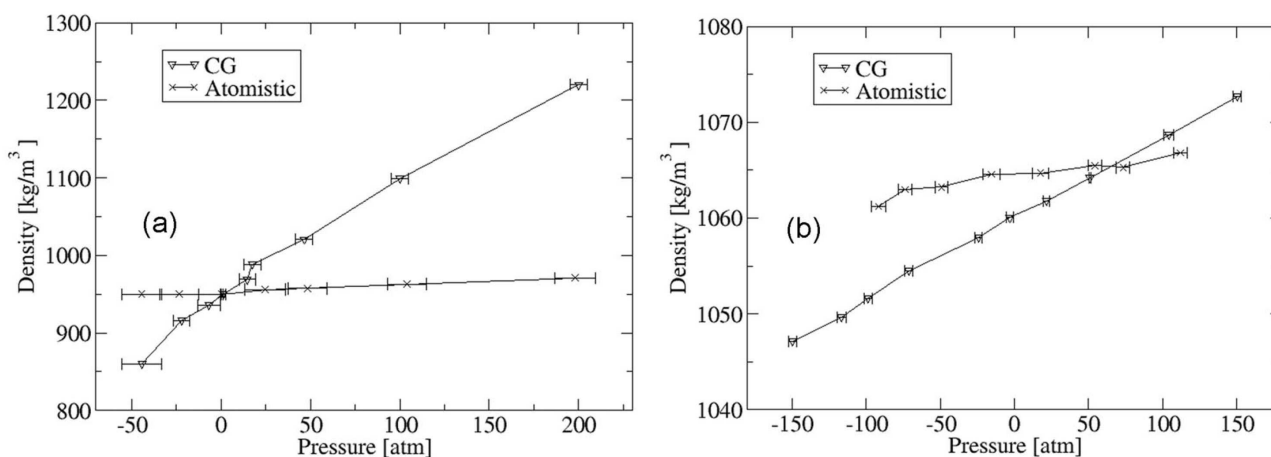


Figure 3.9. Density versus pressure for a) PS at 500 K (PS500) and b) PA-66 at 400K (PA400). The lines are drawn only to help the eyes to follow the point trend.

Using eq 3.1 we calculate K_T for the atomistic and CG models under investigation. For the PS the atomistic K_T ($9.3 \cdot 10^{-7} \text{ kPa}^{-1}$) turns out to be in good agreement with the experimental value ($8.7 \cdot 10^{-7} \text{ kPa}^{-1}$ at 493 K)¹² while the corresponding CG value ($1.6 \cdot 10^{-5} \text{ kPa}^{-1}$) is more than two orders of magnitude smaller than the atomistic one. The latter result is a further proof of the “soft” response of the CG PS model to the pressure changes. As it can be easily inferred from Figure 3.9 for PA-66 the isothermal compressibility calculated from the atomistic and CG simulations agree better than for PS. We find a value of $2.1 \cdot 10^{-7} \text{ kPa}^{-1}$ for the atomistic model and $7.9 \cdot 10^{-7} \text{ kPa}^{-1}$ for the CG one. Both values can be well compared with the experimental one of $7.3 \cdot 10^{-7} \text{ kPa}^{-1}$ (measured at 513 K).¹² For the CG PA-66, following the same method, we calculate K_T at a temperature higher than the *optimization* one (550 K). We find a value of $1.9 \cdot 10^{-7} \text{ kPa}^{-1}$ for the atomistic model and $5.7 \cdot 10^{-7} \text{ kPa}^{-1}$ for the CG one against an experimental result of $8.8 \cdot 10^{-7} \text{ kPa}^{-1}$.¹² The small change of the compressibility (experimental and calculated) with the temperature shows that it is not significantly influenced by the presence of the hydrogen bonds. Moreover, the good agreement at high temperature between the experimental and calculated result confirms the robustness of the IBI transferability in the case of PA-66.

3.4. Conclusions

In this contribution we have tested the transferability of coarse-grained force fields (IBI force field) constructed on the basis of structural distributions derived from atomistic simulations. The force field is *optimized* using the so called *Iterative Boltzmann Inversion* (IBI) procedure until the coarse-grained distribution functions match the atomistic ones. Moreover, with a modified *optimization*

procedure the IBI force field reproduces also the atomistic pressure. In the development of the IBI potential, temperature and pressure enter both in the *optimization* procedure and in the target distributions, which are extracted from atomistic simulations run at specific thermodynamic conditions. In order to check the transferability over different state points, we run several CG-MD simulations at different thermodynamic conditions (pressure and temperature) with a single IBI potential developed at a specific state point. The CG results have been compared with the atomistic ones set as target. The reliability of the IBI force field has been tested against structural properties (bond distance, angle distributions, radial distribution functions), static properties (gyration radius, end to end distances), dynamic properties (mainly self diffusion coefficient) and thermodynamic properties (T_g and isothermal compressibility) for bulk of polystyrene (PS) and polyamide-66 (PA-66).

The CG models describing the two polymers differ in the degree of coarse-graining (the number of real atoms lumped in one bead) and in the chain length. We have found that the finer model used for PA-66 allows to use the IBI potential over the entire temperature range of interest (300-600 K). In contrast, for PS the analysis of the intramolecular distribution such as distances and angles, as well as the RDFs showed that the PS IBI force field can be confidently applied only in a small temperature range (~ 80 K) around the *optimization* temperature. Within this range, density and static properties of the PS bulk are in reasonable agreement with experimental and atomistic values; but for temperatures further from the *optimization* point, the IBI potential cannot correctly reproduce the behaviour of the polymer. In contrast, for PA-66 all properties investigated showed good agreement with the experiments as well as with the atomistic results. Both force fields developed for PA-66 turned out to be very robust and transferable between different temperatures: the changes in the intra and inter molecular distributions are comparable with the atomistic data. Moreover it was possible to calculate the CG T_g and the thermal expansion coefficients both in good agreement with the experimental values. All geometrical properties calculated from the CG trajectories matched with the experimental data available.

Studying the dynamical properties the chemical differences among the two polymers under investigation became more evident and affected the results for low temperatures. Despite this, general observations at high temperatures could be drawn. We have shown that for a defined mapping scheme, IBI potentials developed independently and with different shape, give comparable self diffusion coefficient for high enough temperature. At high temperatures the specifics of a force field become unimportant and only global properties such as excluded volume and bead connectivity prevail. We have also shown that the *scaling factor* measuring the speed up of the CG model depends on the simulation temperature. For PA-66, we have found that at low temperature (400 K) the presence of the hydrogen bonds between the amide group in the atomistic reference systems strongly slows down the

dynamics leading to a very high *scaling factor* (~ 300) due to the absence of the hydrogen bonds in the CG model. As the temperature increases (higher than 500 K), when the hydrogen bonding network is broken, the atomistic a CG dynamics can be better compared. We have shown that increasing the temperature the *scaling factor* reduces and converges to a value of ~ 6 for temperature equal and higher than 550 K. Comparing directly the PS and PA-66 models, we also have shown that, at similar thermodynamic conditions, the magnitude of speed up of the CG dynamics over the atomistic dynamics may be related to the number of degrees of freedom lumped into the beads. Of course the identification of a *scaling factor* independent from the temperature would be an important improvement in understanding the transferability of the CG force field and its dependence on the degree of freedoms neglected. An interesting way to achieve this goal could be to use the mode coupling theory and to compare different modes obtained analyzing the atomistic and CG models.

A further test had been carried on for checking the IBI force field dependence on the density. The results show that the isothermal compressibility is overestimated by the less transferable IBI force field (PS500), leading to a model too “soft” compared with the experimental result. On the contrary for PA-66 the agreement between the atomistic, CG and experimental K_T is satisfactory at the *optimization* temperature and at higher one.

Finally, we have shown that the chain length does not influence the force field transferability between different thermodynamic conditions.

3.5. References

- (1) Reith, D.; Pütz, M.; Müller-Plathe, F. *J. Comput. Chem.* **2003**, *24*, 1624.
- (2) Vettorel, T.; Meyer, H. *J. Chem. Theory Comput.* **2006**, *2*, 616.
- (3) Ghosh, J.; Faller, R. *Mol. Simul.* **2007**, *33*, 759.
- (4) Milano, G.; Müller-Plathe, F. *J. Phys. Chem. B* **2005**, *109*, 18609.
- (5) Spyriouni, T.; Tzoumanekas, C.; Theodorou, D.; F. Müller-Plathe; Milano, G. *Macromolecules* **2007**, *40*, 3876.
- (6) Harmandaris, V. A.; Adhikari, N. P.; Vegt, N. F. A. v. d.; Kremer, K. *Macromolecules* **2006**, *39*, 6708.
- (7) Goudeau, S.; Charlot, M.; Vergelati, C.; Müller-Plathe, F. *Macromolecules* **2004**, *37*, 8072.
- (8) Müller-Plathe, F. *Comput. Phys. Commun.* **1993**, *78*, 77.
- (9) Karimi-Varzaneh, H. A.; Qian, H.-J.; Chen, X.; Carbone, P.; Müller-Plathe, F. *In Preparation* **2009**.
- (10) Karimi-Varzaneh, H. A.; Carbone, P.; Müller-Plathe, F. *J. Chem. Phys.* **2008**, *129*, 154904.
- (11) Ayyagari, C.; Bedrov, D.; Smith, G. D. *Macromolecules* **2000**, *33*, 6194.
- (12) Mark, J. E. *Physical Properties of Polymers Handbook*; Springer: New York, 2007.
- (13) Hocker, H.; Blake, G. J. *P. J. Flory, Trans. Faraday Soc.* **1971**, *67*, 2251.
- (14) Zang, Y. H.; Carreau, P. J. *J. Appl. Polym. Sci.* **1991**, *42*, 1965.
- (15) Ding, Y.; Kisliuk, A.; Sokolov, A. P. *Macromolecules* **2004**, *37*, 161.
- (16) Murthy, N. S.; Wang, Z.-G.; Hsiao, B. S. *Macromolecules* **1999**, *32*, 5594.
- (17) Chen, X.; Carbone, P.; Cavalcanti, W.; Milano, G.; Müller-Plathe, F. *Macromolecules* **2007**, *40*, 8087.
- (18) Sanjeeva, N. M. *J. Polym. Sci., Part B: Polym. Phys.* **2006**, *44*, 1763.

4. Hydrogen Bonding and Dynamic Crossover in Polyamide-66: A Molecular Dynamics Simulation Study

4.1. Introduction

Nylons are some of the commercially most important engineering polymers. They are used for textiles and carpets and also, in bulk, as an engineering plastic.¹ The recent developments in nylon are based on the structure and mobility properties. Via investigation of the influence of the structure on chain mobility, it is possible to understand the correlation between structural features and polymer properties. Nylons are specified as either PA- x or PA- xy , where PA identifies nylons as a polyamide and x and y represent the number of carbon atoms between successive nitrogen atoms. Homologous series of nylons provide an opportunity to study in detail the role of hydrogen bonding in mobility, hydration, chain folding, crystallization, and deformation. Among dual-numbered nylons, PA-66 is the most important.

In polyamides, nearly all the amide groups that separate a sequence of methylene groups are hydrogen-bonded.² This large number of hydrogen bonds forms an extended three-dimensional network whose destruction influences several properties of the material such as the glass transition temperature and the melting point. For these reasons, understanding the thermal mechanical properties of polyamides by studying the thermal stability of hydrogen bonds was a popular topic in previous research.²⁻⁶ The mobility of different parts of PA-66 has been studied experimentally with nuclear magnetic resonance (NMR) methods,⁷ quasi-elastic neutron scattering,⁸ and Fourier-transform infrared (FTIR) spectroscopy.⁹ In these experiments, it has been shown that in PA-66 crystals the amide hydrogen bonds (HBs) are relatively immobile at all temperatures below 503 K (the melting point is 533 K). In particular, temperature-resolved FTIR spectroscopy is the usual methodology for investigating the status of hydrogen bonding at different temperatures. Schroeder and Cooper⁶ developed a procedure for estimating the thermodynamic parameters associated with hydrogen bond dissociation in polyamides from the total area change of the N–H stretching region induced by heat. The essential assumption is that the absorption coefficient of N–H stretching does not vary significantly with temperature. However, Skrovanek and co-workers^{10,11} found that actually the absorption coefficient of N–H stretching depends strongly on temperature and the fraction of nonbonded N–H groups, as estimated from FTIR spectroscopy, is overestimated in the experiments.

Thus, the experimental methods investigate HB dynamics only indirectly, and they can be interpreted in an only qualitative way.⁹

On the other side, molecular dynamics (MD) simulations can provide quantitative information about HB dynamics with atomistic resolution.¹²⁻¹⁵ The factors influencing the dynamics can be obtained from MD trajectories by calculating different HB time correlation functions, as proposed first by Stillinger^{16,17} and developed further by Luzar and Chandler.¹²

In this chapter, using molecular dynamics simulations, we analyze in detail the effect of temperature on the local and global dynamics of unentangled PA-66. The local dynamics are investigated mainly by looking at the HB dynamics, calculating their structure relaxation time and lifetime by means of specific correlation functions. The influence of the relaxation of the HB network on the global dynamics of the polymer is also analyzed. Moreover, the study of the structure relaxation time and the self-diffusion coefficient at different temperatures will also allow us to test the more recent theories developed to describe the physical nature of polymer glasses.^{18,19} In fact, polyamides, like other materials, when submitted to a cooling from high temperatures pass through several phase transitions, among which the most important is the glass transition. The origin (thermodynamic or kinetic) of the glass transition and the consequent structural changes occurring at the molecular level are still under investigation. Previously, theory predicted that the properties of glasses or supercooled liquids at low temperatures (far below the glass transition one) could be reliably extrapolated from the high-temperature equilibrium ones.^{20,21} In fact, it was generally accepted that most materials exhibit a non-Arrhenius behavior. For example, the diffusion coefficient and viscosity were often described with only one temperature law (the so-called Vogel–Fulcher) in the entire range of temperature. However, recent developments in the theory and new experiments have shown that as the conventional glass transition temperature (T_g) is approached the temperature dependence of the global (diffusion coefficient and viscosity) and local dynamic properties continuously changes from the typical Vogel–Fulcher–Tammann form to the Arrhenius form.^{19,22-24} The change in the temperature dependence of the dynamic properties near the conventional T_g demonstrates the poor reliability of the practice of extrapolating high-temperature properties to low temperatures. Therefore, it is of interest to investigate the problem of the temperature dependence of the dynamic properties using a computational approach. Our simulation results can indeed provide an interesting insight into the temperature dependence of the local and global dynamics and their interdependence in supercooled PA-66. We will compare our results with the most recent glass theories and with experiments conducted with several polymeric systems.

4.2. Model and Simulation Details

Twenty-four chains of PA-66 each composed of 20 chemical repeat units, containing 40 amide groups and terminated by ethyl and butyl groups (Figure 4.1), were investigated by means of molecular dynamics (MD) simulations at different temperatures. Each chain had a molecular weight of around 4540 g/mol, which is just below the experimental entanglement molecular weight (4700 g/mol).²⁵ The atomistic force field and the initial coordinates of PA-66 were taken from Goudeau et al.;²⁶ all details concerning the simulations can be found therein. Here, we summarize only the main parameters which define the MD simulations. Temperature and pressure were controlled using the weak coupling scheme introduced by Berendsen²⁷ (with $\tau_T = 0.2$ ps, $\tau_P = 5$ ps, and an isothermal compressibility of 10^{-6} kPa⁻¹). All simulations were performed at atmospheric pressure. The equation of motion was integrated with a time step of 2 fs. A Verlet neighbor list with a pair cutoff of 1.0 nm was used and updated by a link-cell scheme every 30 steps. Bond constraints were maintained to a relative tolerance of 10^{-6} by the SHAKE procedure.^{28,29} All calculations were performed with YASP.³⁰

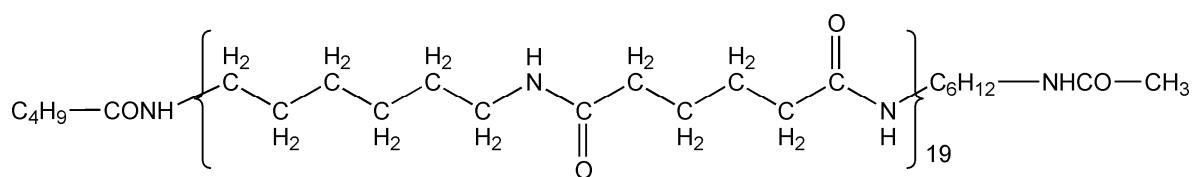


Figure 4.1. Structure of the polyamide chains employed in simulations.

The system was studied at 11 different temperatures (from 300 to 500 K in increments of 25 K and from 500 to 600 K in increments of 50 K) ranging from below to well above the experimental glass transition temperature (350 K).³¹ The system was equilibrated for more than 60 ns at low temperatures (<400 K) and for ~40 ns at high temperatures (>400 K). To determine how the system relaxes at different temperatures, we calculated the orientation time-autocorrelation function (OACF) $\langle \mathbf{u}(t) \cdot \mathbf{u}(0) \rangle$ for unit vectors \mathbf{u} along the C–O and N–H bonds of the amide groups. Figure 4.2 shows the OACF calculated for the amide groups (C–O and N–H bond vectors) at four temperatures. The figure shows that the bond vectors decorrelate fast at high temperatures while they do not decay in the long time in the glassy phase (300 K). To determine if we had achieved a satisfactory relaxed configuration also at low temperatures, we split the simulation box into eight cells (by dividing the box size by two in every direction) and calculated the density in each cell during the simulations. Figure 4.3 shows the variation in density for three cells (cells with the highest, lowest, and the most typical density) versus time. We still found a fluctuation in the density of up to 2% in different cells after 60 ns, because of the small

size of the cells, but the average density (1.1 g/cm^3) in different parts of the simulation box was the same as the experimental value at room temperature ($1.07\text{--}1.1 \text{ g/cm}^3$).³² Our system was, thus, homogeneous. This homogeneity even at a low temperature (300 K) meant that our system was globally well equilibrated.

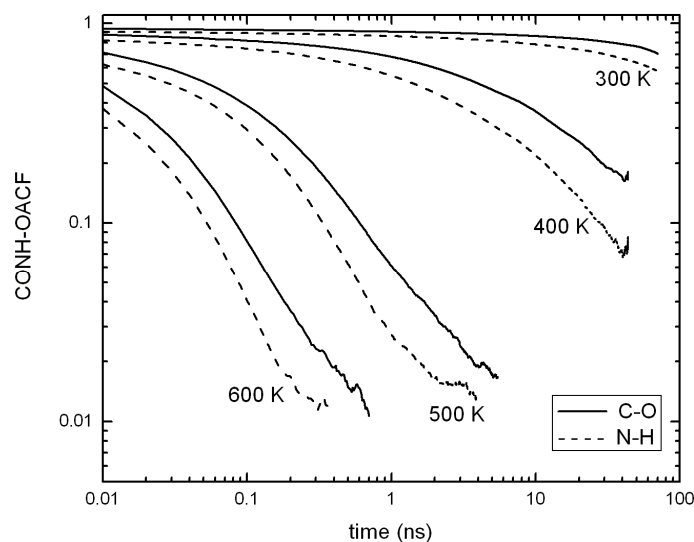


Figure 4.2. Orientation autocorrelation function for amide groups (C–O and N–H bond vectors) at 300, 400, 500, and 600 K. Solid lines represent the autocorrelation function for C–O bond vectors, and dashed lines correspond to the autocorrelation function for N–H bond vectors at every temperature.

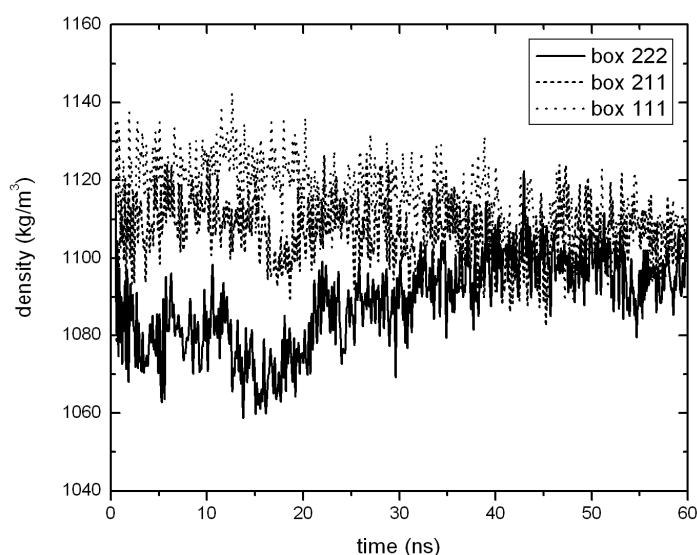


Figure 4.3. Density variations for subcells with the highest (dotted line), lowest (solid line), and most typical (dashed line) density vs time. The numbers for every cell (222, 211, and 111) correspond to the position of the subcell in the complete simulation box.

4.3. Results and Discussion

4.3.1. Static Properties of Hydrogen Bonds

The amide–amide hydrogen bond (HB) interactions were analyzed at 11 different temperatures between 300 and 600 K. The amide N–H group was considered the donor and the amide oxygen the acceptor. The main structural property distinguishing the HBs from the van der Waals interaction is their preference for linearity. To consider the angular preference of HBs, we plotted the N–H \cdots O bond angle (θ) against the H \cdots O distance (d) at 300 K (Figure 4.4). The plot contains all contacts found in the system with $d < 0.4$ nm regardless of the angle. There are densely populated clusters of data points at short distances and almost linear angles. The shortest distances occur at relatively linear angles (with θ between 150° and 180°), whereas longer bonds are observed with a larger angular range (with θ between 60° and 150°). The plot is unpopulated for distances of < 0.175 nm, because exchange repulsion prevents shorter distances. In Figure 4.4, a line limiting the configurations not populated is drawn; it represents the extreme limit of HB bending, which can be considered as an effect of the repulsions between atoms of the amide groups included in the HB.³³

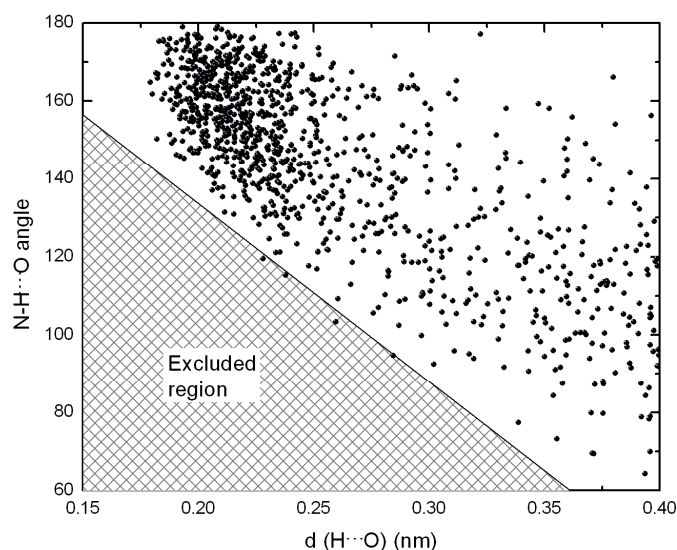


Figure 4.4. Amide–amide hydrogen bonds. Correlation of the N–H \cdots O bond angle and the H \cdots O distance at 300 K.

To study the effect of temperature on the HB length, we plotted the distribution of the H \cdots O distance d for $\theta_{\text{N-H}\cdots\text{O}} > 130^\circ$ (Figure 4.5). The distribution of the H \cdots O distance for linear HBs ($\theta_{\text{N-H}\cdots\text{O}} > 130^\circ$) has a distinct maximum around 0.218 nm at different temperatures. With an increase in temperature, the maximum peak of the distribution of the H \cdots O distance shifts linearly to distances of

>0.212 and >0.224 nm for 300 and 600 K, respectively (inset of Figure 4.5), showing a weakening of the interaction between the hydrogen and the oxygen with an increase in temperature. For high temperatures, the distribution does not fall to zero at long distances but fades into the continuum of random contacts. With an increase in temperature, the distribution of a short H...O distance (around 0.218 nm) decreases and the probability of random contacts at longer distances increases (Figure 4.5).

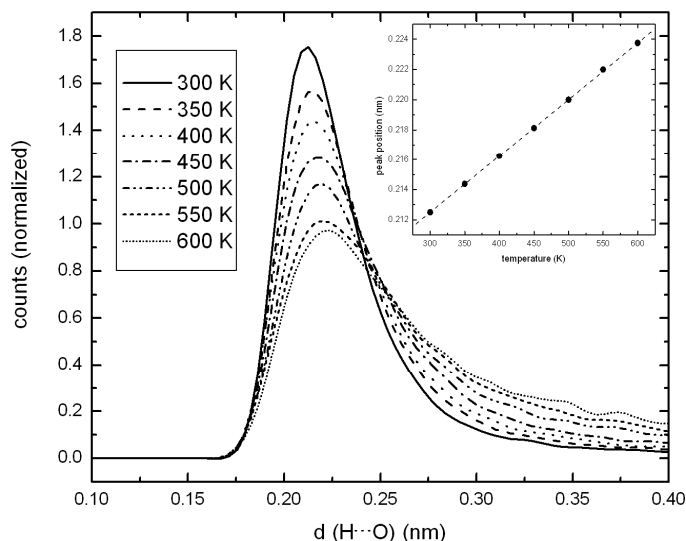


Figure 4.5. Distribution of the H...O distances for fairly linear hydrogen bonds with $\theta_{\text{N-H}\cdots\text{O}} > 130^\circ$. This histogram contains data from a horizontal slice ($180^\circ > \theta > 130^\circ$) of Figure 4.4 at different temperatures. The inset shows the temperature dependence of the peak maximum. The dashed line is the linear fit through the points.

Generally, either a geometric³⁴ or an energetic¹⁴ criterion is used to define a HB. On the basis of the results in the previous paragraph, in this work the HBs were defined according to a geometric criterion. The distance between the hydrogen of the donor group and the acceptor O has to be $<0.297 \text{ nm}^3$ and the donor–hydrogen–acceptor angle $>130^\circ$.²⁶

To calculate the enthalpy (ΔH) of HB breaking, we adopted the model proposed by Schroeder and Cooper⁶ which relates ΔH to the bonded amide fraction (X_b). The equilibrium between the hydrogen-bonded and nonbonded amides can be represented by



with an associated equilibrium constant K given by

$$K = \frac{[\text{NH}]_{\text{free}}[\text{O}=\text{C}]_{\text{free}}}{[\text{NH}\cdots\text{O}=\text{C}]_{\text{bonded}}} \quad (4-2)$$

The equilibrium constant K is related to the bonded amide fraction (X_b), to the enthalpy (ΔH), and to the entropy (ΔS) of HB breaking according to the following equation:⁶

$$\ln K = \ln\left(\frac{(1 - X_b)^2}{X_b}\right) = -\frac{\Delta H}{R} \frac{1}{T} + \frac{\Delta S}{R} \quad (4-3)$$

where R is the gas constant. Experimentally, it has been found that the average strength of the amide hydrogen bonds in an amorphous polyamide decreases with an increase in temperature because of thermal expansion.¹⁰ Thus, the number of HBs decreases with an increase in temperature. In agreement with the experimental results,^{3,6} X_b decreases with an increase in temperature and changes from 0.81 at 300 K to 0.42 at 600 K.

A van't Hoff plot is built using X_b at different temperatures and eq 4.3 (Figure 4.6). The circles in Figure 4.6 show the experimental value for the semicrystalline PA-66.³ The enthalpy ΔH of HB breaking can be obtained from the slope $-\Delta H/R$ of a linear fitting through the simulated points. Our values for the enthalpy and entropy of HB breaking in PA-66 are equal to $15.4 \pm 0.6 \text{ kJ mol}^{-1}$ and $21.7 \pm 1.2 \text{ kJ K}^{-1} \text{ mol}^{-1}$, respectively. ΔH is slightly lower than the values previously reported in the literature for a number of polyamides, which range from 29 to $\sim 59 \text{ kJ mol}^{-1}$ ^{3,5,6,35} (while ΔH for low-molecular weight amides ranges from 14.5 to 27 kJ mol^{-1}).³⁶ The dependence of ΔH on the HB criterion has been checked in our simulations, and we found similar values for ΔH at the different maximum values for H \cdots O distances (0.25, 0.35, and 0.4 nm) and the minimum values for $\theta_{\text{N-H}\cdots\text{O}}$ (90° and 150°). The discrepancy of ΔH with the experimental values is possibly related to the problem of interpreting the infrared spectral features observed in the N–H stretching region. As mentioned in the Introduction, the thermodynamic parameters associated with the HB dissociation obtained by infrared spectroscopy data can be strongly affected by errors. The usual practice of not taking into account the strong dependence of the absorption coefficient on the HB strength has indeed led to an overestimation of the fraction of free N–H groups and, in turn, to an overestimation of the enthalpy of HB breaking.¹⁰ To this erroneous practice Skrovanek and co-workers¹⁰ also ascribed the large discrepancy found between their experimental values of ΔH compared to those of their low-molecular weight analogues. However, the effect of the lower molecular weight of our model compared to the experimental one cannot be ruled out completely, and the presence of entanglements (as likely occur in the experimental samples) could increase the value of ΔH .

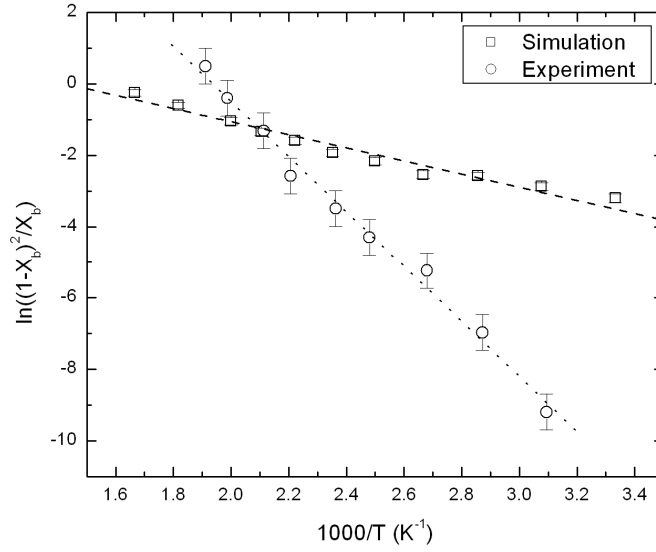


Figure 4.6. van't Hoff plot of the hydrogen bond dissociation equilibrium in the simulation and the experiment.³ The dashed and dotted lines are linear fits through the simulation and the experiment points, respectively.

4.3.2. Dynamic Properties of Hydrogen Bonds

The dynamics of HBs in the bulk of PA-66 was investigated by calculating the structure relaxation time, the rate constant of HB breaking, and the average HB lifetime. We calculated these dynamical properties for HBs between amide groups in terms of two time correlation functions (TCFs), namely, the continuous HB time correlation function, $S(t)$, and the intermittent HB time correlation function, $C(t)$.^{16,17,37} These TCFs are defined as

$$S(t) = \frac{\langle \delta h(0) \delta H(t) \rangle}{\langle \delta h(0) \delta H(0) \rangle} = \frac{\langle h(0)H(t) \rangle - \langle h \rangle \langle H \rangle}{\langle h \rangle - \langle h \rangle \langle H \rangle} \approx \frac{\langle h(0)H(t) \rangle}{\langle h \rangle} \quad (4-4)$$

and

$$C(t) = \frac{\langle \delta h(0) \delta h(t) \rangle}{\langle \delta h^2 \rangle} = \frac{\langle h(0)h(t) \rangle - \langle h \rangle^2}{\langle h \rangle - \langle h \rangle^2} \approx \frac{\langle h(0)h(t) \rangle}{\langle h \rangle} \quad (4-5)$$

where the population variable $h(t)$ is unity when a particular hydrogen–oxygen pair is hydrogen bonded at time t , according to the definition, and zero otherwise. On the other hand, $H(t) = 1$ if the tagged O–H bond remains continuously hydrogen bonded during time duration t and zero otherwise. The brackets denote an average over all amide pairs and all starting times. The average number of HBs (N_{HB}) in a system of N amide groups is equal to the number of all pairs multiplied by the average value

of the HB population operator ($\langle h \rangle$) [$N_{HB} = \frac{1}{2}N(N-1)\langle h \rangle$]. If N_{HB} (in a system containing N amide groups) has the same order of magnitude as N , then the approximations in eqs 4.4 and 4.5 follow because $\langle h \rangle \propto 1/N \approx 0$ when the number of amide groups is large.³⁸

According to the definition, $C(t)$ describes the probability that a particular tagged HB is intact at time t , given it was intact at time zero, while $S(t)$ provides a definition of the lifetime of a tagged HB. The relaxation time of $C(t)$ is usually called the structural relaxation time (τ_R) of HBs, and the relaxation time of $S(t)$ describes the average HB lifetime (τ_{HB}). The long time behavior of $S(t)$ (which depends on the continuous presence of a HB) is strongly affected by short time fluctuations due to librational motion of the molecules and by the criterion for defining the HB. However, such fluctuations do not strongly affect the long time behavior of $C(t)$ (which does not depend on the continuous presence of a HB but allows for intermittent HBs). Thus, $S(t)$ is sensitive to the sampling frequency, and choosing a long time interval between sampled configurations corresponds to ignoring processes where a bond is broken for a short time and subsequently re-forms. To calculate $S(t)$ in our simulations, we sampled the configurations every 10 fs (shorter than the typical libration time, which could destroy a bond),¹⁴ while $C(t)$ was obtained with time resolution of 10 ps.

Figure 4.7a shows the time correlation function $C(t)$ at different temperatures. At very short times, $C(t)$ decays rapidly due to librational motion. After the initial rapid decay, it remains relatively constant, especially at low temperatures: for temperatures below 400 K, the correlation function does not relax within the 20 ns, while for temperatures above 400 K, $C(t)$ decays very fast to zero. At all temperatures, $C(t)$ shows the presence of slow components at long times. Such slow long time decay cannot be described by a single-exponential function or by a stretched-exponential function.¹³ To determine the relaxation times (τ_R), we fit the decay curves (Figure 4.7a) to three exponentials and extrapolated. The parameters for best fits along with the amplitude-weighted average τ_R for four temperatures are listed in Table 4.1. As we can see in Table 4.1, we have an abrupt increase in the structural relaxation time as the glass transition temperature T_g (330 K) as calculated from our atomistic model²⁶ approaches.

To analyze the behavior of τ_R in PA-66 at different temperatures, we plotted the structural relaxation time in $\log(\tau_R)$ versus $1000/T$ in Figure 4.7b. At $T \geq 413$ K, τ_R can be fit well by the Vogel–Fulcher–Tammann (VFT) equation, $\tau_R \propto e^{A T_0 / (T - T_0)}$, where $A = 3.36$ and $T_0 = 298.88$ K. The VFT fit deviates visibly from the data at $T \leq 413$ K, where one can see a sudden change in the slope of the $1/T$ dependence of $\log(\tau_R)$. The relaxation time τ_R at low temperatures can be fitted by the Arrhenius equation ($\tau_R \propto e^{E_A / k_B T}$, with an activation energy E_A of 22.81 kJ mol⁻¹). Thus, with a

decrease in temperature, the dependence of τ_R on temperature becomes weaker and shows a crossover between two different regimes at approximately $T_c = 413$ K (T_c is the crossover temperature between the VFT and Arrhenius fits). The presence of this crossover will be explained further below.

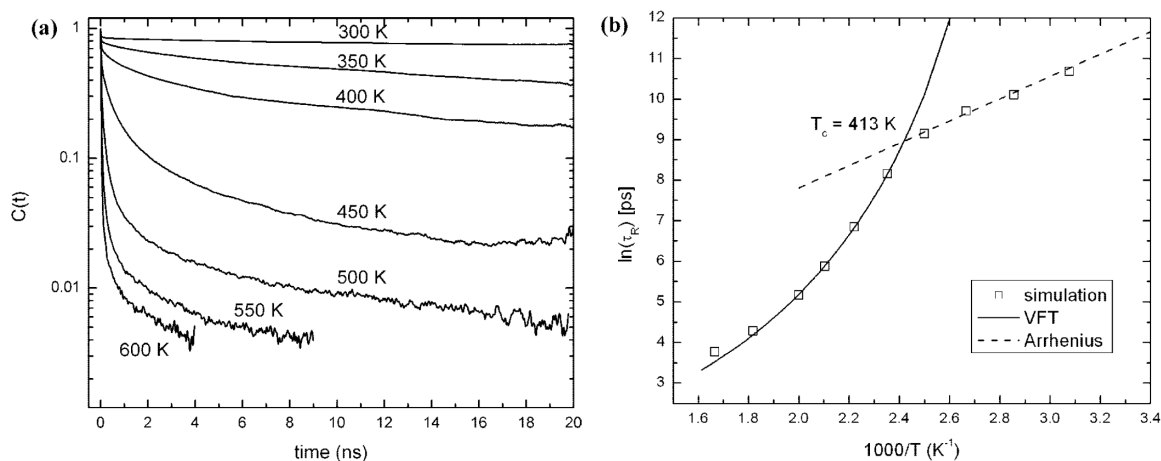


Figure 4.7. (a) Semilog plot of the structural time correlation function $C(t)$ for amide–amide hydrogen bonds at different temperatures. (b) Temperature dependence of structure relaxation time plotted for temperatures ranging between 300 and 600 K. The dashed line denotes a fit to an Arrhenius law at $T < 413$ K and the solid line a fit to a Vogel–Fulcher–Tammann (VFT) law at $T \geq 413$ K. Error bars are smaller than the symbols.

Table 4.1. Multiexponential Fitting Parameters for the Oxygen–Hydrogen Intermittent [$C(t)$] and Continuous [$S(t)$] Hydrogen Bond Time Correlation Functions at 300, 400, 500, and 600 K.

$C(t)$				$S(t)$		
temperature (K)	time constant (ps)	amplitude (%)	τ_R (ps)	time constant (ps)	amplitude (%)	τ_{HB} (ps)
300	201188.0	81.7	164550.0	2.5	37.4	1.2
	58.5	14.9		0.5	44.7	
	2453.7	3.2		0.1	16.9	
400	23449.3	37.7	9302.9	0.9	24.9	0.4
	11.2	31.9		0.3	52.4	
	1594.2	29.0		0.1	22.3	
500	2031.5	6.3	174.7	0.3	58.6	0.2
	5.4	57.6		0.1	20.6	
	118.3	36.0		0.1	20.9	
600	1834.0	1.7	43.1	0.3	14.3	0.1
	4.3	81.1		0.2	54.8	
	45.4	17.1		0.1	31.0	

As mentioned in the Introduction, different kinds of glass-forming liquids can be classified according to the dependence of their transport properties (TPs), i.e., viscosity and self-diffusion coefficient, on temperature. The TPs in strong glass formers follow an Arrhenius type equation (TP = $Be^{A/T}$, with B and A being fitting parameters), while in the fragile glasses, they are described by the Vogel–Fulcher–Tammann (VFT) equation [TP = $Be^{AT_0/(T-T_0)}$, with B , A , and T_0 as fitting parameters]. Recent improvements in the mode-coupling theory (MCT) of the glass transition^{39,40} predict the existence of a crossover of the dynamics at the molecular level, at some critical temperature, T_c , above T_g . Experiments and numerical theories have investigated several low-molecular weight and polymeric systems⁴¹ to test the MCT predictions, and it has been found that the empirical equations such as the Arrhenius or VFT equation alone are not able to fit several types of TPs over a large range of temperatures; in particular, it has been found that the TPs show a crossover from VFT to Arrhenius behavior around T_c . Indeed, many dynamic properties of glass-forming liquids, such as the α and β relaxation processes,⁴² the rotational and translational diffusion coefficients,⁴³ and the dielectric relaxation strength,⁴⁴ show qualitative changes at a temperature around T_c . Thus, there is much evidence that some qualitative changes occur in the dynamics of glass-forming systems in a small temperature range above T_g . It has also been noted in refs⁴⁵ and ⁴⁶ that the ratio T_c/T_g correlates with the fragility of glass-forming systems: the higher the fragility, the lower value of T_c/T_g .

Since the presence of HB affects strongly the transport properties of materials,^{12,47-49} we investigated the trend of the chain self-diffusion coefficient D [$6D = \lim_{t \rightarrow \infty} \frac{d}{dt} \langle |R(t) - R(0)|^2 \rangle$] with temperature to find a possible relation among the behavior of τ_R and TP. Figure 4.8 reports D calculated only in the rubber phase ($T \geq 350$ K) considering the T_g found in our simulations (330 K).²⁶ At 414 K, a transition from a VFT to an Arrhenius behavior is visible. This temperature agrees with the one calculated from the τ_R (413 K), and it corresponds to the experiment “softening temperature” (the temperature above which the system changes from viscous flow to plastic flow) reported for PA-66 which lies at 413 K.⁵⁰ Moreover, the ratio T_c/T_g in our system (≈ 1.25) is in the same range as experimental values found for polybutadiene (≈ 1.20),⁵¹ polyisobutylene (≈ 1.35),²² and polystyrene (≈ 1.14).²² The presence of a crossover temperature in our simulations is also in agreement with the recent theoretical work of Baeurle and co-workers¹⁸ on the glassy state of polymer materials. Their physical interpretation of the crossover temperature can be summarized as follows. If the system is cooled very slowly to a temperature slightly above T_g (i.e., T_c), the glass-forming polymer becomes trapped in a quasi-equilibrium state by undergoing a percolation transition of high-density clusters which leads to variations in the local monomer density and mobility. The formation of a continuous backbone between the high-density clusters restricts the polymer mobility below T_c , causing a sudden

increase in viscosity. Developed starting from observations made on the stress relaxation experiments conducted with styrenic block copolymers,⁵² this model is able to describe correctly their mechanical response.¹⁸ In the case of our simulations, it is possible that the hydrogen-bonded amide groups (randomly distributed or organized in clusters) whose number increases, decreasing the simulation temperature, form at the crossover temperature a continuous backbone causing the deceleration of the structural relaxation time (Figure 4.7a) and of the self-diffusion coefficient (see Figure 4.8). Further investigations into the spatial organization of the HBs and their percolation within the model could confirm this picture.

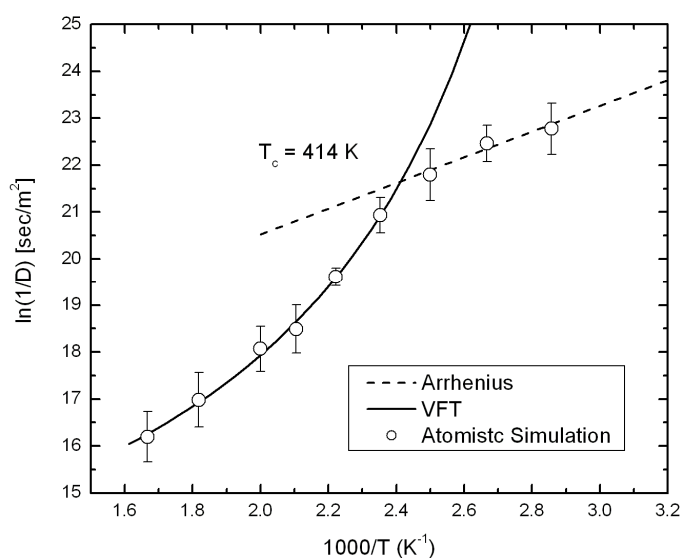


Figure 4.8. Temperature dependence of the chain self-diffusion coefficient plotted for temperatures above T_g (330 K). The dashed line denotes a fit to an Arrhenius law when $T < 414$ K and the solid line a fit to a Vogel–Fulcher–Tammann (VFT) law when $T \geq 414$ K.

To compare the variation of the diffusion coefficient and structure relaxation time with temperature, we normalized $1/D$ and τ_R by their respective values at 600 K. This normalization was done by shifting the curves in Figures 7b and 8 to their corresponding values at 0.00167 K^{-1} (Figure 4.9). We observe that there is a collapse of the two curves; thus, we conclude that both dynamic properties exhibit the same behavior at different temperatures. In Figure 4.9, we also include the correlation times from the orientational correlation functions (τ_{OACF}) of C=O and N–H bonds which are shown in Figure 4.2. τ_{OACF} values are calculated in a same way as τ_R by fitting the orientational correlation functions (Figure 4.2) with three exponential functions. The normalization of the correlation times by the corresponding values at 600 K (Figure 4.9) shows that different dynamic properties of the system ($1/D$, τ_R , and τ_{OACF}) are coupled and follow the same behavior with temperature.

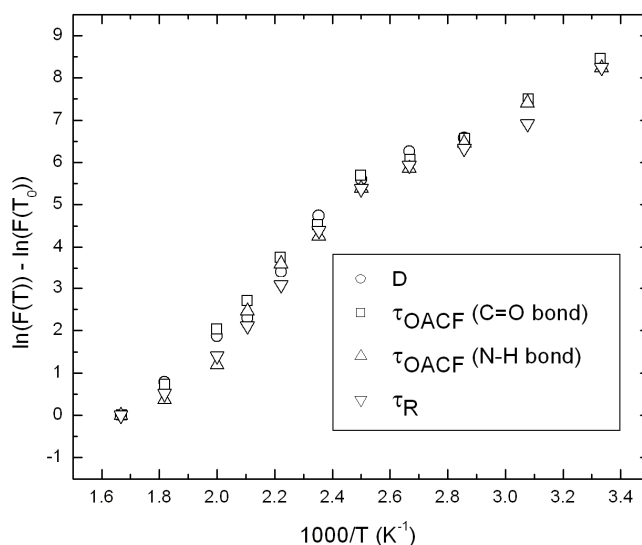


Figure 4.9. Normalization of the curves in Figures 7b and 8 and the time correlations from the orientational correlation function of C=O and N–H bonds by the corresponding values at 600 K (T_0). The function $F(T)$ corresponds to $1/D$, τ_R , and τ_{OACF} for C=O and N–H bonds.

The rate of relaxation to equilibrium is characterized by the reactive flux HB correlation function, $k(t)$

$$k(t) = -\frac{dC(t)}{dt} \quad (4-6)$$

where $-k(t)$ is the rate of change of the HB population at time t . To study the variation of $k(t)$ at short times, we calculated the derivative of the intermittent HB correlation function $C(t)$ (eq 4.5) obtained with a time resolution of 1 ps (Figure 4.10). The $k(t)$ values determined from our simulation at four temperatures are shown in Figure 4.10. At short times, $k(t)$ quickly changes from its initial value. The angular restriction of the HB definition makes it very sensitive to librational motion, which has a characteristic time of <0.1 ps. To gain a better view of the relaxation for a time scale of <1 ps, we used $C(t)$ with a time resolution of 10 fs (inset of Figure 4.10). At this time scale, the system undergoes several transitions from forming the HB to breaking the HB and the reactive flux shows a dip at $t \approx 0.07$ ps (see the inset of Figure 4.10). Thus, the dip is created by the pairs initially hydrogen bonded which are broken (by libration) but often re-form a HB. Beyond this transient period, $k(t)$ decays monotonically, and for times of >2 ps, it will not change much with time at different temperatures. As shown in Figure 4.10, the reactive flux function, $k(t)$, has a larger value for higher temperatures until 20 ps; however, there is a big difference between the $k(t)$ at 300 and 400 K, while the $k(t)$ has almost same value at long times for 500 and 600 K. These results show that temperature affects the rate of relaxation to equilibrium more at low temperatures than at high temperatures.

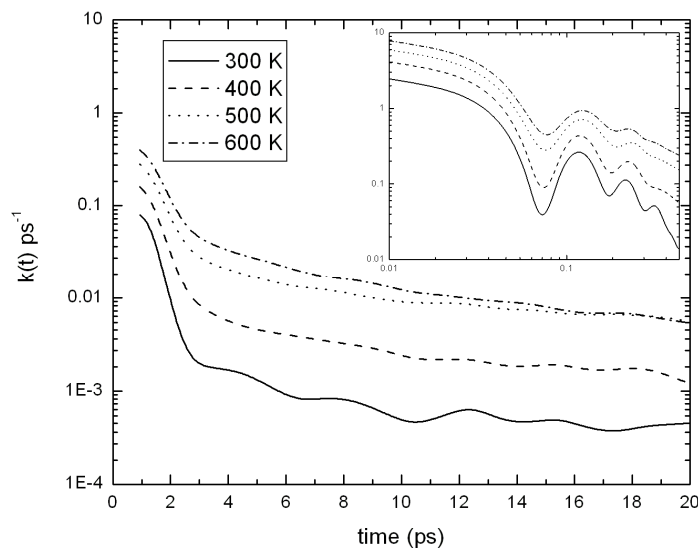


Figure 4.10. Reactive flux HB correlation function $k(t)$ at 300, 400, 500, and 600 K extracted from the atomistic simulations. The inset panel shows a log–log plot of the same function at short times.

The dynamics of HBs between amide groups is strongly coupled to the diffusion of the molecules. Faster diffusion will result in faster HB relaxation and vice versa.¹² After a HB is broken, the amide groups can remain in the vicinity for some time before the bond is reformed or they diffuse away from each other. To study the effect of diffusion on the dynamics of HBs at different temperatures, we calculated the time correlation function^{48,53}

$$M(t) = \frac{\langle h(0)(1-h(t))H'(t) \rangle}{\langle h \rangle} \quad (4-7)$$

where $H'(t)$ is unity if the tagged pairs of hydrogen and oxygen are closer than 0.297 nm at time t and zero otherwise. In Figure 4.11, the relaxation of $M(t)$ at different temperatures is shown. As discussed before, we have a fragile-to-strong transition in the transport properties of the system at $T_c = 413$ K. This crossover can also be identified in the relaxation of $M(t)$. The figure shows that $M(t)$ is almost constant below 400 K, while it relaxes fast above 400 K. A low diffusion coefficient at temperatures below 400 K causes low mobility of the amide groups that remain in the vicinity of each other after the break of the HB, increasing the probability of re-forming it. Thus, $C(t)$ and $M(t)$ decay very slowly for low temperatures, while at high temperatures (above 400 K), they decay very fast since after the HB rupture the amide groups can diffuse easily away from each other.

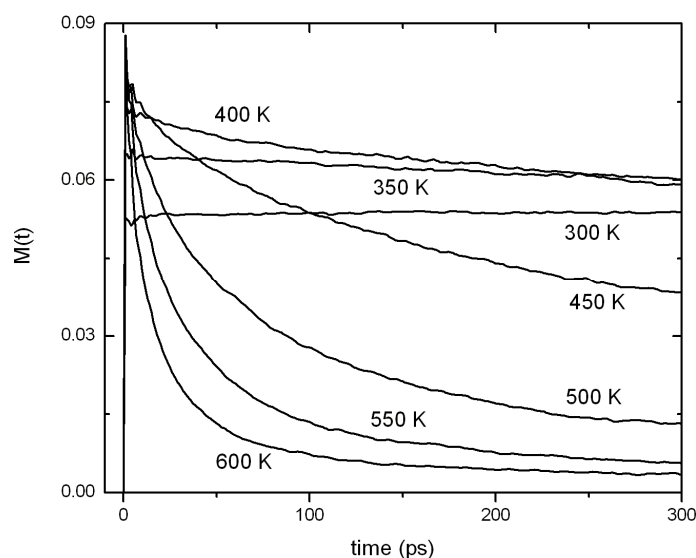


Figure 4.11. Time dependence probability that amide–amide HBs are broken, but they remain in the vicinity of each other.

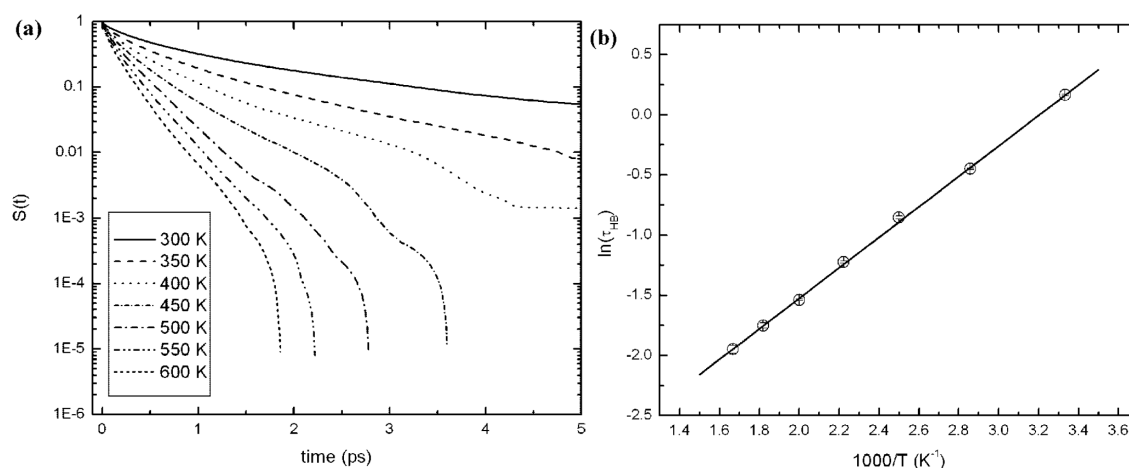


Figure 4.12. (a) Semilog plot of the time correlation function $S(t)$ for HB between oxygen and hydrogen of the amide groups at different temperatures. (b) Hydrogen bond lifetimes (τ_{HB}) obtained from $S(t)$. The line is a fit to the Arrhenius law.

In Figure 4.12a, we show the relaxation of the continuous HB time correlation function, $S(t)$, at different temperatures. As we find for intermittent HB the time correlation function [$C(t)$], $S(t)$ decays very fast at short times due to librational motion, but the correlation functions at different temperatures do not show a long time relaxation compared to $C(t)$. $S(t)$, like $C(t)$, can be fitted to a sum of three exponentials. The fitting parameters and the amplitude-weighted average HB lifetimes (τ_{HB}) for four temperatures are given in Table 4.1. The HB lifetime decreases with an increase in temperature, from 1.18 to 0.14 ps from 300 to 600 K. In Figure 4.12b, we display the variation of τ_{HB} in a semilog plot versus $1000/T$. The figure shows that the mean HB lifetimes obtained from $S(t)$ follows an Arrhenius behavior at different temperatures ($\tau_{\text{HB}} \propto e^{E_A/k_B T}$) with an activation energy of $10.5 \pm 0.5 \text{ kJ mol}^{-1}$. The

activation energy associated with the hydrogen bond lifetime is interpreted as the energy required to break a HB via librational motion, a fast motion.⁵⁴ The Arrhenius behavior of τ_{HB} is in agreement with experimental results conducted with liquid water in different environments.^{14,17,38,54-56}

4.4 Conclusions

We have analyzed the hydrogen bond dynamics in bulk polyamide-66 by means of molecular dynamics simulations. Our geometrical definition of the HB has led to a hydrogen bond enthalpy ΔH value that is in agreement with experimental data, especially with those measured for low-molecular weight amides. Following the time relaxation of several correlation functions, we have found that the global dynamics of unentangled polyamide-66 is governed by the relaxation of the hydrogen bond network formed among the amide groups. By looking at the behavior of the self-diffusion coefficient and the structural relaxation times, we identified a transition temperature (T_c) at ~ 413 K, and it corresponds to the experiment softening temperature reported for polyamide-66 which is 413 K.⁵⁰ Approaching T_c from above, the temperature dependence of these two dynamic variables changes continuously from VFT to Arrhenius behavior. Our simulation results confirm the most recent theoretical works^{18,19} predicting an Arrhenius behavior of the diffusion coefficient in supercooled polymers and, in the case of polyamide-66, relate unequivocally the relaxation of the hydrogen bonds with the global dynamics of the polymer. According to the most recent glass theory,^{18,19} the crossover temperature found in our simulations can be seen as the temperature at which the polymer melt is subjected to spatiotemporal fluctuations that lead to variations in the local mobility governed by the relaxation of the HBs. Our results have also confirmed that this transition temperature does not coincide with the glass transition one, but their ratio falls into the typical values found experimentally for other polymeric systems.

It must be noticed that in contrast, the hydrogen bond lifetimes (time to first rupture) governed by the local librational dynamics of the amide groups show an Arrhenius behavior over the whole temperature range. In summary, we have shown that for unentangled polyamide-66 the continuous change in the temperature dependence of the diffusion coefficient from the VFT to Arrhenius form corresponds, at the molecular level, to a change in the hydrogen bond dynamics. This result shows that for polyamides the extrapolation of high-temperature properties to low temperatures is not reliable. The interpretation at the molecular level of the crossover transition found for PA-66 can help in understanding the physical aging process for other polymeric materials characterized by an extensive hydrogen bond network.

4.5. References

- (1) Kohan, M. I. *Nylon Plastics Handbook*; Hanser Gardener: Cincinnati, 1995.
- (2) Murthy, N. S. *J. Polym. Sci. B: Poly. Phys.* **2006**, *44*, 1763.
- (3) Garcia, D.; Starkweather, H. W. *J. Polym. Sci. Polym. Phys. Edi.* **1985**, *23*, 537.
- (4) Bessler, E.; Bier, G. *Makromol. Chem.* **1969**, *122*, 30.
- (5) Trifan, D. S.; Terenzi, J. F. *J. Polym. Sci.* **1958**, *28*, 443.
- (6) Schroeder, L. R.; Cooper, S. L. *J. Appl. Phys.* **1976**, *47*, 4310.
- (7) Slichter, W. P. *J. Polym. Sci.* **1958**, *35*, 77.
- (8) Xenopoulos, A.; Wunderlich, B.; Narten, A. H. *Macromolecules* **1993**, *26*, 1576.
- (9) Lu, Y.; Zhang, G.; Feng, M.; Zhang, Y.; Yang, M.; Shen, D. *J. Polym. Sci. B* **2003**, *41*, 2313.
- (10) Skrovanek, D. J.; Howe, S. E.; Painter, P. C.; Coleman, M. M. *Macromolecules* **1985**, *18*, 1676.
- (11) Skrovanek, D. J.; Painter, P. C.; Coleman, M. M. *Macromolecules* **1986**, *19*, 699.
- (12) Luzar, A.; Chandler, D. *Phys. Rev. Lett.* **1996**, *76*, 928.
- (13) Chanda, J.; Chakraborty, S.; Bandyopadhyay, S. *J. Phys. Chem. B* **2006**, *110*, 3791.
- (14) Starr, F. W.; Nielsen, J. K.; Stanley, H. E. *Phys. Rev. Lett.* **1999**, *82*, 2294.
- (15) Tamai, Y.; Tanaka, H. *Macromolecules* **1996**, *29*, 6761.
- (16) Stillinger, F. H. *Adv. Chem. Phys.* **1975**, *31*, 1.
- (17) Stillinger, F. H. *Science* **1980**, *209*, 451.
- (18) Baeurle, S. A.; Hotta, A.; Gusev, A. A. *Polymer* **2006**, *47*, 6243.
- (19) DiMarzio, E. A.; Yang, A. J. M. *J. Res. Natl. Inst. Stand. Technol.* **1997**, *102*, 135.
- (20) Gibbs, J. H. *J. Chem. Phys.* **1956**, *25*, 185.
- (21) Adam, G.; Gibbs, J. H. *J. Chem. Phys.* **1965**, *42*, 139.
- (22) Kisliuk, A.; Mathers, R. T.; Sokolov, A. *J. Polym. Sci., Part B: Polym. Phys.* **2000**, *38*, 2785.
- (23) O'Connell, P. A.; McKenna, G. B. *J. Chem. Phys.* **1999**, *110*, 11054.
- (24) Gerardin, J.; Mohanty, S.; Mohanty, U. *J. Chem. Phys.* **2003**, *119*, 4473.
- (25) Zang, Y.-H.; Carreau, P. J. *J. Appl. Phys. Sci* **1991**, *42*, 1965.
- (26) Goudeau, S.; Charlot, M.; Vergelati, C.; Müller-Plathe, F. *Macromolecules* **2004**, *37*, 8072.
- (27) Berendsen, H. J. C.; Postma, J. P. M.; Gunsteren, W. F. v.; Nola, A.; Haak, J. R. *J. Chem. Phys.* **1984**, *81*, 3684.
- (28) Ryckaert, J.-P.; Ciccotti, G.; Berendsen, H. J. C. *J. Comput. Phys.* **1977**, *23*, 327.
- (29) Müller-Plathe, F.; Brown, D. *Comput. Phys. Commun.* **1991**, *78*, 77.
- (30) Müller-Plathe, F. *Comp. Phys. Comm* **1993**, *78*, 77.
- (31) Bradbury, E. M.; Elliot, A. *Polymer* **1963**, *4*, 47.
- (32) Viers, B. D. *In Polymer Data Handbook*; Oxford University Press: New York, 1999.
- (33) Savage, H. F. J.; Finney, J. L. *Nature* **1986**, *322*, 717.
- (34) Lopez, C. F.; Nielsen, S. O.; Klien, M. L.; Moore, P. B. *J. Phys. Chem. B* **2004**, *108*, 6603.
- (35) Hobza, P.; Mulder, F.; Sandorfy, C. *J. Am. Chem. Soc.* **1982**, *104*, 925.
- (36) Pimentel, G. C.; McClellan, A. L. *The Hydrogen Bond*; W. H. Freeman and Co.: San Francisco, 1960.
- (37) Rapaport, D. C. *Mol. Phys.* **1983**, *50*, 1151.
- (38) Luzar, A. *Chem. Phys.* **2000**, *258*, 267.
- (39) Götze, W.; Sjögren, L. *Rep. Prog. Phys.* **1992**, *55*, 241.
- (40) Götze, W. *J. Phys.: Condens. Matter* **1999**, *11*, A1.
- (41) Novikov, V. N.; Sokolov, A. P. *Phys. Rev. E.* **2003**, *67*, 031507.

-
- (42) Döß, A.; Paluch, M.; Sillescu, H.; Hinze, G. *Phys. Rev. Lett.* **2002**, *88*, 095701.
- (43) Rössler, E. *Phys. Rev. Lett.* **1990**, *65*, 1595.
- (44) Schönhals, A. *Europhys. Lett.* **2001**, *56*, 815.
- (45) Rössler, E.; Sokolov, A. P.; A. Kisluk; Quitmann, D. *Phys. Rev. B* **1994**, *49*, 14967.
- (46) Sokolov, P.; Kisluk, A.; Quitmann, D.; A. Kudlik; Rössler, E. *J. Non-Cryst. Solids* **1994**, *138*, 172.
- (47) Luzar, A.; Chandler, D. *Nature* **1996**, *397*, 55.
- (48) Xu, H.; Berne, B. J. *J. Phys. Chem. B* **2001**, *105*, 11929.
- (49) Xu, H.; Stern, H. A.; Berne, B. J. *J. Phys. Chem. B* **2002**, *106*, 2622.
- (50) <http://www.lenzing.com/plastics/en/5750.jsp>.
- (51) Arbe, A.; Richter, D.; Colmenero, J.; Farago, B. *Phys. Rev. E* **1996**, *54*, 3853.
- (52) Baeurle, S. A.; Hotta, A.; Gusev, A. A. *Polymer* **2005**, *46*, 4344.
- (53) Paul, S.; Chandra, A. *Chem. Phys. Lett* **2004**, *386*, 218.
- (54) Chen, S.-H.; Teixeira, J. *Adv. Chem. Phys.* **1985**, *64*, 1.
- (55) Conde, O.; Teixeira, J. *Mol. Phys.* **1984**, *53*, 951.
- (56) Laenen, R.; Simeonidis, K.; Laubereau, A. *J. Chem. Phys* **2002**, *112*, 8487.

5. Fast Dynamics in Coarse-Grained Polymer Models: The Effect of the Hydrogen Bonds

5.1. Introduction

The hydrogen bonds (HB) is one of the intermolecular interactions that most influences the dynamics of the molecular systems, being responsible for the structure, function, and dynamics of a vast number of chemical systems from inorganic to biological compounds.¹ Due to the simplification of the coarse-grained models, the atoms directly involved in the HB (oxygen, nitrogen or fluorine as hydrogen bond acceptor) and the hydrogen (the donor atom) are usually “coarse-grained away”, i.e. lumped with other atoms in beads. Several models have been developed to describe HB especially in studying protein folding² with different success. Similar types of study have not been carried out for synthetic macromolecules although also in their case the presence of the HBs affects strongly their conformation, chemical-physical properties, crystallization self-assembly behaviour and many other global properties. It is therefore particularly interesting to see whether and how the features owed to the hydrogen bonds are preserved in the CG model of the macromolecule, in which they are only present in an effective and averaged way. In addition, the possibility of correctly describing the HB dynamics using a CG model would be of great importance for further improvements of CG force fields.

In this contribution we study a CG model of polyamide-66 (PA-66) focusing on the dynamics (and thermodynamics) of the HB. Among the common thermoplastic polymers, polyamides are noted for their outstanding properties, including high tensile strength, excellent abrasion, chemical and heat resistance and low coefficient of friction.³ The macroscopic properties of PA are strongly determined by the presence of a large three-dimensional hydrogen-bonds network connecting the amide groups, which is also responsible for different crystalline phases present in the semi-crystalline materials.⁴⁻⁷ Extensive research on hydrogen bonding in PA-66 has been performed experimentally in the past.⁸ Moreover our recent computational work on PA-66⁹ has revealed, by means of atomistic molecular dynamic simulations, interesting features of their dynamics. Therefore this polymer is the perfect candidate for our investigation.

The present chapter has three components. We first review the procedure followed to decide the mapping scheme (where to locate the CG beads and how many atoms to collect in each bead) as well as the iterative procedure (Iterative Boltzmann Inversion) used to develop the CG potential acting

among the beads. Secondly, an effective reverse-mapping strategy is presented which reinserts the atoms into a relaxed coarse-grained structure. The reinsertion of the atomic details in the CG model after long CG simulations is important to test the CG force field and the mapping scheme. The resulting atomistic structure is tested against several structural properties among them the number of hydrogen bonds. Thirdly, the ability of the CG model to describe correctly the dynamics of the hydrogen-bond network at different simulation temperatures is tested. To address this issue we use the same correlation functions which have been employed in the analysis of hydrogen bond dynamics in atomistic simulations.⁹

5.2. Coarse-Grained Model

The same mapping scheme described in chapter 3 for PA-66 has been used here. In this section we briefly describe the development of the CG force field and we provide the force field parameters (in Appendix.1).¹⁰ The initial mesoscale structure is obtained from the atomistic chains by a direct mapping. The coarse-grained model and the underlying atomistic structure are sketched in Figure 5.1. The bead labelled A represents the amide group plus the first methylene group of the tetramethylene unit, the other two methylene groups of the tetramethylene unit are lumped in one bead labelled M2, the hexamethylene unit is split into two beads containing three methylene groups each (labelled M3). The centers of the beads A, M2, M3 are located respectively in the carbonyl carbon, in the center of mass of the ethylene unit and in the central carbon atom. The coarse-grained monomer is then represented by the bead sequence: A-M2-A-M3-M3. The end groups are treated separately, since their local dynamics differ from the internal monomers, and to conserve the total mass of the system. We label the end monomer containing the amide group AP and the one containing the aliphatic moiety M3P (Figure 5.1). Both end beads contain, compared to the corresponding intra chain beads (A and M3), one extra hydrogen atom. In this mapping scheme, the atomistic system composed by 24 chains of 765 atoms each (18360 interaction sites) is turned into a coarse-grained model of 24 chains 100 beads (or superatoms) each (2400 interaction sites).

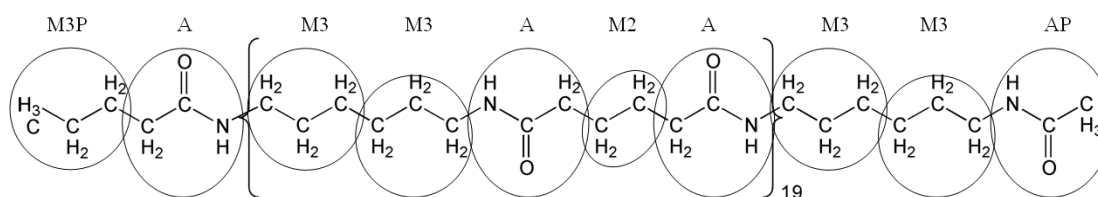


Figure 5.1. Mapping between atomistic and coarse-grained models of polyamide-66. The circles denote which atoms are joined into coarse-grained beads. The designations of the beads are indicated by the labels.

A realistic CG force field of PA-66 must reproduce the distributions for five bond types (A-M3, A-M2, M3-M3, M3P-A and AP-M3) and five angles types (A-M2-A, M3-M3-A, M3-A-M2, AP-M3-M3 and M3-A-M3P), plus all intermolecular and intramolecular radial distribution functions (RDF) between the beads as extracted from the atomistic simulations, whose details and results are reported in reference.¹¹ The CG potential presented here is obtained by the so called Iterative Boltzmann Inversion (IBI)¹² procedure that iteratively corrects the potential of mean force along a coordinate χ ($A(\chi)$ in eq 5.1, where k_B is the Boltzmann constant and T is the temperature), obtained from directly Boltzmann-inverting the distribution of this coordinate ($P(\chi)$ in eq 5.1), until the potential energy $V(\chi)$ corresponding to that interaction is obtained.¹³

$$A(\chi) = -k_B T \ln P(\chi) \quad \text{direct Boltzmann inversion} \quad (5-1)$$

To build up the bonded part of the potential, we start from bond-length and bond-angle distributions extracted from the atomistic simulations and normalized by the Jacobian between internal and Cartesian coordinates.¹⁴ Probably due to the stiffness of the bonded interactions, the direct Boltzmann inversion of the atomistic distributions (eq 5.1) gives approximate potentials, which already lead to CG distributions close to the atomistic ones, i.e. $V(\chi) \sim A(\chi)$. Nevertheless, since we need a perfect coincidence of the distributions we have found it advantageous to first fit the distributions $P(\chi)$ with a suitable sum of Gaussians, which is then Boltzmann inverted.¹⁵ Since the atomistic distributions of the M3-M3-A-M2, M3-A-M2-A and A-M3-M3-A dihedral angle distributions are almost uniform between 0° and 360° , no explicit torsional potential for beads separated by three backbone bonds is needed. The beads separated by three or more CG bonds interact through the coarse-grained nonbonded potential in the same way as any other nonbonded pair. The parameters N (number of Gaussian functions), A_i (total area), w_i (width), and m_i (central value) of the Gaussian expansions of the different $P(\chi)$

$$P(\chi) = \sum_{i=1}^N A_i (2\pi w_i^2)^{-1/2} \exp\left(-\frac{(\chi - m_i)^2}{2w_i^2}\right) \quad (5-2)$$

are given in Tables A.1.1 and A.1.2 of the Appendix.1.¹⁰

For the softer nonbonded part of the potential we use the full IBI process. The potentials obtained from the direct Boltzmann inversion of the radial distribution functions (RDFs, $P(\chi)$ of eq 5.1 is in this case one of the RDFs) are used only as initial guesses for the iteration procedure. Iterations continue until agreement of the coarse-grained RDF with the corresponding atomistic RDF is obtained (eq 5.3 where k_B is the Boltzmann constant, T is the temperature, $RDF_{\text{target}}(r)$ is the RDF

from the atomistic simulations, $RDF_j(r)$ is the RDF extracted from the CG simulations run with the CG force field $V_j(r)$ and j is the iteration count).¹³

$$V_{j+1}(r) = V_j(r) + k_B T \ln \frac{RDF_j(r)}{RDF_{\text{target}}(r)} \quad \text{Iterative Boltzmann Inversion} \quad (5-3)$$

The CG simulations are done with our molecular dynamic code IBIsCO.¹⁶ They are performed at constant temperature (400 K) and density (the same as the corresponding atomistic one, 1064 kg/m³) for 3.5 ns for each iteration. The molecular dynamics simulations are performed with a time step of 7 fs. In order to adjust the pressure to 1 atm without affecting the RDFs, a correction term, the so called ramp correction, is added a posteriori to the optimized potential. It varies linearly with the bead-bead distance and vanishes at the cut-off distance (1.2 nm).¹³ The slope of the ramp is adjusted until the system reaches a pressure of 1 atm. It is the same for all pairs and small enough as to not distort the RDFs. Since the pressure before the ramp correction is already close to the target pressure (~20 atm), only a few iterations are needed in order to reach 1 atm. After this further correction, simulations in the *NPT* ensemble are carried out at atmospheric pressure.

The CG force field corresponding to this mapping scheme describes accurately static properties and experimental data of PA-66 in a wide range of temperature above and below the CG force field developing one.¹¹ Therefore the results presented in the next section are obtained from only one set of interactions resulting from the IBI procedure run at 400 K. The nonbonded CG potential is available in tabulated form in the supplementary materials of Ref¹⁷.

5.3. Back-Mapping Procedure

The procedure of re-inserting the atoms into a CG structure is called reverse mapping or back-mapping. It is based on simple geometrical principles and it is a way to obtain well-equilibrated atomistic configurations of high molecular weight polymer chains.

Several back-mapping algorithms have been proposed for different polymers.¹⁸⁻²¹ When the mesoscale model is tailored on the atomic contour using atomic distributions to build up the CG force field, as is the present case, the zoom-in back to the atomic description is usually a simple geometrical problem. In some cases, as for Santangelo *et al.*,¹⁹ if the model is particularly coarse, or the beads contain asymmetric atoms and the polymer chain has a specific tacticity, a more sophisticated method must be followed: for instance, the atomic fragment inserted in the CG model must be chosen among several that correspond to the same type of bead. In the present case the fine CG model and the position of the bead centers, make the procedure of back-mapping easier. The algorithm described

here, indeed, quickly generates, after a short post-equilibration, a stable atomistic configuration. The entire strategy is based on the fact that the fragments making up beads are small enough and do not contain any internally flexible moieties; moreover within one fragment there are no atomistic backbone torsions. Therefore, the relative positions of the atoms collected inside the fragment (the internal conformation) can be chosen from configurations extracted from the original atomistic simulations. This means that, for example for the A beads, a configuration (atom distances, angles and torsions) of the atoms constituting the fragment is chosen randomly from the original atomistic trajectory and it is used as the only configuration for all the A beads. Separate fragments are used for the end beads AP and M3P. In this way, we create a one-to-one library where to each fragment corresponds *one* atomistic configuration. Moreover, the average values for all the backbone atomic distances connecting the beads (for instance the C-C bond between two M3 fragments or the C-N bond connecting A and M3) and angles (defined below and denoted as α and β in the text) calculated from the original atomistic simulations, are added to the library. These distances and angles are employed in the back-mapping procedure to connect the fragments.

The back-mapping procedure starts by placing at the center of the first CG bead (say the central methylene carbon for M3P) the proper atoms taken from the atomistic library configuration; then the chain is grown adding one bead after the other one according to the microstructure of the CG polymer chain. After having replaced the first bead (bead 1 in Figure 5.2) by its corresponding atomistic fragment, the center of the second atomistic fragment (say the carbonyl carbon for the A bead) is placed at the position of the second bead and so on. For each insertion, the orientation of the atomistic fragments is initially random. Thus, a rotation of the fragments is needed to correct the angles and distances among the atoms belonging to the atomistic backbone. The first rotation changes the angle (denoted α in Figure 5.2a) formed by the vector \vec{R} (connecting the centers of the fragments to be bonded) and the bond vector \vec{S} of the newly added fragment (fragment 2 in Figure 5.2, and in the present case of type A), until it reaches a value closest as possible to the library one. In order to make the correction, the added fragment (bead 2) is thus rotated around the axis (\vec{V} in Figure 5.2a) perpendicular to the plane formed by the vectors \vec{S} and \vec{R} . The second rotation adjusts the distance between the backbone atoms of the two fragments, which are to be linked. It is performed around the vector connecting the bead centers of mass (\vec{R} Figure 5.2b) until the distance d (i.e. the covalent bond of the backbone) satisfies as much as possible the reference value of the library. At this stage the third atomic fragment (bead 3 in Figure 5.2c, here type M3) is placed at the corresponding CG bead position. To make the back-mapping procedure more efficient, a third correction is applied to the orientation of the second fragment by rotating it around the vector \vec{S} , until the angle defining its

orientation with respect to the polymer chain backbone vector R' (denoted as β in Figure 5.2c) matches the library value. The atomistic model rebuilt so far (M3P-A) is ready to be connected with the third fragment (M3) that will be rotated following the two steps (a and b in Figure 5.2) reported before; and the procedure starts again until all the fragments are reinserted. Since all the degrees of freedom are coupled, we can expect that some angles or distances optimized during the previous steps must be further optimized. Moreover when all the chains in the box are back-mapped some overlaps between beads belonging to different chains can occur. Then, in order to relax the model completely, three different simulation steps are performed. Firstly, a simulation at constant density (same as the original atomistic density at the desired temperature) and temperature (400 K) is run for 3000 steps with a time step of 0.05 fs. During the simulation in order to optimize the bonded part of the potential, in the atomistic force fields all the nonbonded interactions are switched off. In this way all the angles can reach their equilibrium values; the reverse-mapping procedure turns out to be so efficient that we can use even at this preliminary stage the bond constraints. In the second stage of 10000 steps a soft core potential is applied to the nonbonded interactions. The soft-core potential is implemented in our simulation program YASP²² in the following way: The short range part (0-0.19 nm) of the nonbonded potential energy function is replaced by a cubic spline. The spline coefficients are chosen to satisfy four conditions: the spline matches the value (i) and the derivative (ii) of the original potential energy function at the crossover distance; its derivative is zero at an interatomic distance r of zero (iii); most importantly, its value V_0 at $r = 0$ is finite (iv). This gets rid of the singularity at $r = 0$ and allows atoms to pass through each other and allows the relaxation of high-energy entanglements. Since the back-mapped systems are already in quite a good configuration and only few overlaps are present, only a short relaxation simulation with $V_0 = 1000$ kJ/mol is needed. These calculations are done with a time step of 1 fs. In the third stage, the full potential is turned on and a short simulation at constant volume is run with a time step of 2 fs. Finally after this preparation protocol, simulations at constant pressure are performed for 5 ns.

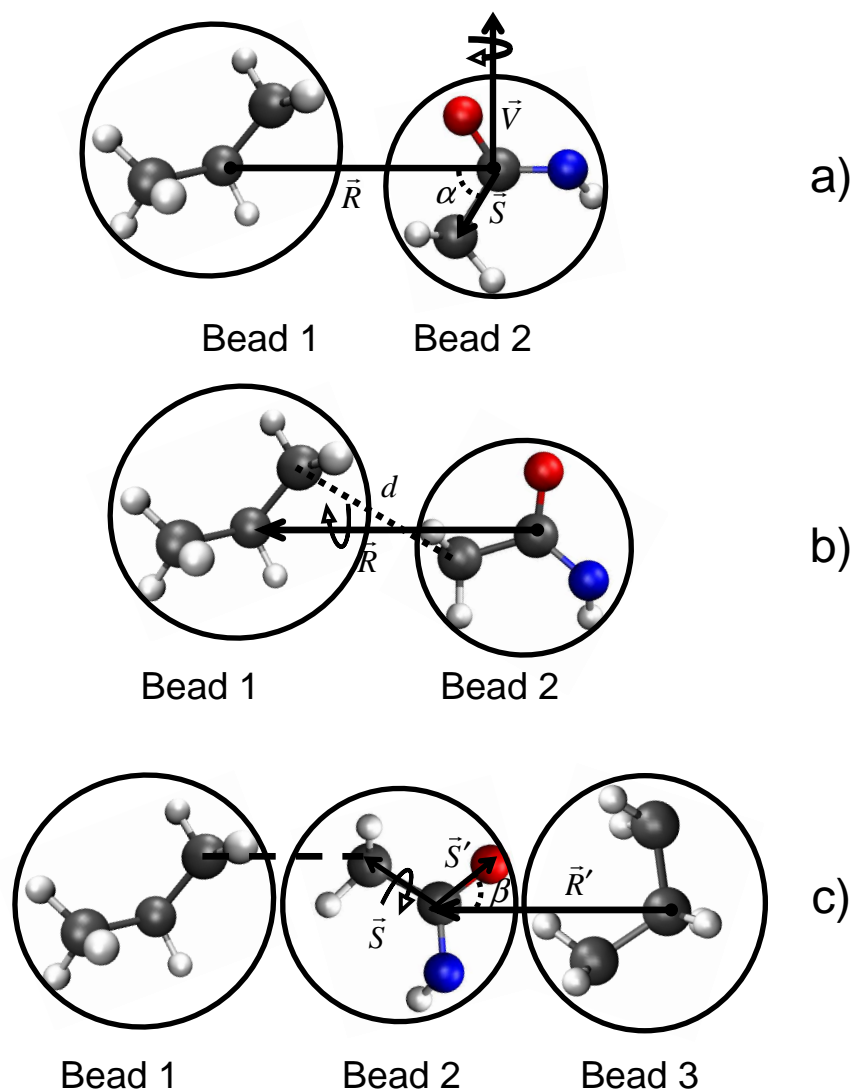


Figure 5.2. Scheme of the back-mapping algorithm. The labels used to define distances, angles and vectors are described in the text. Arrows indicate the rotation around vectors. The fragments are depicted with different colours that correspond to the different atoms: white hydrogen, grey carbon, blue nitrogen, red oxygen. The dashed line (---) represents the formed atomistic backbone bond.

5.4. Results and Discussion

5.4.1. Validation of the Back-Mapping Procedure

In order to validate the back-mapping procedure structural information obtained from atomistic simulations run after the reinsertion of the atoms are compared with the original atomistic simulations used to develop the CG force field. Figure 5.3 compares the radial distribution function calculated for the amide groups, the distribution of A-M2 bond and M3-A-M2 angle extracted from the atomistic simulation of the back-mapped model at 400 K and the original simulations used to develop the CG

potential. Similar good agreement is found also for the other distributions (not shown). The back-mapping procedure proposed here turns out to be very robust, so that the protocol of coarse-graining, equilibration at the coarse-grained level and back-mapping provides a means to relax high molecular weight polyamide. As it has been shown recently for polystyrene²³ CG simulations are a way to relax even entangled polymers, and the further reinsertion of the atomistic details allows to investigate well-relaxed polymer matrices with molecular weight comparable with experiment. In addition, in the case of polyamides this procedure may be of help in investigating the crystallization mechanism which is a key point in the understanding of their general properties.

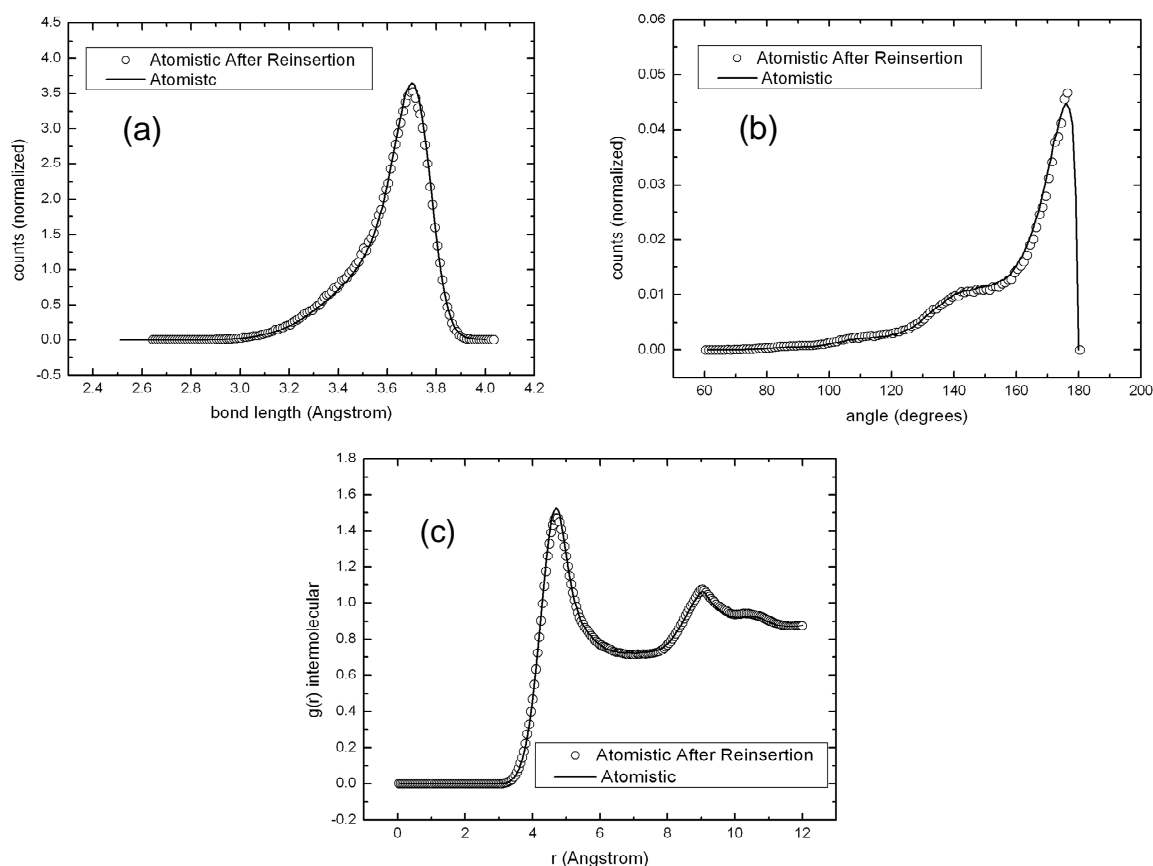


Figure 5.3. Histogram of A-M3 bond length (a), A-M2-A angle (b) and interchain radial distribution functions A-A pairs (c) extracted from atomistic (solid line) and CG after reinsertion of atomistic detail (empty circles) at 400K.

In Table 5.1 structural properties obtained from CG, original atomistic and back-mapped atomistic simulations are compared with the available experimental data. Since experimentally polyamides are usually found in semi-crystalline phase, structural data of the amorphous state are rather limited in literature. Moreover the molecular weight (M_w) of our models is lower than the typical experimental range and the models cannot form entanglements (our M_w (4540 g/mol) is barely

behind the critical mass reported in literature as 4700 g/mol).²⁴ We separate the comparison of the data in two steps: first we analyze the differences within the models and then we compare the simulation results with the experimental data. The gyration radius (R_g) and the end-to-end distance (R_0) values of the three models show that during the CG simulation a further relaxation of the systems (although small) occurs. The values of the original atomistic and back-mapped models slightly differ showing a relatively better agreement with the experimental data for the back-mapped model. Here we have to point out that the experimental R_0 reported in the table (6.4 nm) corresponds to the critical end-to-end distance (R_c) at which the entanglement occur assuming a critical mass (M_c) of 4700 g/mol. R_c is calculated through this formula²⁵

$$R_c = M_c^{1/2} \left(\langle R_0^2 \rangle / M_w \right)^{1/2} \quad (5-4)$$

where $\langle R_0^2 \rangle$ is the averaged end-to-end distance for a polymer chain of molecular weight M_w . From R_0 the characteristic ratio (C_n) can be calculated through the formula

$$C_n = \langle R_0^2 \rangle / nl^2 \quad (5-5)$$

where n is the number of backbone bonds and l their averaged length. For long chains C_n converges to a single value usually known as C_∞ . The numbers obtained from the simulations cannot be well compared with the experimental datum due to the low M_w of our models. More interesting is to compare the ratio among the end-to-end distance and the corresponding molecular weight $\left(\langle R_0^2 \rangle / M_w \right)^{1/2}$. Normalizing with respect to the M_w our results agree well with the experimental one and the back-mapped even slightly better than the original atomistic model. Since we are interested in investigating the HBs we firstly focus our attention on their amount counting their V. group and the acceptor O has to be below 0.297 nm²⁶ and the donor-hydrogen-acceptor angle above 130°. This criterion has turned out to be reliable in identifying HB in PA-66.⁹ The average fraction (averaged on the trajectory) of the HBs (number of amide-amide hydrogen bonds per amide groups) calculated for the original atomic model and for the back-mapped one are reported in the last row of Table 5.1. The difference among the numbers is almost negligible confirming that this CG force field is able to describe correctly all the static properties of the PA-66 also those that have been not explicitly considered in its developing in a broad range of temperature.²⁷

Table 5.1. Static properties for polyamide-66 obtained from the original atomistic simulations (before coarse-graining), the coarse-grained simulations and the atomistic simulation after back-mapping. If not specified in parenthesis the results are obtained at 400 K.

	Original atomistic ^a	Coarse grained	Backmapped atomistic	Expt.
Density [g/cm ³]	1.06	1.06	1.06	1.10 ^b (T=533 K)
Gyration radius [nm]	3.4±0.9	3.0±0.5	3.1±0.8	-
End-to-end distance [nm]	7.4±0.3	6.6±0.2	7.0±0.3	6.4 ^{c,d}
Persistence length [nm]	8.2±0.1 7.0±0.1 (T=500K)	7.5±0.1 6.3±0.1 (T=500 K)	7.4±0.3	5.3 ^c
$\langle\langle R^2 \rangle_0 / M \rangle^{1/2}$ [Å]	1.09±0.05 1.01±0.04 (T=500K)	0.98±0.03 0.94±0.02 (T=500K)	1.03±0.04	0.94 ^c
C_∞	4.0	3.2	4.5	6.1 ^c
Fraction of HB	0.71±0.01	-	0.70±0.01	0.87 ^e

^a Ref. ¹¹

^b Ref. ²⁸

^c Ref. ²⁴⁻²⁹ The temperature of the experiment is not reported. Values obtained from intrinsic viscosity measurements. Results corresponding to molecular weight larger than 4700 g/mol.

^d Critical end-to-end distance for entanglements calculated from the critical molecular weight ($M_c=4700$ g/mol) through the following relation: $R_c = M_c^{1/2} \langle\langle R_0^2 \rangle / M \rangle^{1/2}$ (see text)

^e Ref. ²⁷. The experimental value corresponds to the fraction of HBs in a semi-crystalline phase of PA-66 calculated by Fourier-transform infrared spectroscopy.

5.4.2. Chain Stiffness

The rigidity of the polymer chain is usually enhanced by the presence of intra or inter-molecular HBs.^{30,31} An estimation of the chain stiffness can be obtained calculating the persistence length (L_p) that measures the length along the chain over which the tangent vectors of the chain become decorrelated. In a simulation, L_p can be directly evaluated from the correlation of the bonds along the chain:

$$C_{DD}(k) = \langle\langle (\mathbf{D}_i \mathbf{D}_{i+1} \cdot \mathbf{D}_{i+k} \mathbf{D}_{i+k+1}) / \|\mathbf{D}_i \mathbf{D}_{i+1}\| \|\mathbf{D}_{i+k} \mathbf{D}_{i+k+1}\| \rangle \rangle \quad (5-6)$$

where $\mathbf{D}_i \mathbf{D}_{i+1}$ is the vector separating the i th and $(i+1)$ th bead of the chain. The average is performed over all positions of i along the chain for all the backbone vectors, and over all frames of the trajectory

file. In order to calculate the persistence length, the autocorrelation function $C_{DD}(k)$ is fitted to the following exponential form:

$$C_{DD}(k) \approx C_0 \exp(-k/L_p) \quad (5-7)$$

The least-squares fit of the $C_{DD}(k)$ data gives the L_p in units of bond lengths. The variation of the persistence length with temperature is calculated from the original atomistic and CG simulations (Figure 5.4). For a meaningful comparison L_p is calculated on a pseudo-CG trajectory mapped on the atomistic one. For every temperature the atomic model turns out to be slightly stiffer than the CG one. Moreover, whereas the CG model shows a constant decrease of L_p with the increasing of the temperature (except at very low temperatures), the atomic model shows an almost constant L_p until 450 K and a further drop off for higher temperatures. Since the rigidity of the polymer chain is mainly due to the presence of the HBs, such transition might be associated with a decrease in the HBs strength when the temperature increases. In fact, in the atomic model in a comparable temperature range the self diffusion coefficient changes of about 2 orders of magnitude and a decrease in the number of HBs is also observed (see also Table 5.1 and 2).^{9,11} In the next paragraph the relation among the relaxation of the HB network and the self diffusion coefficients will be discussed and possible reasons for the lack of such transition in the persistence length of the CG model will be presented.

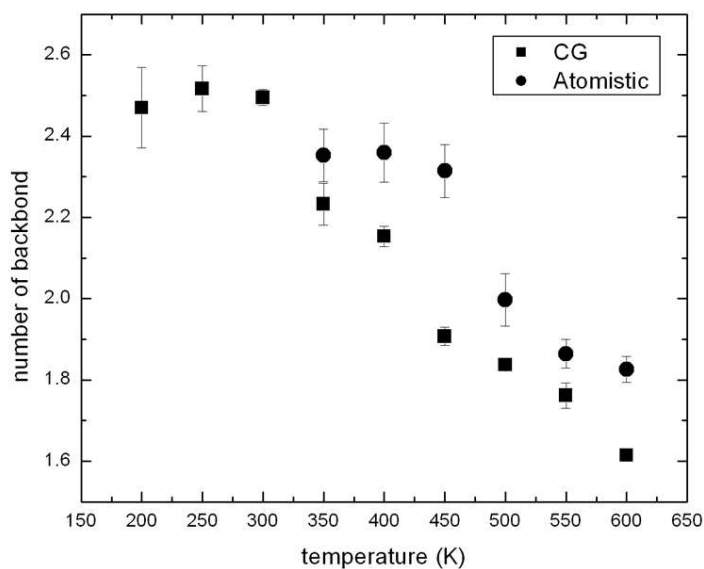


Figure 5.4. Persistence lengths in number of backbone bonds obtained from the pseudo-CG and CG simulations at different temperatures. To obtain the value of the L_p in nm we consider an averaged value for the CG bond of 3.5 nm.

5.4.3. Hydrogen Bond Analysis

In chapter 4 by means of atomistic simulations we have shown that the global dynamics of unentangled polyamide-66 is governed by the relaxation of the hydrogen-bond network formed among the amide groups, and by looking at the behavior of the self diffusion coefficient and the relaxation times of the HBs we identified a crossover temperature at ~ 413 K (T_c).⁹ At this temperature an evident transition from a Vogel-Fulcher-Tammann to an Arrhenius behavior has been seen changing the temperature from above. The presence of a dynamic crossover at a temperature slightly higher than the nominal glass transition one was in agreement with the more recent experimental data and glass theories.³²⁻³⁵ The dynamics of the HB among the polyamide chains were analyzed in terms of two time correlation functions, namely, the continuous hydrogen bond time correlation function, $S(t)$, and the intermittent hydrogen bond time correlation function, $C(t)$, defined as^{36,37}

$$S(t) = \frac{\langle h(0)H(t) \rangle}{\langle h \rangle} \quad (5-8)$$

and

$$C(t) = \frac{\langle h(0)h(t) \rangle}{\langle h \rangle} \quad (5-9)$$

In the equations the variable $h(t)$ is unity when a specific pair of sites is hydrogen-bonded at time t , while the variable $H(t)$ is unity when the tagged pair of sites remain continuously hydrogen bonded from $t = 0$ to time t , and zero otherwise.

The aim of the analysis presented here is two-fold: firstly to find a suitable way to investigate the HB dynamics in the CG model (since the atoms involved in the interaction are not explicitly described but lumped into beads), secondly to compare the CG “hydrogen-bond” dynamics with the atomistic results. Our CG model includes the atoms defining the HB (the hydrogen of the NH donor group and the carbonylic oxygen acceptor) in the A bead. Thus the idea is to use a geometrical criterion involving these beads to identify the HB. The criterion chosen is based only on the distance among A beads: we consider two A beads “hydrogen bonded” if their distance is less than 0.52 nm (R_{HB}). In this definition of “hydrogen bonds” (CG-HB) the directionality of the bonds is lost as a consequence of mapping the donor and acceptor atoms into spherical beads. The value of R_{HB} is chosen after analyzing the atomistic simulations. It is the largest possible distance between two carbonyl carbons, for which there still is a HB present between the two amide groups.

In order to verify the chosen criterion we first calculate the CG-HB using the atomistic trajectories. Figures 5a and b show respectively intermittent hydrogen bond time correlation function

$(C_{AA}^{am}(t))$ calculated among the carbonyl atoms (corresponding to the center of the A bead) and the corresponding relaxation times (τ_R^{am}) calculated from the original atomistic simulations run at different temperatures. The multiexponential functions used to fit the time correlation functions $C_{AA}^{am}(t)$ and the resulting τ_R^{am} are reported in Table A.1.3 of the Appendix.1.¹⁰ These curves show the same cross-over transition as corresponding analyses in ref.⁹, which used a more conventional definition of the hydrogen bond based on atomic distances and angles. Figure 5.5b shows clearly that the simple carbon-carbon distance criterion among the A beads can be used as a qualitative definition of the HB in the atomistic model: the plot shows a transition at ~ 430 K in agreement with the T_c value found in the atomistic simulations ($T_c \approx 413$ K). The results for τ_R^{am} can be fitted by the Vogel-Fulcher-Tammann (VFT) form for $T \geq 430$ K ($\tau_R \propto e^{A/T_0/(T-T_0)}$ where A and T_0 are the fitting parameters), and by the Arrhenius equation for lower temperatures ($\tau_R \propto e^{E_a/k_B T}$ where E_a is the fitting parameter and K_B is the Boltzmann constant). Moreover, the activation energy in the Arrhenius part ($E_a = 13.4$ kJ/mol) turns out in reasonable agreement with conventional HB definition ($E_a = 22.8$ kJ/mol).⁹

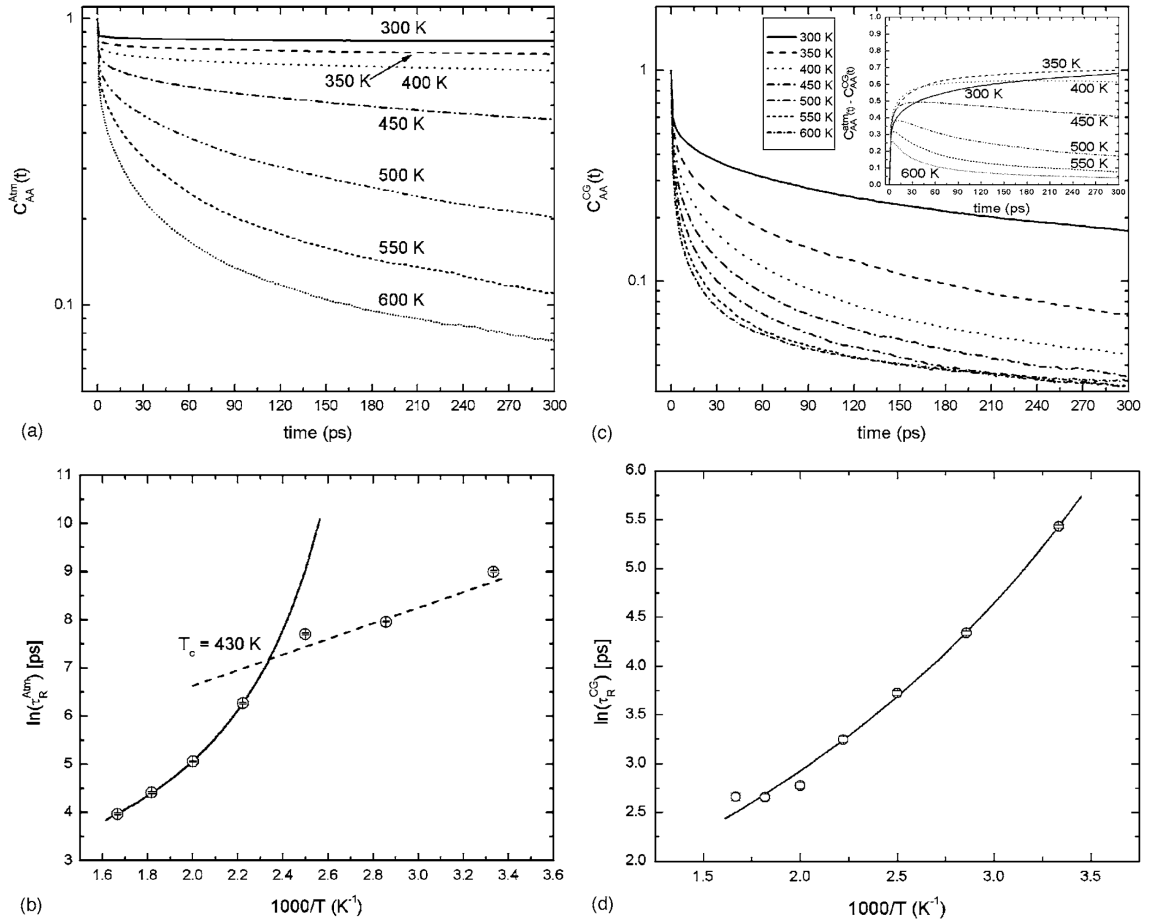


Figure 5.5. a) c): The time correlation functions, $C_{AA}^{\text{atm}}(t)$ $C_{AA}^{\text{CG}}(t)$, for hydrogen bonds between of the amide groups at different temperatures for the atomistic and CG simulations calculated from MD trajectories saved every 1 ps (atomistic) and 1.4 ps (CG). b) d): Temperature dependence of structure relaxation time plotted as $\log(\tau_R)$ vs $1000/T$ for the atomistic ($\log(\tau_R^{\text{atm}})$) and CG ($\log(\tau_R^{\text{CG}})$) simulations. Dash line denotes the fit to an Arrhenius law and solid line denotes the fit to Vogel-Fulcher-Tamman (VFT) law. In the inset the difference among $C_{AA}^{\text{atm}}(t)$ and $C_{AA}^{\text{CG}}(t)$ is reported for all the simulation temperatures.

Supported by these results we apply the same distance criterion to the CG simulations. Figure 5.5c and d report the intermittent hydrogen bond time correlation function calculated using the CG trajectories ($C_{AA}^{\text{CG}}(t)$) and the corresponding relaxation time τ_R^{CG} , while the multiexponential fitting parameters are reported in the Table A.1.4 of the Appendix.1. {Groot, 1997 #90} In this case the results for τ_R^{CG} can be fitted by the VFT equation over the entire range of temperature showing no changes in their trend. Moreover, as expected, the τ_R^{CG} are smaller than the τ_R^{atm} at each temperature. Their difference becomes remarkable at low temperature, showing a bigger mobility of the HB network in the CG model than in the atomistic one especially for temperatures lower than 500 K. In order to

compare the different relaxation processes involved in the decorrelation of $C_{AA}^{CG}(t)$ and $C_{AA}^{am}(t)$ we calculate the difference function $F(t)$ ($F(t) = C_{AA}^{am}(t) - C_{AA}^{CG}(t)$) at each temperature (inset of Figure 5.5c). At high temperature ($T \geq 500$ K) $F(t)$ initially increases then starts to decay. This is due to the fact that at short time the two correlation functions relax with a different behavior ($C_{AA}^{am}(t)$ slower than $C_{AA}^{CG}(t)$) then after a certain time depending on the temperature, they decay to zero in a similar way. On the contrary at low temperatures $F(t)$ does not relax and only for temperature $T=450$ K shows a moderate decay. For $350K \leq T < 500K$ the two correlation functions are in fact characterized by different relaxation processes and at lower the temperature the difference is more remarkable: while $C_{AA}^{CG}(t)$ relaxes to zero within 500 ps even at very low temperature (350 K), $C_{AA}^{am}(t)$ does not show any decay in the same time scale. These results highlight the fact the temperature dependence of the HB network is different in the CG and the atomic model and that lowering the temperature enhances this difference.¹¹ A possible theoretical explanation for the lack of the crossover transition in the CG HBs dynamics can lie in the flat potential energy surface of the CG model. The recent theory formulated by Di Marzio and Yang³² proposes a kinetic model to explain the fragile-to-strong transition occurring in the dynamic properties in glass forming material. Their model is based on the fact that the lower is the temperature the deeper are the potential wells where the particle can be trapped. As the temperature approaches the critical temperature T_c (usually slightly higher than the glass transition temperature) the rate determining step of the particle motion becomes the rate of escape from one of the potential holes. At T_c the material becomes highly viscous and a further drop in temperature provokes the transition to a glassy material where the particles are trapped in an infinitely deep energy well. The shallow energy wells characterizing the CG potential surface make the temperature effect almost negligible at least for temperatures down to 200 K. The chain mobility is reduced by lowering the temperature but it seems that the molecules do not get trapped in the energy holes. This result suggests that temperature dependence of the viscoelastic properties (such as the viscosity) could be not correctly described.

The weakness of the CG HB can be drawn looking at the continuous hydrogen bond time correlation function ($S_{AA}^{CG}(t)$) (see Figure 5.6a) and the temperature dependence of its corresponding relaxation time τ_{HB}^{CG} (Figure 5.6b) from whose slope an activation energy (E_a) for the rupture of CG-HB can be obtained. E_a is 3.85 kJ/mol compared with a value of 10.5 kJ/mol found from the atomistic simulations.

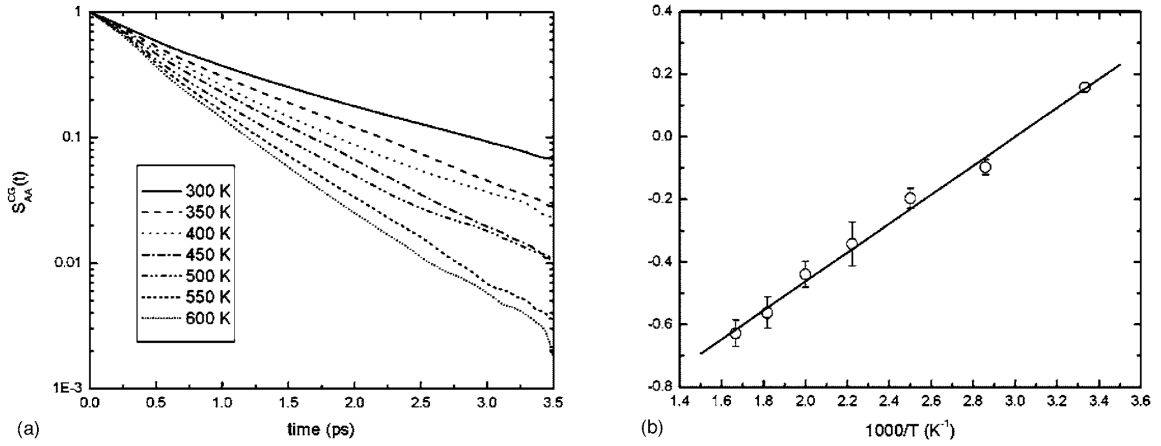


Figure 5.6. a) Time correlation function $S_{AA}^{CG}(t)$, calculated from MD trajectories saved every 7 fs, for hydrogen bond between the amide groups at different temperatures in the CG simulations b) Hydrogen bond lifetimes τ_{HB}^{CG} obtained from $S_{AA}^{CG}(t)$. The solid line represents the linear fit through the points.

In chapter 3 where we discussed about the transferability of coarse-grained force fields,¹¹ the center-of-chain self diffusion coefficients (D) of the atomistic and CG PA-66 at different temperatures have compared and we have calculated a scaling factor (s), which accounts for the speed up of the CG model, by simply computing the ratio between the two self diffusion coefficients. We found that s is temperature dependent. Table 5.2 reports the relaxation times (τ_R^{atm} , τ_R^{CG}) calculated for different

temperatures and the scaling factors calculated for D ($s^D = \frac{D^{CG}}{D^{atm}}$) and for τ_R ($s^\tau = \frac{\tau_R^{atm}}{\tau_R^{CG}}$). Figure 5.7a

shows that when $1/D$ and τ_R are normalized with respect to their value at 600 K their temperature dependence is represented by a single curve. This proves that, as it has been found by means of atomistic simulations,⁹ in the CG simulations the dynamics of polyamides is strongly coupled to the mobility of the HB network, and at each temperature D is inversely proportional to τ_R . A relation

among s^D and s^τ can be drawn based on the curve of Figure 5.7a where $\ln\left(\frac{D(T_0)}{D(T)}\right) \cong \ln\left(\frac{\tau_R(T)}{\tau_R(T_0)}\right)$, from

which arises that the product $D(T) \cdot \tau_R(T)$ must be constant at each temperature. From our simulations $D^{atm}(T) \cdot \tau_R^{atm}(T) \cong 6.6 \cdot 10^{-6}$ and $D^{CG}(T) \cdot \tau_R^{CG}(T) \cong 3.1 \cdot 10^{-6}$ for the atomistic and CG models respectively;

then, s^D turns out to be around twice as s^τ ($s^D \cong 2.13 \cdot s^\tau$). Figure 5.7b shows the good overlapping of the two scaling factor accounting for the constant factor 2.13. Hence, two stronger effects contribute to the values of s^D : *i*) the hydrogen bonds relaxation dynamics (s^τ), responsible for the temperature dependence, and *ii*) the soft potential acting among the beads. The latter contribution

is constant with the temperature and depends on the number of degrees of freedom coarse-grained away and on the procedure (based on the inversion of the RDF) used to develop the CG force field.

Table 5.2. Structural relaxation times of hydrogen bonds calculated for atomistic (τ_R^{atm}) and CG (τ_R^{CG}) simulations. The last two columns report the time scaling factors calculated from the τ_R (s^τ) as well as from the chain centre-of-mass diffusion coefficients D (s^D).

Temperature (K)	τ_R^{atm} (ps) ^a	τ_R^{CG} (ps)	s^D ^b	s^τ
600	43 ± 1	14.3 ± 0.6	5.8 ± 3.3	3.0 ± 0.2
550	72 ± 2	14.2 ± 0.5	12.3 ± 8.6	5.1 ± 0.2
500	174 ± 4	16.0 ± 0.5	30.1 ± 18.5	10.9 ± 0.4
450	934 ± 11	25.7 ± 0.7	55.8 ± 18.4	36.3 ± 1.1
400	9 302 ± 64	41.3 ± 0.9	461.8 ± 294.9	225.1 ± 5.3
350	24 138 ± 100	76.7 ± 1.5	606.5 ± 377.7	314.5 ± 6.2

^a See Ref. ¹¹

^b See Ref. ⁹

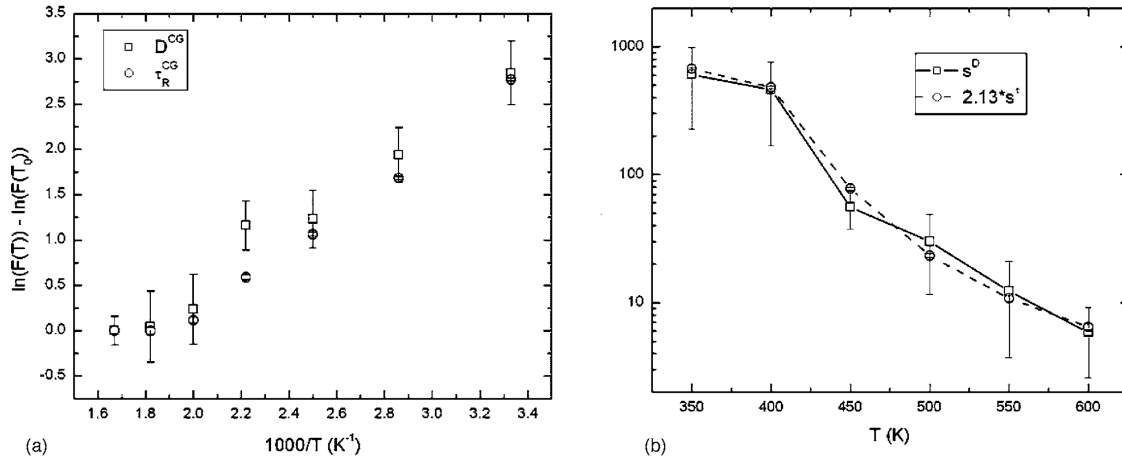


Figure 5.7. a) Master curve for the chain centre-of-mass diffusion coefficient ($F=1/D$) and τ_R ($F=\tau_R$) normalized with respect to their value at 600 K ($T_0 = 600K$); b) behaviour of the scaling factor coming from the diffusion coefficient ($s^D = D^{CG}/D^{atm}$) and from the hydrogen bonds correlation functions $C_{AA}(t)$ ($s^\tau = \tau_R^{atm}/\tau_R^{CG}$).

5.5. Conclusions

In this contribution we have analyzed the static and dynamic properties of hydrogen bonds in a CG model of PA-66. The geometric definition of a hydrogen bond has been simplified so it works not only for the atomistic model (where it was validated) but also for the CG model, where the atoms defining hydrogen bonds are only implicitly included. Looking at the results obtained from the back-

mapping procedure we have shown that the CG force field can be confidently used in studying static properties in a broad range of temperature but the dynamics of the system is correctly described only at high temperature ($T > 400$ K). We have found that the structure relaxation time for the CG model is much shorter than for the atomic model, especially at low temperatures. In particular, in contrast with what we have found by means of atomistic simulations, the temperature dependence of the CG dynamics does not show any transitions and can be described in the entire range of temperatures using the Vogel-Fulcher-Tammann law. As expected the τ_R^{atm} are higher than τ_R^{CG} confirming the artificial acceleration of the CG dynamics. The weakness of the CG-HB might be due to the lack of directionality as a consequence of mapping scheme where the donor and acceptor atoms are lumped into spherical beads. We have defined a master curve for D and τ_R and showed that their behavior with the temperature is coupled. Hence, the temperature dependence of the scaling factor s^D accounts both the softer CG potential acting between the beads (temperature independent) and the temperature dependent hydrogen bond relaxation times which are more underestimated at low temperatures. Hence, as it happens for biological systems, the necessity to introduce explicitly a new interaction accounting the directionality of the HBs and their increasing strength with the decrease of the temperature, is probably fundamental to analyze processes such as the self assembly or crystallization that are governed by their dynamics.

5.6. References

- (1) Steiner, T. *Angew. Chem., Int. Ed.* **2002**, *41*, 48-76.
- (2) De Sancho, D.; Rey, A. *J. Comput. Chem.* **2007**, *28*, 1187-1199.
- (3) Kohan, M. I. *Nylon Plastics Handbook*; Hanser Gardener: Cincinnati, 1995.
- (4) Miura, H.; Hirschinger, J.; English, A. D. *Macromolecules* **1990**, *23*, 2153.
- (5) Murthy, N. S. *J. Polym. Sci. B* **2006**, *44*, 1763.
- (6) Murthy, N. S.; Wang, Z.-G.; Hsiao, B. S. *Macromolecules* **1999**, *32*, 5594-5599.
- (7) Jones, N. A.; Atkins, E. D. T.; Hill, M. J.; Cooper, S. J.; Franco, L. *Macromolecules* **1997**, *30*, 3569-3578.
- (8) Skrovanek, D. J.; Howe, S. E.; Painter, P. C.; Coleman, M. M. *Macromolecules* **1985**, *18*, 1676.
- (9) Karimi-Varzaneh, H. A.; Carbone, P.; Müller-Plathe, F. *Macromolecules* **2008**, *41*, 7211.
- (10) See EPAPS Document No. E-JCPSA6-129-007839 for the force field parameters and for the correlation function fitting parameters. For more information on EPAPS, see <http://www.aip.org/pubservs/epaps.html>.
- (11) Carbone, P.; Varzaneh, H. A. K.; Chen, X.; Müller-Plathe, F. *J. Chem. Phys.* **2008**, *128*, 064904.
- (12) Reith, D.; Patz, M.; Müller-Plathe, F. *J. Comput. Chem.* **2003**, *24*, 1624.
- (13) Müller-Plathe, F. *ChemPhysChem* **2002**, *3*, 754-769.
- (14) Tschop, W.; Kremer, K.; Batoulis, J.; Burger, T.; Hahn, O. *Acta Polymer* **1998**, *49*, 61.
- (15) Milano, G., S. Goudeau, F. Müller-Plathe *J. Polym. Sci., Part B: Polym. Phys.* **2005**, *43*.
- (16) Karimi-Varzaneh, H. A.; Qian, H.-J.; Chen, X.; Carbone, P.; Müller-Plathe, F. *In Preparation* **2009**.
- (17) Karimi-Varzaneh, H. A.; Carbone, P.; Müller-Plathe, F. *J. Chem. Phys.* **2008**, *129*, 154904.
- (18) Tschop, W.; Kremer, K.; Han, O.; Batoulis, J.; Burger, T. *Acta Polymer* **1998**, *49*, 75.
- (19) Santangelo G.; Di Matteo A.; Müller-Plathe, F.; Milano, G. *J. Phys. Chem. B* **2007**, *111*, 2765-2773.
- (20) Queyroy, S.; Neyertz, S.; Brown, D.; Müller-Plathe, F. *Macromolecules* **2004**, *37*, 7338.
- (21) Hess, B.; Leon, S.; van der Vergt, N.; Kremer, K. *Soft Matter* **2006**, *2*, 409.
- (22) Müller-Plathe, F. *Comput. Phys. Commun* **1993**, *78*, 77.
- (23) Spyriouni, T.; Tzoumanekas, C.; Theodorus, D.; Müller-Plathe, F.; Milano, G. *Macromolecules* **2007**, *40*, 3876.
- (24) Zang, Y.-H.; Carreau, P. J. *J. Appl. Pol. Sci* **1991**, *42*, 1965.
- (25) Flory, P. J. *Statistical Mechanics of Chain Molecules*; Wiley: New York, 1969.
- (26) Garcia, D.; Starkweather, H. W. *J. Polym. Sci. Polym. Phys. Edi.* **1985**, *23*, 537.
- (27) Garcia, D.; Starkweather, H. W. *J. Polym. Sci., Part B: Polym. Phys.* **1985**, *23*, 537.
- (28) Wang, Y. Z.; Chia, W. J.; Hsieh, K. H.; Tseng, H. C. *J. Appl. Pol. Sci.* **1992**, *44*, 1731.
- (29) Aharoni, S. M. *Macromolecules* **1983**, *16*, 1722.
- (30) Seger, B.; Burchard, W. *Macromolecular Symposia* **1994**, *83*, 291.
- (31) Hanemann, O.; Ballauff, M. *Macromolecules* **1997**, *30*, 7638.
- (32) DiMarzio, E. A.; Yang, A. J. M. *J. Res. Natl. Inst. Stand. Technol.* **1997**, *102*, 135.
- (33) Baeurle, S. A.; Hotta, A.; Gusev, A. A. *Polymer* **2006**, *47*, 6243.
- (34) Kisliuk, A.; Mathers, R. T.; Sokolov, A. *J. Polym. Sci., Part B: Polym. Phys.* **2000**, *38*, 2785.

-
- (35) Gerardin, J.; Mohanty, S.; Mohanty, U. *J. Chem. Phys.* **2003**, *119*, 4473.
- (36) Chanda, J.; Chakraborty, S.; Bandyopadhyay, S. *J. Phys. Chem. B* **2006**, *110*, 3791-3797.
- (37) Starr, F. W.; Nielsen, S. O.; Stanley, H. E. *PRL* **1999**, *82*, 2294.

6. Fine-Graining Without Coarse-Graining: An Easy and Fast Way to Equilibrate Dense Polymer Melts

6.1. Introduction

In materials science, atomistic simulations have become in the last years a powerful tool to predict properties, to verify theories or to explain experimental findings.¹⁻³ In particular, in polymer science the resort to molecular simulations has remarkably increased after the advent of high performance computers that allow to simulate models composed by thousands of atoms in a reasonable time. However, despite the improvement in the hardware, modeling high-molecular-weight polymer melts is still a computational challenge. Many striking features of polymers (including their viscoelastic behavior) depend indeed on the fact that the monomers are bonded together following a specific topology. The chain connectivity makes the conformational space to be sampled very broad and characterized by a complex energy landscape. Therefore, specific simulation techniques must be developed in order to efficiently explore the conformation space and gain information about the structure and dynamics of a polymer melt avoiding the system being trapped in the neighborhood of the initial configuration.

An effective way to simulate polymers must then match two conflicting requirements in the model description: (i) The structures and models need detailed atomistic resolution to capture subtleties in the polymer-polymer interactions and to allow comparison with experimental information. (ii) The prepared structures must cover a large spatial domain to capture the large-scale structural features and processes inherent in the polymeric materials. Due to computer-time limitations, one can either have the fine resolution or the large spatial dimension or an unsatisfactory compromise between the two.

Different approaches have been proposed in the past to efficiently relax high molecular weight polymer melts. These methods can be roughly divided in two classes based on the level of resolution of the model. The first consists of techniques where the atomistic models are subjected to specific algorithms (usually Monte Carlo (MC)) able to quickly sample the conformational energy surface and find a good local minimum.⁴⁻⁷ An example of such methods is the advanced off lattice MC algorithm (end-bridging MC) proposed recently by Theodorou and coworker,⁸ where the MC moves involve large segments of the polymeric chain altering their connectivity. This connectivity-altering move (and its variant)⁹ has proved to greatly enhance the sampling efficiency of the configurations. During such

move, two chains are selected so that the end of one is within a certain bridging distance from a backbone segment of the other. A trimer centered at this latter backbone segment is excised from the second chain, thus defining two subchains. The end of one of these subchains is connected to the end of the first chain by constructing a bridging trimer, forming a new chain with prescribed molecular geometry (bond lengths and bond angles). The selection of the chains, the building of the bridging trimer, and the acceptance criteria of the method are designed so that the requirements of microscopic reversibility for proper sampling are satisfied. Using this technique various high molecular weight (M_w) polymers (polyethylene,^{8,10} polyisoprene,¹¹ poly(ethylene-oxide)¹²) have been simulated and the results compared successfully with the experimental numbers.

Using again the MC technique, Neyertz and Brown¹³ proposed a different set of moves (pivot MC) based on Flory's hypothesis, .i.e., that polymer configurations in a pure melt are very similar to those obtained by sampling an isolated molecule where only a certain number of specific near-neighbor atoms interact. Molecular configurations are generated using a pivot MC algorithm that efficiently samples the bond-angle and torsional phase space of isolated chains. Only interactions between backbone sites separated by a fixed number of backbone bonds (n_{bonds}) are considered at this stage. A collection of such chains are then randomly placed within the confines of a periodic simulation box and the excluded volume is introduced. The choice of the n_{bond} value depends on the chemistry of the polymer chain. This method has been successfully applied to study melt of various unentangled polymers.¹³⁻¹⁵

Both MC methods have been proved to efficiently relax high M_w polymers but the first (the end bridging MC) is difficult to implement, and the second (the pivot MC) can be less efficient in equilibrating highly rigid polymers (where the value of n_{bond} becomes very high) or polymers where long range interactions (like the electrostatic ones) do have a significant influence on the structure of the chain conformations in the bulk melt.

In a second class of methods, a coarser (than atomistic) model is subjected to a standard molecular dynamics (MD) simulation in order to relax the long range structure. The reduction of the degrees of freedom in the model is necessary to speed up the relaxation process and allows the use of a conventional MD algorithm to sample the conformational space. After relaxing the structure at the coarse-grained level, the omitted details (the atoms) are re-introduced (reverse-mapping procedure) into the model. This procedure has been used to successfully study entangled^{16,17} and unentangled^{15,18} polymer melts. Moreover, there is a further advantage in using the MD technique, since additional qualitatively information about dynamic properties¹⁹⁻²¹ can be gained from the resulting trajectories.

To achieve a quicker relaxation, an interesting combination of these two families of methods has been also proposed.^{17,22} In particular Spyriouni and coworkers¹⁷ were able to equilibrate entangled

atactic polystyrene melts applying the end-bridging MC algorithm to a coarse-grained model of polystyrene. The so relaxed coarse-grained structure was subsequently reverse-mapped to obtain the atomistic structures.

However, these latter methods present difficulties in the implementation (the development of the force field for the coarser model is not trivial²³) and can lead to a wrong description of the local structure (after the atoms have been re-inserted) if the coarse-grained model has sampled conformational states forbidden to the atomistic one.

Here is presented a new and easy procedure to quickly equilibrate entangled linear polymers. The method proposes the use of a reverse-mapping (or fine graining) technique to generate an atomistic polymer structure directly from a generic polymer model. This method (here called “fine-graining”) requires only two steps: the generation of a random walk path (representing the averaged conformational state of a generic polymer chain in a melt) and the subsequent insertion of the atomistic details following the trace of the random walk. After inserting the missing atoms into the generic polymer structure, few simulation steps are further required to re-form backbone bonds among the monomers and to relax (locally) the newly formed atomic polymer chains. The method is applied to three types of amorphous polymer melts: polyethylene (PE), atactic polystyrene (a-PS) and polyamide-66 (PA-66). Results about global properties (gyration radius, end-to-end distance, radial distribution functions) and local structure (distribution of the dihedral angles, local reorientation of bonds) are compared with those obtained from other methods presented in literature and with experimental data.

6.2. Computational Method

6.2.1. Continuum Random Walk

It is commonly accepted that in concentrated solution or melt polymers display random-walk conformational properties on length-scales much larger than the monomer diameter. This means that there is no long range correlation between subsequent bonds when these two bonds are separated by a specific number of monomers (n_m) along the chain (“Flory ideality hypothesis”).²⁴ The value of n_m (Kuhn length) defines the chain stiffness and its length (l_k), usually given in nm and not in monomer units, can be measured experimentally. Therefore, knowing the value of l_k for a specific polymer, it is possible to build a random walk chain whose monomer length is l_k .

Here, an off-lattice Continuum Random Walk (CRW) algorithm is implemented to generate random walk chains characterized by different l_k s. The values of l_k for the different polymers are taken from the literature; the algorithm allows the monomer length to oscillate around the specified

average value $\langle l_K \rangle$ following a Gaussian distribution of standard deviation equal to 2% of $\langle l_K \rangle$. The width of the distribution is chosen considering a small fluctuation of the of the Kuhn length due to experimental error. The fluctuation is anyway enough small to not affect the final results. The chains are randomly placed in a cubic simulation box whose dimensions correspond roughly to the experimental density of the polymer at a chosen temperature without paying attention to possible overlaps among the chains. The set of the correct density at this stage is not important as the correct value will be reached at the end of the reverse mapping procedure. A good guess (based on experimental data or previous simulation results) is anyway necessary to ensure the correct equilibration procedure.

6.2.2. Reverse Mapping

After generating the generic polymer chains by means of the CRW algorithm, atomistic chains are grown along their parent random walks (RW). The easiest way to do it is to populate each RW segment with a suitable atomistic fragment. As initial attempt the atomistic fragment inserted is treated as rigid and only one conformation for the backbone atoms (*all-trans*) is allowed. Thus, each atomistic moiety in its *trans* conformation is placed on each RW segment in a way that their geometric centers coincide (see Figure 6.1a); subsequently the atomic fragments are rotated around their center by a suitable angle to follow the RW tangent. The rotation angle is that between the vector formed by the centers of two subsequent RW segments and the one connecting the geometric center of the inserting fragment and its last atom (Figure 6.1b). In order to keep the global structure of the chains generated by the CRW, the center of the RW segments and of the inserted atomistic fragments are restrained to their positions during the relaxation steps with a restraining force constant of $1.0 \times 10^9 \text{ kJ} \cdot \text{mol}^{-1} \cdot \text{nm}^{-2}$.

There is not an established procedure to rebuild the backbone bonds among the inserted fragments and to relax (locally) the newly atomistic polymer chains; the recipe proposed here involves a set of several MD simulations, but other procedures, maybe more efficient, can be envisaged. During the MD simulations, temperature is controlled by the Berendsen thermostat with a coupling time equal to the value provided in next section “Simulation parameters”. Initially the chains are treated and rebuilt separately. For each individual chain the following MD steps are performed:

- 1) The nonbonded interactions are turned off (the parameters for the nonbonded interactions are set equal to zero) and a MD simulation with a very high bond constant ($1.0 \times 10^9 \text{ kJ} \cdot \text{mol}^{-1} \cdot \text{nm}^{-2}$) and small time step (0.00001 ps) is run for 100000 time steps.
- 2) The nonbonded interactions are then turned on and a simulation for 100000 time steps with a soft-core potential is carried out (time step is set to 0.00001 ps). The soft-core potential is implemented in

our simulation program YASP²⁵ in the following way: The short range part (0–d nm) of the nonbonded potential energy function is replaced by a cubic spline. The spline coefficients are chosen to satisfy four conditions: the spline matches the value (i) and the derivative (ii) of the original potential energy function at the crossover distance d; its derivative is zero at an interatomic distance r of zero (iii); most importantly, its value V_0 at $r=0$ is finite. In all cases the parameters for the soft core potential are set as $d=0.19$ nm and $V_0=15000$ kJ·mol⁻¹.

3) The value of V_0 is then increased to 50000 kJ·mol⁻¹ and the simulation with time step 0.00001 ps is run till temperature reaches its target value (between 100000 and 500000 time steps are required depending on the polymer).

4) The full nonbonded force field parameters are restored, the soft-core potential is turned off, and the system is initially equilibrated for 500000 time steps.

The previous steps are necessary to rebuild a single atomistic chain from the different fragments inserted in the RW path. During the MD simulations, periodic boundary conditions are applied, but the geometric center of the atomistic fragments and the corresponding ones belonging to the RW segments are restrained in their positions. This means that only the local structure (bending and dihedral angles) is modified during the procedure. After that, all chains (still restrained to their parent RW) are placed in a simulation box of size corresponding to the target density (say 0.75 g/cm³ for PE) and, in order to remove possible overlaps between their atoms, the following steps are necessary:

5) A soft-core ($d=0.19$ nm and $V_0=1000$ kJ·mol⁻¹) simulation is run for 100000 time steps with a time step of 0.0001 ps; V_0 is then increased to 20000 kJ·mol⁻¹ and the simulation is carried on till the temperature reaches the target value. The bond constants are still set to a very high value (1.0×10^7 kJ·mol⁻¹·nm⁻²) to maintain the topology of the chain.

6) The full nonbonded potential is restored and a simulation is run for 500000 time steps.

7) Finally, all restraints applied on the center of the segments are relieved and another MD simulation is run for 100000 time steps, initially with a time step of 0.00001 ps and then with a time step of 0.0001 ps.

At this point, harmonic bonds are replaced by bond constants if required in the final force field. All previous steps are run at constant volume. Now the system can be simulated in NPT and the normal simulation parameters (see next section “Simulation parameters”) can be used. As an example the rebuilt structure of one chain of PA-66 can be seen in Figure 6.1c.

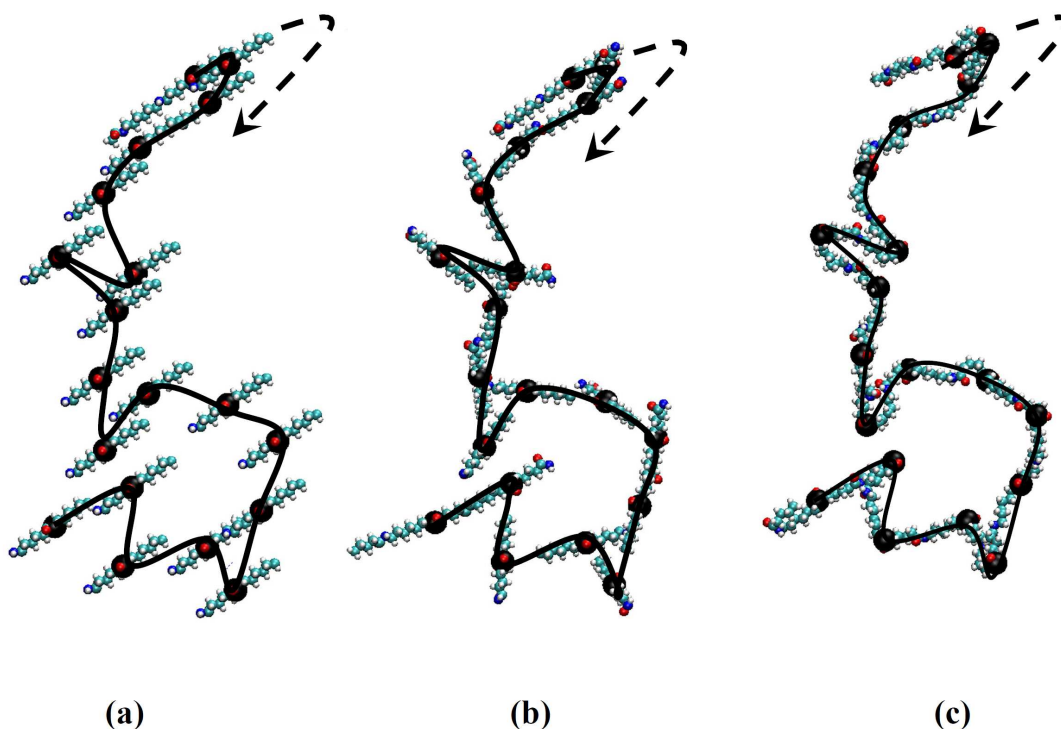


Figure 6.1. Steps of the reverse-mapping procedure (the case of PA-66 is reported): (a) insertion of the atomistic fragments (colored beads) on the parent random walk (solid black line); (b) orientation of the atomistic fragments; (c) final configuration of the rebuilt atomistic model. The arrow indicates the direction of the growing chain.

6.2.3. Simulation Parameters

Here the simulation details for the three polymers studied are briefly summarized. A more exhaustive description of the MD simulations can be found in the appropriate references reported below.

Polyethylene. The united-atom force field used both during the reverse-mapping steps and the MD runs is the one reported by Smit.²⁶ During the NPT simulations the cutoff radius is set to 1.0 nm; the temperature (450K) and the isotropic pressure (1 atm) are kept constant by the Berendsen thermostat (with a coupling time of 0.2 ps) and barostat (with coupling time of 5 ps).²⁷ The bond constraints are maintained to a relative tolerance of 10^{-6} by the SHAKE procedure.²⁸ A timestep of 2 fs is used. The length of the production run ranges between 2 and 14 ns depending on the molecular weight (M_w).

Polystyrene. The all-atom force field used during the reverse-mapping steps and the MD runs is the one reported in refs.²⁹ and ³⁰. During the NPT simulations the cutoff radius is set to 1.0 nm; temperature (500K) and isotropic pressure (1 atm) are kept constant by Berendsen thermostat (with a

coupling time of 0.2 ps) and by Berendsen barostat (with coupling time of 2.0 ps). The simulations are carried out with flexible bonds and a timestep of 2 fs. The production run is 8 ns for the highest M_w .

Polyamide-66. The all-atom force field parameters used can be found in ref.¹⁴ Temperature (550K) and pressure (1 atm) were controlled using the Berendsen algorithm with coupling time of 0.2 ps and 5 ps respectively. The equation of motion is integrated with a time step of 2 fs. The cutoff radius is to 0.9 nm, and a Verlet neighbor list with a pair cutoff of 1.0 nm is used, and updated by a link-cell scheme every 30 steps. Bond constraints are maintained to a relative tolerance of 10^{-6} by the SHAKE procedure. The length of the simulation is 2 ns.

6.3. Results and Discussion

6.3.1. Polyethylene

Seven different molecular weights of linear monodisperse PE are simulated (see Table 6.1). For the creation of the CRW the Kuhn length is set equal to 1.9 nm, a value close to the experimental one.³¹ During the reverse-mapping procedure each segment of the random walk (RW) is replaced by eight PE monomers. The inserting fragment has all the backbone dihedrals (φ) in the *trans* conformation ($\varphi=180^\circ$). For each molecular weight studied the chains are placed in a simulation box that reproduced the same average density of 0.75 g/cm^3 . After the reverse-mapping, the atomistic models are subjected to MD simulations at constant pressure (1 bar).

Table 6.1. Details of the polyethylene systems under investigation.

Number of chains in the simulation box	Number of Kuhn segments per chain	Number of carbons per chain (N)	Total number of monomers in the box	$\langle R_e^2 \rangle$ (\AA^2)	$\langle R_g^2 \rangle$ (\AA^2)
15	40	640	4800	14678.5 \pm 428.8	2849.3 \pm 46.8
20	30	480	4800	8688.0 \pm 267.3	1679.9 \pm 36.9
30	20	320	4800	5828.0 \pm 171.6	1324.1 \pm 25.8
40	10	160	3200	3103.1 \pm 72.9	570.4 \pm 9.3
50	5	80	2000	1545.6 \pm 33.7	277.2 \pm 3.9
60	3	48	1440	871.0 \pm 17.1	148.4 \pm 1.8
70	2	32	1120	523.1 \pm 8.4	84.1 \pm 0.8

The densities (reported as their reciprocal values) corresponding to the different molecular weights are shown in Figure 6.2 and compared with the experimental data. The overestimation of the density calculated from the simulations (for the percentage errors see inset of Figure 6.2) is probably due to the atomistic force parameters that, as it has been verified,⁸ are not very accurate in describing the volumetric properties and usually overestimate the density by ca. 3%. More importantly, the figure shows that, as expected for a polymer melt, the density values increases as the M_w increases until reaching a plateau for chain length exceeding 200 monomers. This trend in the density is caused by the reduced effect of the free volume of the chain ends when the molecular weight increases. The data can be fitted with the following equation

$$v = v_{\infty} + \frac{v_0}{M_w} \quad (6-1)$$

where v_{∞} is the value of the specific volume (v) at infinite chain length and v_0 is a proportionality constant, describing the rate with which v changes with increasing M_w . Fitting the simulation data, v_{∞} turns out to be equal to $1.270 \text{ cm}^3/\text{g}$ and $v_0 = 45.272 \text{ cm}^3/\text{mol}$; these numbers are in good agreement with the corresponding experimental results $v_{\infty} = 1.302 \text{ cm}^3/\text{g}$ and $v_0 = 41.551 \text{ cm}^3/\text{mol}$.³² The correct prediction of the trend of the density values with the polymer M_w shows that the fine-graining procedure is able to equilibrate the long-range thermodynamic properties of entangled and unentangled PE chains.

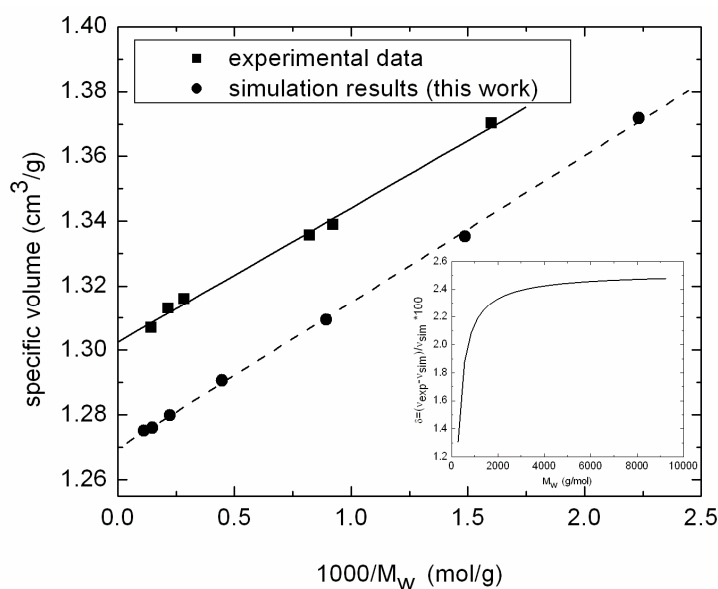


Figure 6.2. Dependence of the specific volume (v) on inverse of the molecular weight (M_w) as predicted by this work and as measured experimentally.⁸ The straight and the dashed lines show the fitted linear functions to the predicted and experimental points according to eq 6.1 in the text. The inset shows in percentage the error between the experimental and the simulated values.

In order to analyse the local and global structural properties of the chains, the distribution of the backbone dihedral angles (averaged over the chains and the trajectories) and the X-ray structure factor (Figure 6.3) are calculated. The probability of encountering a dihedral angle in *trans* conformation in the PE sample is $P_t=0.647$ in perfect agreement with that found by Spyriouni et al.³³ calculated for PE (C_{16}) simulated using MC at the same temperature ($T=450K$) using the force field reported in ref.³⁴ ($P_t=0.652$). This agreement shows that, even though the initial conformation of the inserted unit was set to be only *trans*, during the equilibration step the correct dihedral distribution is reached.

The partial structure factor can be calculated through the formula³⁵

$$S_{\alpha\beta}(k) = \delta_{\alpha\beta} + 4\pi\sqrt{\rho_\alpha\rho_\beta} \int_0^b r^2 [g_{\alpha\beta}(r) - 1] \frac{\sin(kr)}{(kr)} dr \quad (6-2)$$

where $\rho_\alpha = \frac{N_\alpha}{V}$ is the number density of atoms of type α , $g_{\alpha\beta}(r)$ is the radial distribution function among the atoms α and β , $\delta_{\alpha\beta}$ is the Dirac delta function and b (the upper limit of the integral) is half of the simulation box length. The total X-ray structure factor is given by equation (3):

$$S(k) = \sum_\alpha \sum_\beta C_\alpha C_\beta \frac{f_\alpha(k) f_\beta(k)}{\langle f(k) \rangle^2} S_{\alpha\beta}(k) \quad (6-3)$$

where C_α is the concentration of α atoms, f_α are the atomic form factors, and $\langle f(k) \rangle = \sum_\alpha C_\alpha f_\alpha(k)$.

It must be noticed that for the PE, since the atomistic force field used is a united force field, there is only one type of particle and $\alpha \equiv \beta$. Figure 6.3 shows an excellent agreement between the simulated and the experimental patterns and all the peaks both at low (corresponding to the intermolecular correlations) and at high (representing the intramolecular correlations) values of k are perfectly reproduced by the simulations. To assess the good equilibration of the polymer chain at intermediate length scale the mean square internal distances (MSID) are calculated for the PE samples.³⁶ The inset of Figure 6.3 shows that the PE displays the Gaussian behavior as the MSID tends asymptotically to a constant value as N increases. Ahul et al.³⁶ pointed out that the MSID is a useful way to check whether deformations on the short and intermediate length scales take place in the polymer chain. They identified the causes of such deformations in both the fast introduction of the excluded volume interactions and the inhomogeneous distribution of the density in the initial simulation box. In the present case the gradual introduction of the excluded volume interactions (spread over 1.5 ns) may have helped in overcoming the problem of the initial inhomogeneous distribution density and no evident deformations of the chain are visible.

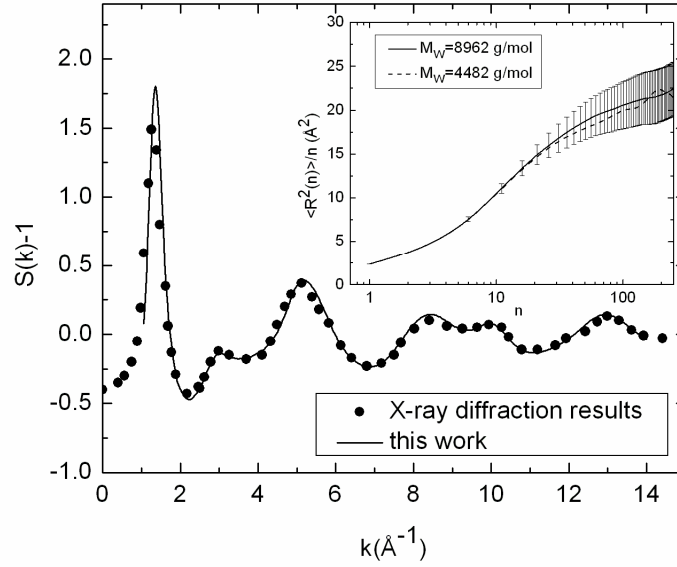


Figure 6.3. X-ray diffraction patterns of polyethylene from the simulation ($T=450$ K, $M_w=8960$ g/mol) and experiment⁵² ($T=430$ K, $M_w=8806$ g/mol) at $P=1$ atm. The inset shows the mean squared internal distances for PE of chain length $N=640$ ($M_w=8962$ g/mol) and $N=320$ ($M_w=4482$ g/mol). The error bars correspond to the highest M_w .

Another important quantity to check in order to verify the ability of the fine-graining procedure to equilibrate polymer melts is the variation of the single chain conformational properties with the M_w . Figure 6.4 shows the values of the end-to-end distance ($\langle R_e \rangle$) and gyration radius ($\langle R_g \rangle$) for different M_w s (values reported also in Table 6.1). The results are compared with those obtained for PE of similar M_w s equilibrated using the end-bridging MC (simulated at 450 K). The comparison is made even more interesting by the fact that for some samples the end-bridging MC and the fine-graining technique use the same force field reported by Smit.²⁶ The agreement between these data is impressive and it represents a major proof of the good equilibration achievable with the fine-graining method. The two sets of data follow the statistics of the ideal chains where $\langle R_g \rangle = \langle R_e \rangle / 6$ and $\langle R_e \rangle \approx N^\nu$, and the Flory exponent ν is $\nu = 0.5$ (the straight line through the symbols in Figure 6.4). From the value of $\langle R_e \rangle$ the characteristic ratio C_n can be calculated through the formula

$$C_n = \langle R_e^2 \rangle / (n-1)l^2 \quad (6-4)$$

where n is the number of backbone bonds and l their averaged bond length (in this case 1.54 Å). For long chains C_n converges to a single value usually known as C_∞ . The C_∞ can be then directly estimated from the slope of the line fitting $\langle R_e^2 \rangle$ versus $(n-1)l^2$. The C_∞ obtained in such way turns out

to be 8.75, value that is in good agreement with that obtained from the end-bridging MC method⁸ using the force field developed by Mavrantzas and Theodorou³⁷ ($C_\infty = 9.13$) and with the value obtained more recently using the TRAPPE force field ($C_\infty = 8.26$).³⁸ The computed value agrees quite well with recent experimental measurements which for molten PE yield $C_\infty = 7.8$.^{39, 40} The small overestimation made by the simulation is caused by the atomistic force employed that slightly overestimates the *trans* population of the dihedral angles along the PE chain.⁹

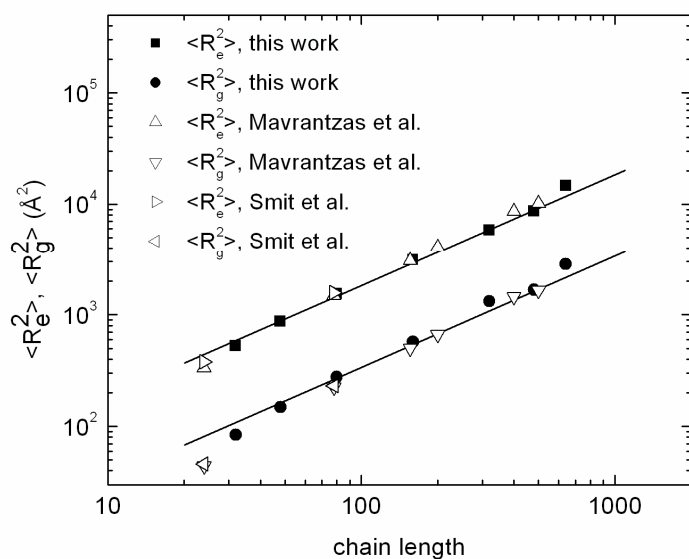


Figure 6.4. Mean-square end-to-end distance ($\langle R_e^2 \rangle$) and gyration radius ($\langle R_g^2 \rangle$) of polyethylene as function of the number of backbone atoms (N) in logarithmic scale. The results obtained from the fine-graining technique using the Smit force field²⁶ (“this work” in the legend) are compared with those obtained with end-bridging MC using the force fields reported in ref.³⁷ (“Mavrantzas et al.” in the legend) and in ref.²⁶ (“Smit et al.” in the legend). The straight lines represent the Flory predictions for $\langle R_e^2 \rangle$ and $\langle R_g^2 \rangle$ ($\langle R_e \rangle$ and $\langle R_g \rangle \approx N^{0.5}$). Error bars are at the size of the symbols.

Table 6.2. Details of the polystyrene systems under investigation.

Number of chains in the simulation box	Number of Kuhn segments per chain	Number of backbone’s carbons per chain (N)	Number of monomers per chain	$\langle R_e^2 \rangle$ (\AA^2)	$\langle R_g^2 \rangle$ (\AA^2)
15	10	160	80	3811.1 ± 139.7	677.1 ± 17.9
11	13	208	104	3707.6 ± 93.1	783.3 ± 14.1
8	19	304	152	9563.9 ± 220.7	1737.9 ± 38.5

6.3.2. Atactic-Polystyrene

The fine-graining procedure turns out to be a very effective and easy technique to equilibrate long PE chain. However, PE is topologically the simplest example of a polymer chain since, if an UA force field is used, the chain is made up only by spherical particles of the same van-der-Waals radius (except the first and the last monomers). On the contrary, PS shows a more complicated topology, first because of the steric pendant groups (the phenyl rings) attached to the backbone chain, second the methine carbons of the backbone are asymmetric and their relative chirality defines the tacticity of the polymer chains. Moreover, the PS chain is characterized by a long range correlation among the bonds (high Kuhn length value) and consequently a higher stiffness. Therefore it is worth to verify the effectiveness of the fine-graining procedure also in cases where the conformation of the inserting atomic moiety is not straightforward determined, more conformational states can be populated, and the stiffness of the chain is enhanced.

The Kuhn length for atactic PS is set to 2.0 nm⁴¹ corresponding to roughly 8 monomers when the backbone dihedral angles are all in the *trans* conformation. Three different M_ws have been studied (see Table 6.2) all below the experimental entanglement molecular weight (16600 g/mol)³¹ that corresponds to roughly 320 backbone carbons; during the reverse-mapping steps atomistic segments, characterized each by a randomly different tacticity, are inserted in the RW monomers.

In literature different coarse-grained models of a-PS have been proposed with the aim of studying long range structural and dynamic properties.^{16, 42, 43} The models differ in the number of degrees of freedom retained and in the procedure for developing the effective interactions between the coarse-grained beads. Figure 6.5 shows the values for $\langle R_e \rangle$ and $\langle R_g \rangle$ obtained from the fine-graining procedure compared with the numbers reported for coarse-grained models of PS of similar M_ws. The change in the structural parameters with increasing the M_w is similar in all the models. It must be noticed anyway that the lower M_w models of this work (N=160 and N=208) show a moderate increase in $\langle R_g \rangle$ when the M_w increases and similar (considering the error) value of $\langle R_e \rangle$. A more conventional behavior is shown by the highest M_w (N=308) where both $\langle R_g \rangle$ and $\langle R_e \rangle$ have higher values than the corresponding ones calculated for lower M_ws. Anyway, it is worth to notice that for low M_ws, a direct comparison between the absolute values of $\langle R_g \rangle$ and $\langle R_e \rangle$ obtained with the fine-graining method and the other models reported in literature can be done only in a qualitative way since a coarser model gives a rougher description of the molecular shape.

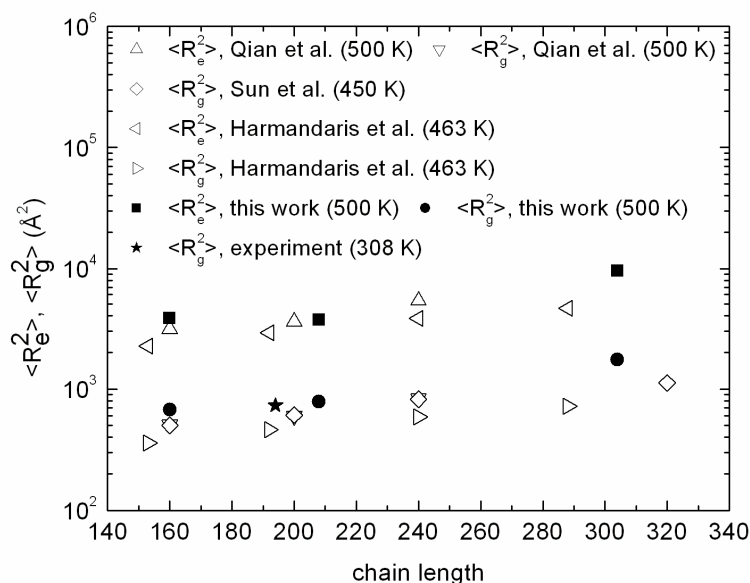


Figure 6.5. Mean-square end-to-end distance, $\langle R_e^2 \rangle$, and radius of gyration, $\langle R_g^2 \rangle$ of atactic polystyrene as a function of chain length N ($T=500$ K). Error bars are at the size of the symbols. The results obtained from the fine-graining technique are compared with those obtained from the coarse-grained simulations of Qian et al.³⁰ ($T=500$ K), Sun and Faller¹⁶, ($T=450$ K) and Harmandaris and Kremer²¹ ($T=463$ K). The experimental value obtained from small-angle X-ray scattering in θ solution at $T=308$ is also reported.⁵³

The good long range relaxation of the PS melt can be verified comparing the X-ray spectrum calculated using eqs 6.2 and 6.3 with the experimental pattern (Figure 6.6). There are indeed substantial differences between the coherent scattering functions, $S(k)$, of the various polymers. For all polymers the "amorphous halo" is the prominent peak which occurs at $k < 2.0 \text{ \AA}^{-1}$, and this feature is observed to change in shape and position depending on the polymer. For example, this peak is narrow and symmetric for PE (Figure 6.3) while for PS it shows two features: the main peak (1.5 \AA^{-1}) is of breadth similar to, and position slightly higher than, that of PE; moreover a small pre-peak, located at lower k (0.75 \AA^{-1}) (know as "polymerization peak") is also clearly visible. Figures 6.3 and 6.6 show that even though the long length-scale equilibration has been performed simply by creating RWs characterized by different Kuhn lengths, after the reverse-mapping scheme the simulated X-ray shows the correct low- k peaks characteristic of different polymers. The MSID analysis for two M_w s of the PS samples is reported in the inset of Figure 6.6. Here, due to the small M_w s the asymptotic behavior showed by PE cannot be seen. In order to check possible deformations of the polymer chains, the analysis is made on two M_w s ($N=160$ and $N=304$). The two curves show a similar behavior at short and intermediate length scales independent of the total chain length (N) and there is not evident stretch of the chain for $N < 30$. Other simulations will be carried on in order to investigate the behavior of the

chain as the M_w further increases. Another important analysis that can be done on polystyrene is to study the relative backbone-backbone or phenyl-phenyl positions in the simulation box. A convenient way is to compare the partial X-ray structure factors with the ones calculated from previous simulations reported by Ayyagari et al.⁴⁴ that, by means of MD simulations, calculated the intra- and inter-molecular contributions to the X-ray structure factor in order to clarify the interactions responsible for the presence of two peaks in the “amorphous halo” region and their temperature-dependence position. Figure 6.7 shows the Kratky plot of the individual contributions as well as the total $S(k)$ for a-PS at 500 K as obtained after the fine-graining procedure. The agreement with the results found by Ayyagari (not shown in the figure) is remarkable: the phenyl-phenyl and phenyl-backbone correlations turn out to be responsible for the presence of the high- k peak, while the low- k peak is due mainly to the backbone-backbone contributions. This perfect agreement among the total and partial X-ray spectra leads to the important conclusion that the a-PS melt is well equilibrated at different length scales and that the relative positions of the atoms belonging to the backbone atoms and to the pendant group is correct.

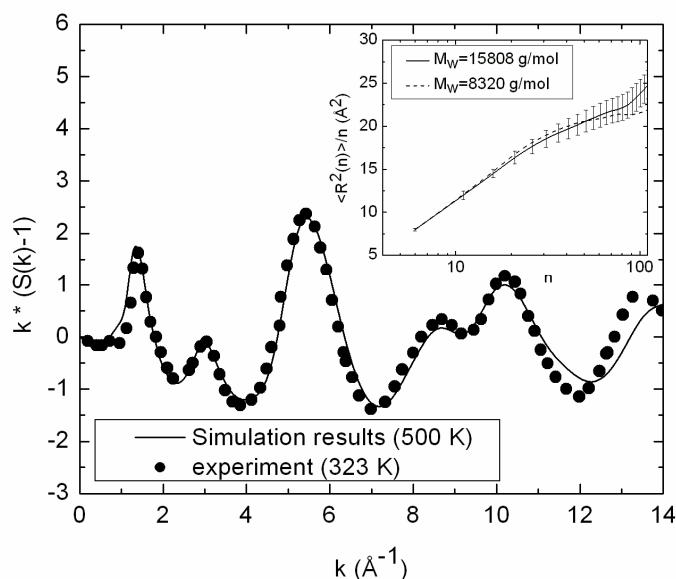


Figure 6.6. The k -weighted total structure factor of atactic polystyrene from the simulation ($N=160$) and experiment ($N=16$).⁵⁴ The inset shows the the mean squared internal distances for polystyrene chain of length $N=304$ ($M_w=15808$ g/mol) and $N=160$ ($M_w=8320$ g/mol). The error bars correspond to the highest M_w .

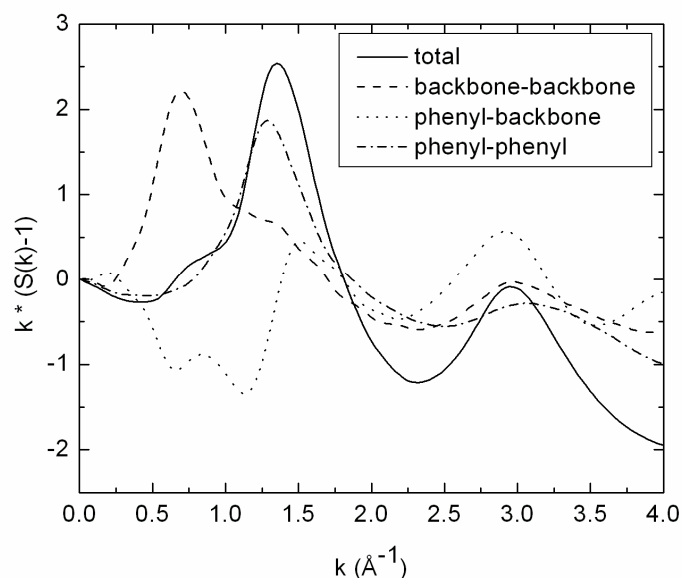


Figure 6.7. Kratky plot of the contribution of phenyl-phenyl, phenyl-backbone and backbone-backbone correlations to the X-ray structure factor of polystyrene ($N=160$) at 500 K.

To analyze the equilibration of the chain at shorter length-scale the orientation distribution functions describing the mutual orientation of aromatic rings is calculated. A convenient measure is the cosine of the angle between the plane normals \mathbf{u} of two rings. In order not to distinguish between two symmetrically equivalent orientations (one ring turned by 180°), the absolute value of the scalar product $|\mathbf{u} \cdot \mathbf{u}|$ is used. This is 1 for two coplanar rings, 0 for a T-shaped arrangement, and $1/2$ for a random distribution of orientations. In Figure 6.8, this orientational distribution function (ODF) as a function of the average distance between the pair of rings is reported. At a short distance (less than 0.5 nm) the phenyl rings are predominantly coplanar, while for larger distance the co-planarity is quickly lost and no further specific orientation can be seen. This result agrees with that found in previous atomistic simulations of a-PS bulk simulated with the same force field.²⁹

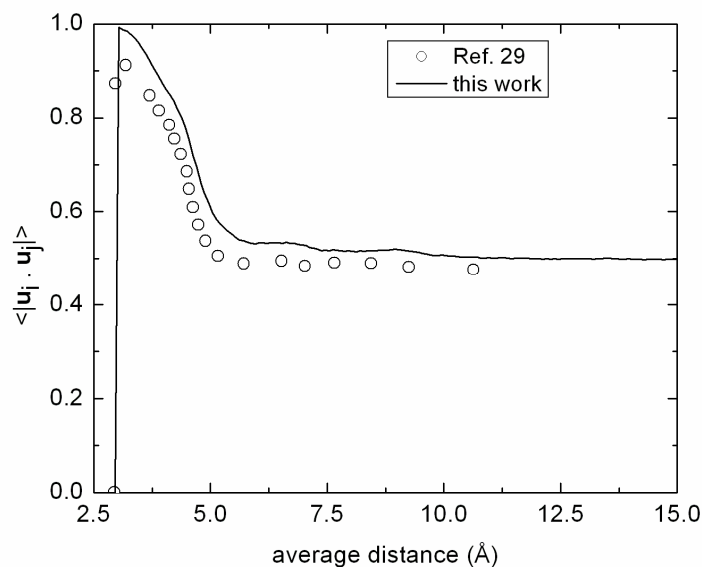


Figure 6.8. Comparison between the orientation distribution function describing the mutual orientation of the plane normals of phenyl rings calculated for a-PS with $N=160$ (“this work”) and from ref.²⁹.

To study the local relaxation the dihedral distribution of the backbone angles is calculated from the simulations (see Table 6.3). From NMR measurements on a-PS, Dunbar⁴⁵ estimated an amount of dihedral angles in the *trans* (*t*) conformation of around 68 ± 10 % at room temperature. The result obtained for the PS with $N=160$ for the overall *trans* content is in agreement with the experimental result, but the nearly symmetric distribution obtained for *g* (most favourable conformation) and *g'* (highly unfavoured conformation since responsible for the so called “pentane effect”) is probably caused by the steric hindrance of the pendant rings that locks the model in a unfavourable conformations. To avoid this problem, longer MD simulations after the reverse-mapping steps are probably necessary to relax completely the local structure. It must be noticed anyway that very similar distribution has been obtained from standard MD atomistic simulations carried out on ten monomers of a-PS using the same atomistic force field employed here.³⁰ The simulations predicted around 60% for the *trans* conformation, 21% for the *g* and 19% for the *g'* state. This can suggest that the reason for the fact that the *g* and *g'* conformations are similarly populated stems on the force field used more than on the equilibration procedure. Another important analysis that can be done in order to check the correct local conformation is the distribution of two successive backbone dihedrals. Considerable deviations may occur between the distributions gained interpreting NMR data⁴⁶ and the predictions obtained from the atomistic simulations. Robyr et al.⁴⁷ were able to reproduce the realistic a-PS chain conformations using a modified RIS model but the correct reproduction of the dyad conformations from simulations is still far to be achieved even using sophisticated procedures to equilibrate the chain.^{17, 48} The dyad

distribution obtained from the fine-graining procedure is also not in perfect agreement with the experimental findings, but the results are anyway encouraging. The NMR experiments⁴⁶ show that at least 50% of the racemo dyads are close to the *tt* state, and more than 8% is in the *tg'/g't* conformations, while in the case of meso dyads a large amount of dihedrals are near the *tg/gt* conformations (>80%) and a small amount (<10%) near the *tt* state. For the racemic dyad the simulations predict 71 % of *tt* and 7.6% in the *tg'/g't* while 19% of *tt* and 40% of *tg/gt* conformations are found for the meso dyad. The discrepancy between the simulations and the experimental finding for the meso dyad (underestimation of the amount of the *tg/gt* conformations and the overestimation of the *tt* conformers) is remarkably similar to that reported by Mulder et al.⁴⁸ (19.8 % of *tt* and 64.9% of *tg/gt*) and Spyriouni et al.¹⁷ (60% *gt/tg*) which used an atomistic force field different than the one used in this paper. However, further investigations will be carried out to verify the atomistic force field used here and to monitor changes in the torsion distribution when longer MD simulations are performed.

Table 6.3. Overall dihedral distribution and dyad conformations calculated at 500 K for atactic polystyrene. All molecular weights studied show similar probabilities.

	States	Probability %
Overall distribution	t	67
	g	17
	g'	16
Meso dyad	tt	19.0
	tg/gt	40.4
	gg	1.0
	g'g/g g'	1.7
	t g' / g't	38.1
	g'g'	0
	Racemic dyad	tt
	tg/gt	7.6
	gg	6.5
	g'g/g g'	2.3
	t g' / g't	7.6
	g'g'	4.5

Table 6.4. Comparison between the results obtained from the fine-graining procedure (“this work”) after 2 ns of MD of 12 chains and the ones obtained using the pivot MC method (PMC) after 20 ns of MD of 24 chains of polyamide-66 at 550 K.

	This work	PMC
Density (kg/m ³)	986.3 ± 3.2	981.0 ± 1.5
$\langle R_e^2 \rangle$ (Å ²)	4422.4 ± 176.3	4699.4 ± 164.2
$\langle R_g^2 \rangle$ (Å ²)	872.8 ± 18.3	935.0 ± 19.0
Fraction of hydrogen-bonds *	0.49 ± 0.01	0.49 ± 0.02

* The hydrogen bonds are defined according to a geometrical criterion stating that the distance between the hydrogen of the donor group and the acceptor O has to be <0.297 nm and the donor-hydrogen-acceptor angle > 130.²⁰ The “fraction of hydrogen bond” corresponds to the fraction of amide groups hydrogen bonded.

6.3.3. Polyamide-66

The last polymer on which the fine-graining technique is tested belongs to the family of the polyamides where a widespread hydrogen bond network connecting the amide groups dominates their properties even at high temperature. Moreover, the experimental value of the Kuhn length is not available. Therefore the l_k value ($l_k=1.8$ nm) obtained from previous atomistic simulations¹⁴ is used to prepare the RWs. In this case each RW segment is repopulated with 22 backbone atoms (including four amide groups), corresponding to one and half monomers (NHCO-(CH₂)₄-CONH-(CH₂)₆-NHCO-(CH₂)₄-CONH) with all the backbone dihedral angles in the *trans* conformation. Due to the lack of experimental data, the simulation results are compared with previous MD simulations¹⁴ run with the same force field employed here; moreover at the moment the simulations will be restricted only to one M_w ($M_w=4540$ g/mol) barely behind the critical mass reported in literature as 4700 g/mol⁴⁹ above which entanglements start to be formed. In ref.¹⁴ the PA-66 melt has been equilibrated using the pivot MC method (PMC) of Neyertz and Brown¹³ using $n_{\text{bonds}}=4$ (backbone bonds) implying that two neighboring amide groups do not interact with each other. Once that the single chains have been generated using the PMC algorithm, the procedure followed to equilibrate the melt is very similar to that followed in this paper: the chains are submitted to periodic boundary condition and the full intermolecular interactions have been introduced gradually. Table 6.4 compares the values of several properties as obtained from the fine-graining and from the PMC technique. The density and, most importantly, the averaged (on the trajectory and the polymer chains) number of hydrogen bonds are in

perfect agreement; the single chain property, $\langle R_e \rangle$, also matches ($\langle R_e \rangle = 68.5 \pm 12.8 \text{ \AA}$ from the PMC and $\langle R_e \rangle = 66.5 \pm 13.3 \text{ \AA}$ from the fine-graining). Both results are in reasonable agreement with the experimentally available value, obtained for a θ solution, estimated as $61 \pm 6 \text{ \AA}$ for 4500 g/mol chains.⁵⁰

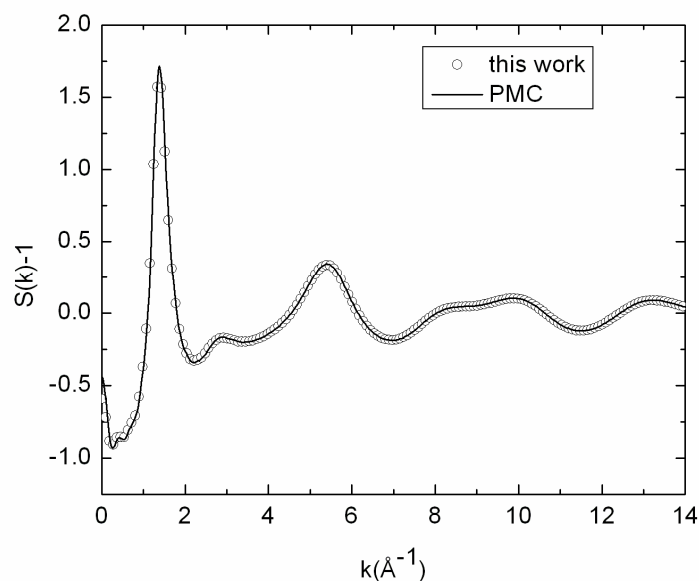


Figure 6.9. Total structure factor of polyamide-66 chains with 20 monomers per chain. Comparison between the results obtained using the fine-graining technique (“this work”) for 12 chains and the pivot MC (“PMC”) method for 24 chains followed by MD relaxation. Both simulations use the same force field and temperature ($T=550 \text{ K}$).

The overall good relaxation of the melt can be seen in Figure 6.9 that compares the $S(k)$ calculated from eqs 6.2 and 6.3 obtained from the fine-graining technique and from the PMC after 2 ns of MD simulations. Both the “amorphous halo”, at $k < 0.2 \text{ nm}^{-1}$, and the high- k peaks show the same spacing. Since the presence of hydrogen bonds between amide groups determines most of the conformational properties of PA-66 even at high temperature, it is interesting to analyze the distribution of these functional groups within the simulation box in more detail. Figure 6.10 shows the inter-molecular radial distribution functions (RDF) of the carbonyl carbon atoms and compares the results obtained using the PMC and the fine-graining methods. The first peak (at $\sim 0.5 \text{ nm}$) of the RDF corresponds to the averaged inter-chain spacing between two carbonyl groups and it is related to the presence of the intermolecular hydrogen bonds connecting the amide groups. The PMC and the fine-graining methods reproduce the same distribution and the perfect overlap among the peaks confirms the agreement between the values of the fraction of hydrogen bonds reported in Table 6.4. The last analysis concerns the conformation of the single chain investigated looking at the intramolecular RDF

between the carbonyl carbons (Figure 6.11). The RDF presents two peaks centered at 0.6 and 0.9 nm. In order to understand their molecular origin, the distribution of the distance among the carbonyl carbons within the chain is calculated and reported in the inset of Figure 6.11. This distribution considers only the distance among subsequent carbonyl carbons. The distribution is double peaked and the peaks lay at the same spacing as the RDF ones. Thus, it is evident that the first peak of the RDF at ~ 0.6 nm corresponds to the carbonyl carbon pairs separated by four methylenic carbons, while the second one (at ~ 0.9 nm) is mainly due to the carbons separated by six methylenic groups. Also in this case the PMC and the fine-graining technique show that even at short length scale the PA-66 chains equilibrated with the MC approach and the fine-graining one have adopted the same local conformations.

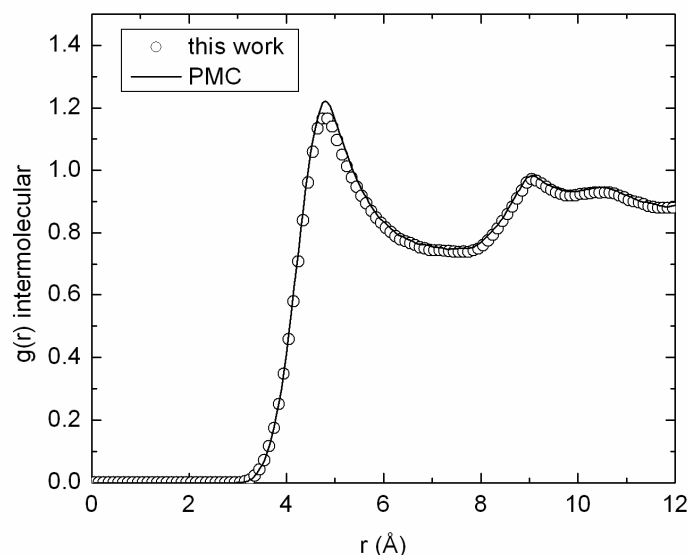


Figure 6.10. Intermolecular radial distribution functions calculated among the carbonyl carbons of the polyamide-66 chains with 20 monomers per chain. The comparison between the results obtained using the fine-graining technique (“this work”) and the pivot MC (“PMC”) method is shown. (T=550 K)

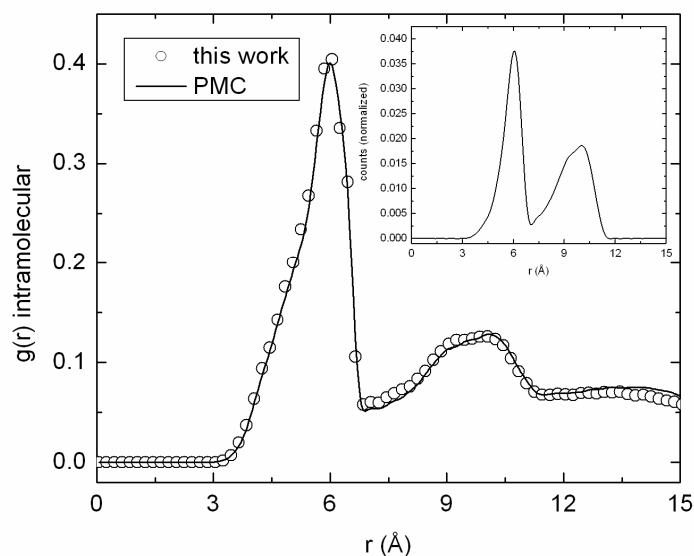


Figure 6.11. Intramolecular radial distribution function of the carbonyl carbons of the polyamide-66 chains with 20 monomers per chain. The comparison between the results obtained using the fine-graining technique (“this work”) and the pivot MC (“PMC”) method followed by MD relaxation is shown ($T=550$ K). The inset is the distribution of distance between subsequent carbonyl carbon.

6.4. Conclusions

A technique to relax high M_w polymer melts has been proposed. The method, named fine-graining, acts on two different length scales to equilibrate the melt: at the long length scale the chains are described as a random walk whose Kuhn length is chosen depending on the polymer under study. Then, following the parent random walk, the atomistic details are introduced by replacing the RW segments with the corresponding atomistic fragments of the appropriate number of monomers. At the short length scale the equilibration consists of a simple procedure involving a series of MD simulations. A similar approach has been used by Kotelyanskii et al.⁵¹ where lattice self-avoiding random-walks are generated to completely occupy a cubic lattice. The random walks are then decorated assigning to each lattice site a specific building block (of size smaller than a monomer). The rebuilt atomistic structure is then annealed and equilibrated. The fundamental difference among the fine-graining and the procedure proposed by Kotelyanskii is that the fine-graining exploits the “Flory ideality hypothesis” generating a non-self avoiding random walk and re-introducing the atoms at a length-scale equal to the Kuhn length. Anyway it is worth to notice that the reverse mapping procedure presented here is not unique and others may be tried.

The technique has been successfully applied to equilibrate three different polymers (polyethylene, atactic polystyrene and polyamide-66) characterized by different molecular weight, chain flexibility

(Kuhn length value), chemistry and topology. The method has proved to be very competitive due mainly to its easy implementation. In particular, the perfect agreement between structural properties (computed at different length-scale) obtained with the fine-graining procedure and other methods (i.e. end-bridging MC or PMC) but simulated with the same simulation details (force field, M_w of the polymers), is very impressive, and it gives a clear proof of the reliability of the fine-graining method.

In the future some important aspects of the technique can be further investigated. First the choice of an accurate atomistic force field is probably a crucial point for the success of the procedure since the formation of the backbone bonds connecting the inserting atomistic fragments and the relaxation of the local conformations, rely on atomistic MD simulations. Moreover, from the results it turned out that the length of the final NPT MD trajectory is not a major concern for a flexible chain, such as for PE, where the correct dihedral distributions is obtained after a short MD run, but it may be a problem for a more rigid polymer such as PS. In the latter case indeed the presence of bulky pendant groups, may require long MD simulations with soft-core potential or an “ad hoc” choice of the internal conformation of the atomistic fragment to relax properly the local structure. In the particular case of PS a possible improvement could also be the use of a fragment library containing polymer segments in different configurations or the reduction of the torsional barriers during the reverse mapping steps, together with the soft core potential, leading to a faster equilibration of the dihedral angles. Another point that may be of interest is the effect that a correct choice of the Kuhn length value has on the final results. This can be important especially in those cases where the experimental numbers are not available to check whether the Kuhn length available for polymers with similar chemistry could be used or if an accurate estimation of the value (from experiments or molecular simulations) is necessary.

6.5 References

- (1) B. J. Reynwar, G. Illya, V. A. Harmandaris, M. M. Müller, K. Kremer and M. Deserno, *Nature*, 2007, **447**, 461-464.
- (2) G. Srinivas, D. E. Discher and M. L. Klein, *Nat. Mater.*, 2004, **3**, 638-644.
- (3) R. Everaers, S. K. Sukumaran, G. S. Grest, C. Svaneborg, A. Sivasubramanian and K. Kremer, *Science*, 2004, **303**, 823-826.
- (4) J. J. Depablo, M. Laso and U. W. Suter, *J. Chem. Phys.*, 1992, **96**, 2395-2403.
- (5) J. I. Siepmann and D. Frenkel, *Mol. Phys.*, 1992, **75**, 59-70.
- (6) L. R. Dodd, T. D. Boone and D. N. Theodorou, *Mol. Phys.*, 1993, **78**, 961-996.
- (7) A. Uhlherr, *Macromolecules*, 2000, **33**, 1351-1360.
- (8) V. G. Mavrantzas, T. D. Boone, E. Zervopoulou and D. N. Theodorou, *Macromolecules*, 1999, **32**, 5072-5096.
- (9) N. C. Karayiannis, A. E. Giannousaki, V. G. Mavrantzas and D. N. Theodorou, *J. Chem. Phys.*, 2002, **117**, 5465-5479.
- (10) O. Alexiadis, V. G. Mavrantzas, R. Khare, J. Beckers and A. R. C. Baljon, *Macromolecules*, 2008, **41**, 987-996.
- (11) M. Doxastakis, V. G. Mavrantzas and D. N. Theodorou, *J. Chem. Phys.*, 2001, **115**, 11339-11351.
- (12) C. D. Wick and D. N. Theodorou, *Macromolecules*, 2004, **37**, 7026-7033.
- (13) S. Neyertz and D. Brown, *J. Chem. Phys.*, 2001, **115**, 708-717.
- (14) S. Goudeau, M. Charlot, C. Vergelati and F. Müller-Plathe, *Macromolecules*, 2004, **37**, 8072-8081.
- (15) S. Queyroy, S. Neyertz, D. Brown and F. Müller-Plathe, *Macromolecules*, 2004, **37**, 7338-7350.
- (16) Q. Sun and R. Faller, *Macromolecules*, 2006, **39**, 812-820.
- (17) T. Spyriouni, C. Tzoumanekas, D. Theodorou, F. Müller-Plathe and G. Milano, *Macromolecules*, 2007, **40**, 3876-3885.
- (18) P. Carbone, H. A. Karimi-Varzaneh, X. Y. Chen and F. Müller-Plathe, *J. Chem. Phys.*, 2008, **128**.
- (19) X. Y. Chen, P. Carbone, W. L. Cavalcanti, G. Milano and F. Mueller-Plathe, *Macromolecules*, 2007, **40**, 8087-8095.
- (20) H. A. Karimi-Varzaneh, P. Carbone and F. Müller-Plathe, *Macromolecules*, 2008, **41**.
- (21) V. A. Harmandaris and K. Kremer, *Macromolecules*, 2009, **ASAP • DOI: 10.1021/ma8018624**.
- (22) K. Kamio, K. Moorthi and D. N. Theodorou, *Macromolecules*, 2007, **40**, 710-722.
- (23) F. Müller-Plathe, *Chemphyschem*, 2002, **3**, 754-769.
- (24) M. Rubinstein and R. H. Colby, *Polymer Physics*, Oxford University Press, 2007.
- (25) F. Müller-Plathe, *Chemphyschem*, 1993, **78**, 77-94.
- (26) B. Smit, S. Karaborni and I. J. Siepmann, *J. Chem. Phys.*, 1995, **102**, 2126.
- (27) H. J. C. Berendsen, J. P. M. Postma, W. F. van Gusteren, A. Di Nola and J. R. Haak, *J. Chem. Phys.*, 1984, **81**, 3684.
- (28) J.-P. Ryckaert, G. Ciccotti and H. J. C. Berendsen, *J. Comput. Phys.*, 1977, **23**, 327.
- (29) F. MüllerPlathe, *Macromolecules*, 1996, **29**, 4782-4791.
- (30) H. J. Qian, P. Carbone, X. Y. Chen, H. A. Karimi-Varzaneh, C. C. Liew and F. Müller-Plathet, *Macromolecules*, 2008, **41**, 9919-9929.
- (31) J. E. Mark, Ed., *Physical Properties of Polymers Handbook*, Springer, 2007.
- (32) D. J. Kinning, E. L. Thomas and J. M. Ottino, *Macromolecules*, 1987, **20**, 1129-1133.

-
- (33) T. Spyriouni, I. G. Economou and D. N. Theodorou, *Macromolecules*, 1997, **30**, 4744-4755.
- (34) L. R. Dodd and D. N. Theodorou, *Adv. Pol. Sci.*, 1994, **116**, 249.
- (35) B. L. Bhargava, R. Devane, M. L. Klein and S. Balasubramanian, *Soft Matter*, 2007, **3**, 1395-1400.
- (36) R. Auhl, R. Everaers, G. S. Grest, K. Kremer and S. J. Plimpton, *J. Chem. Phys.*, 2003, **119**, 12718-12728.
- (37) V. G. Mavrantzas and D. N. Theodorou, *Macromolecules*, 1998, **31**, 6310-6332.
- (38) K. Foteinopoulou, N. C. Karayiannis, M. Laso and M. Kroeger, *Journal of Physical Chemistry B*, 2008, **to appear**.
- (39) J. C. Horton, G. L. Squires, A. T. Boothroyd, L. J. Fetters, A. R. Rennie, C. J. Glinka and R. A. Robinson, *Macromolecules*, 1989, **22**, 681-686.
- (40) L. J. Fetters, W. W. Graessley, R. Krishnamoorti and D. J. Lohse, *Macromolecules*, 1997, **30**, 4973-4977.
- (41) J. P. Cotton, D. Decker, H. Benoit, B. Farnoux, J. Higgins, G. Jannink, R. Ober, C. Picot and Cloizeau, *Macromolecules*, 1974, **7**, 863-872.
- (42) V. A. Harmandaris, N. P. Adhikari, N. F. A. van der Vegt and K. Kremer, *Macromolecules*, 2006, **39**, 6708-6719.
- (43) G. Milano and F. Müller-Plathe, *J. Phys. Chem. B*, 2005, **109**, 18609-18619.
- (44) C. Ayyagari, D. Bedrov and G. D. Smith, *Macromolecules*, 2000, **33**, 6194-6199.
- (45) M. G. Dunbar, B. M. Novak and K. Schmidt-Rohr, *Solid State Nucl. Magn. Reson.*, 1998, **12**, 119-137.
- (46) P. Robyr, Z. Gan and U. W. Suter, *Macromolecules*, 1998, **31**, 8918-8923.
- (47) P. Robyr, M. Müller and U. W. Suter, *Macromolecules*, 1999, **32**, 8681-8684.
- (48) T. Mulder, V. A. Harmandaris, A. V. Lyulin, N. F. A. van der Vegt, K. Kremer and M. A. J. Michels, *Macromolecules*, 2009, **42**, 384-391.
- (49) Y.-H. Zang and P. J. Carreau, *J. Appl. Pol. Sci.*, 1991, **42**, 1965.
- (50) B. D. Viers, *Nylon 66. In Polymer Data Handbook*, Oxford University Press, New York, 1999.
- (51) M. Kotelyanskii, N. J. Wagner and M. E. Paulaitis, *Macromolecules*, 1996, **29**, 8497-8506.
- (52) G. H. Kevin, D. M. John, G. C. John, S. S. Kenneth, H. N. Alfred and H. Anton, *J. Chem. Phys.*, 1991, **94**, 4659-4662.
- (53) T. Konishi, T. Yoshizaki, T. Saito, Y. Einaga and H. Yamakawa, *Macromolecules*, 1990, **23**, 290-297.
- (54) Londono, J. D.; Habenschuss, A.; Curro, J. G.; Rajasekaran, J. J. *J. Polym. Sci., Part B: Polym. Phys.*, **1996**, **34**, 3055

7. Outlook

This PhD thesis deals with the several developments and their applications in the field of computer simulation of polymers. It is very clear that coarse-graining is an exciting conceptual and algorithmic challenge in the field of computer simulation and statistical mechanics. It is an approach that is providing a great step forward in the molecular modeling and simulation of real, complex systems. Thus, the first aim of this thesis was to develop a new simulation package designed specially for the coarse-grained (CG) simulations.¹ In the next step we studied the transferability of the CG force fields to different thermodynamic conditions.^{2,3} As an application, we used the CG model of polyamide-66 to investigate the effect of hydrogen bonds in structure and dynamics of the CG simulations with comparing with the atomistic results.^{4,5} To understand better the different properties of polymers with higher resolution, in the last part of this dissertation an easy and fast way to equilibrate dense polymer melt has been developed.⁶

Although coarse-grained (CG) models provide a highly efficient computational tool for rapidly investigating different properties of the system with a desired resolution, they face a number of significant challenges before they can become widely utilized by the research community, especially by experimental researchers as a tool to help interpret their experiments.

As it is discussed in chapter 3, the structure-based CG models are state-point dependent, which means that the potentials obtained at given thermodynamic condition do not generally provide a good description of the structure and other properties at other conditions. Thus, one needs to test the transferability for each CG model individually. Our results showed that for a defined mapping scheme, IBI potentials developed independently and with different shape, give comparable self diffusion coefficients for high enough temperatures. At high temperatures the specifics of a force field become unimportant and only global properties such as excluded volume and bead connectivity prevail. We have also shown that the *scaling factor* measuring the artificial speed-up of the CG model over the parent atomistic model depends on the simulation temperature. A key goal then is both to define and to *understand* what is and what is not transferable in a given CG model and why. Recent work by Harmandaris et al.⁷ showed that the dependence of the polymer dynamics on the density is not described accurately with the CG model, while the dependence on the chain length is same as in atomistic simulations. Thus, at high molecular weights where the change in the polymer dynamics is entirely due to the increase of the molecular weight we will have a constant scaling factor between the atomistic and the CG model. The asymptotic plateau value of the scaling factor allows us to quantitatively predict the diffusion coefficient (and of other dynamical properties) of higher molecular

weight polymer melts directly from the CG simulations. Since we have IBIsCO as a powerful tool for CG simulations, combining these results with the recent work of Qian et al.⁸ to control the fast dynamics in the CG models could lead to a robust way for calculating the viscosity of long polymer chains.

Another challenge involves the establishment of a proper formal connection between the behavior of the CG representation of the system and the underlying all-atom (full atomic resolution) model. In many systems, formation (e.g., self-assembly) and dynamics of large-scale structures and conformations cannot be decoupled from local, chemical processes and specific intermolecular interactions. A hydrogen bond (HB) is an attractive interaction acting between an electronegative atom (the acceptor) and a hydrogen atom bonded to a donor nitrogen, oxygen or fluorine. Due to the simplification of the CG models, the atoms directly involved in the HB (donor and acceptor) are usually “coarse-grained away” i.e. lumped with other atoms into beads. In chapter 5, we have shown that poorly described HB interactions can lead to an unphysical CG dynamics that prevents the correct description of the collective properties of the polymers. A method, which introduces explicitly an orientation-dependent coarse-grained HB potential, would allow to study those collective phenomena in materials that, driven by the presence of HBs, cannot be investigated with an atomistic approach. Polymer crystallization and self-assembly of block-copolymer could be a first object of investigation. As the HBs are the driving forces in many biological processes, the new force field could be particularly suitable for the study of biopolymers such as polysaccharides and biomaterials where a polymer interacts with a biological system.

The proposed coarse-grained model can also be used for the study of systems more complicated than bulk polymer melts. Possible examples are the study of the diffusion of a penetrant in a polymer matrix, or of block copolymers, blends, etc.^{9,10} In addition, the method can be directly incorporated in multiscale methodologies, which include multiple levels of simulation, and where both atomistic and mesoscopic descriptions are needed at the same time, but in different regions. An example is the study of the long time dynamics of polymers near solid attractive surfaces where an atomistic description is needed very close to the surface, whereas a mesoscopic description can be used for length scales far from the surface.¹¹

Even with the dynamic speedup gained by CG models, it is not trivial to obtain well-equilibrated structures of mesoscale polymeric systems, especially for long-chain molecules beyond a few entanglement lengths, for branched polymers, or for polymers at interfaces. Thus, preparing the initial relaxed configuration for the computer simulation of polymers is still a challenge. In chapter 6 it is proposed to use a direct reverse-mapping or fine-graining technique to generate an atomistic polymer structure directly from a generic polymer model. Future efforts could focus on the study of

the dynamic properties of these equilibrated long chain systems and on the application of the method to other systems considering of chains bearing short or long branches along the backbone.

7.1. References

- (1) Karimi-Varzaneh, H. A.; Qian, H.-J.; Chen, X.; Carbone, P.; Müller-Plathe, F. *In Preparation*, 2009.
- (2) Carbone, P.; Karimi-Varzaneh, H. A.; Chen, X.; Müller-Plathe, F. *J. Chem. Phys.* **2008**, *128*, 064904.
- (3) Qian, H.-J.; Carbone, P.; Chen, X.; Karimi-Varzaneh, H. A.; Liew, C. C.; Müller-Plathe, F. *Macromolecules* **2008**, *41*, 9919.
- (4) Karimi-Varzaneh, H. A.; Carbone, P.; Müller-Plathe, F. *J. Chem. Phys.* **2008**, *129*, 154904.
- (5) Karimi-Varzaneh, H. A.; Carbone, P.; Müller-Plathe, F. *Macromolecules* **2008**, *41*, 7211.
- (6) Carbone, P.; Karimi-Varzaneh, H. A.; Müller-Plathe, F. *Faraday Discussion 144* **2009**, *accepted*.
- (7) Harmandaris, V. A.; Kremer, K. *Macromolecules* **2009**, *42*, 791.
- (8) Qian, H.-J.; Liew, C. C.; Müller-Plathe, F. *Phys. Chem. Chem. Phys.* **2009**, *11*, 1962.
- (9) Merkel, T. C.; Bondar, V. I.; Nagai, K.; Freeman, B. D.; Pinnau, I. *J. Polym. Sci. Part B: Polym. Phys.* **2000**, *38*, 415.
- (10) Korsmeyer, R. W.; Meerwall, E. V.; Peppas, N. A. *J. Polym. Sci. Part B: Polym. Phys.* **1986**, *24*, 409.
- (11) Abrams, C. F.; Delle Site, L.; Kremer, K. *Phys. Rev. E* **2003**, *67*, 021807.

Appendix 1

Table A.1.1. Gaussian parameters of bond potential for the coarse-graining force fields of Polyamide-66.

$$P(\chi) = \sum_{i=1}^N A_i (2\pi w_i^2)^{-1/2} \exp\left(-\frac{(\chi - m_i)^2}{2w_i^2}\right)$$

<i>Bonds</i>	<i>N</i>	<i>i</i>	<i>Total area (A_i)</i>	<i>Width (Å) (w_i)</i>	<i>Center (Å) (m_i)</i>
A-M2	2	1	0.38	0.29338	3.03208
		2	0.63	0.13995	3.24873
A-M3	3	1	0.20613	0.31286	3.43678
		2	0.26622	0.1864	3.60964
		3	0.52661	0.13552	3.71412
M3-M3	3	1	0.15127	0.29519	3.33387
		2	0.1205	0.31809	3.67582
		3	0.71442	0.14379	3.91605
AP-M3	3	1	0.31543	0.14705	3.70972
		2	0.50737	0.24204	3.60195
		3	0.19874	0.37297	3.41251
M3P-A	3	1	0.2256	0.1417	3.88825
		2	0.53312	0.28631	3.75924
		3	0.24419	0.46014	3.53897

Table A.1.2. Gaussian parameters of angle potential for the coarse-graining force fields of Polyamide-66.

<i>Angles</i>	<i>N</i>	<i>i</i>	<i>Total area (A_i)</i>	<i>Width (degree) (w_i)</i>	<i>Center (degree) (m_i)</i>
A-M2-A	4	1	0.20184	41.2406	126.425
		2	0.405297	30.6180	156.021
		3	0.29043	8.82555	173.8283
		4	0.1	5.07947	176.4161
M3-A-M2	3	1	0.28737	32.24665	148.5638
		2	0.67387	30.95144	116.8712
		3	0.05177	16.50632	87.58377
M3-M3-A	3	1	0.52146	19.706	166.6254
		2	0.3914	30.8838	147.912
		3	0.13939	32.11339	116.771
M3-M3-AP	3	1	0.22138	13.0215	171.62913
		2	0.52826	24.93209	156.16492
		3	0.26723	37.46973	131.26766
M3P-A-M3	4	1	0.39227	34.77594	102.61543
		2	0.13791	20.0339	112.5837
		3	0.38033	28.93898	139.48177
		4	0.04972	13.9295	172.4121

Table A.1.3. Multiexponential Fitting Parameters for the A-A Intermittent ($C_{AA}^{atm}(t)$) and Continuous ($S_{AA}^{atm}(t)$) Hydrogen Bond Time Correlation Functions at 300, 400, 500 and 600 K calculated from atomistic simulations. The fitting function used is $f(x) = \sum_{i=1}^3 t_i \cdot \exp\left(-x/a_i\right)$ where t_i is the time constant and a_i is the amplitude.

temperature (K)	$C_{AA}^{atm}(t)$			$S_{AA}^{atm}(t)$		
	time constant (ps)	amplitude (%)	τ_R (ps)	time constant (ps)	amplitude (%)	τ_{HB} (ps)
300	16.72	1.78	8008	1.03	27.31	8.94
	0.31	13		15.55	55.50	
	396.61	85.22		0.20	16.40	
400	3051.14	3.54	2206	0.93	34.6	3.49
	0.21	16.42		7.09	44.17	
	26.85	80.04		0.19	20.37	
500	356.84	42.50	157	0.73	41.2	1.32
	0.63	35.5		2.90	33.74	
	26.27	22.0		0.18	23.96	
600	17.01	31.67	53	0.86	55.54	0.76
	0.67	48.11		3.56	6.21	
	235.54	20.22		0.21	36.6	

Table A.1.4. Multiexponential Fitting Parameters for the A-A Intermittent ($C_{AA}^{CG}(t)$) and Continuous ($S_{AA}^{CG}(t)$) Hydrogen Bond Time Correlation Functions at 300, 400, 500 and 600 K calculated from the CG simulations. The fitting function used is $f(x) = \sum_{i=1}^3 t_i \cdot \exp\left(-x/a_i\right)$ where t_i is the time constant and a_i is the amplitude.

temperature (K)	$C_{AA}^{CG}(t)$			$S_{AA}^{CG}(t)$		
	time constant (ps)	amplitude (%)	τ_R (ps)	time constant (ps)	amplitude (%)	τ_{HB} (ps)
300	859.45	24.95	228.46	1.72	52.09	1.17
	1.04	50.4		0.56	49.24	
	55.69	24.24				
400	491.91	7.15	41.33	1.92	14.25	0.82
	0.93	69.28		0.63	87.59	
	23.67	23.33				
500	112.42	12.26	16.03	1.59	9.97	0.64
	0.63	64.53		0.52	92.58	
	7.95	23.19				
600	141.43	8.80	14.29	2.43	1.51	0.53
	0.60	71.54		0.49	99.15	
	7.21	19.64				

Simulation Tools

The molecular dynamics simulations reported in this PhD thesis were performed on the cluster of the Theoretical Physical Chemistry group of Prof. Florian Müller-Plathe at the Technische Universität Darmstadt. The cluster was supplied by the company TRANSTEC. Additional molecular dynamics calculations were carried out on IBM p575 machines of Hessisches Hochleistungsrechner located at the Technische Universität Darmstadt.

For carrying out the atomistic molecular dynamics simulations the package YASP was used, which was originally developed by Prof. Florian Müller-Plathe and later parallelized by Dr. Konstantin B. Tarmyshov. The coarse-grained simulations have been done by using IBIsCO, which developed by myself and parallelized for distributed memory architectures using MPI.

Publications

Publications based on the present dissertation

1. H. A. Karimi-Verzaneh, H-J. Qian, X. Chen, P. Carbone, F. Müller-Plathe, “IBIsCO: A Molecular Dynamics Simulation Package for Coarse-Grained Simulations”, 2009 (in preparation)
2. P. Carbone, H. A. Karimi-Verzaneh, X. Chen, F. Müller-Plathe, “Transferability of coarse-grained force fields: The polymer case”, *Journal of Chemical Physics* **128**, 064904 (2008).
3. H. A. Karimi-Verzaneh, P. Carbone, F. Müller-Plathe, “Hydrogen Bonding and Dynamic Crossover in Polyamide-66: A Molecular Dynamics Simulation Study”, *Macromolecules*, **41** (19), 7211–7218, (2008).
4. H. A. Karimi-Verzaneh, P. Carbone, F. Müller-Plathe, “Fast dynamics in coarse-grained polymer models: the effect of the hydrogen bonds”, *Journal of Chemical Physics*, **129**, 154904 (2008).
5. P. Carbone, H. A. Karimi-Verzaneh, F. Müller-Plathe, “Fine-graining without coarse-graining: an easy and fast way to equilibrate dense polymer melts”, *Faraday Discussion* **144**, (2009). (accepted)
- 6*. H-J. Qian, P. Carbone, X. Chen, H. A. Karimi-Verzaneh, C. C. Liew, F. Müller-Plathe, “Temperature Transferable Coarse-grained Potentials for Ethylbenzene, Polystyrene and their Mixtures”, *Macromolecules*, **41** (24), 9919–9929, (2008).

* Not presented in this dissertation.

Acknowledgements

I would like to express my gratitude to all those who gave me the possibility to complete this thesis. Foremost, I would like to express my deep and sincere gratitude to my supervisor, Prof. Dr. Florian Müller-Plathe for the continuous support of my Ph.D study and research, for his patience, motivation, enthusiasm, and immense knowledge. His guidance helped me in all the time of research and writing of this thesis.

Besides my advisor, I owe my deepest gratitude to my colleague and friend, Dr. Paola Carbone, whose encouragement, guidance and support from the initial to the final level enabled me to develop an understanding of the subject. Without her my academic life could have been much lonely, and I look forward to a continuing collaboration with her in the future. My sincere thanks also go to Dr. Hu-Jun Qian and Dr. Xiaoyu Chen for their valuable discussions and help in programming. I want to express my gratitude to Prof. Balasubramanian for his hospitality and leading me working on diverse exciting projects. I would like to thank Prof. David Brown for providing GMQ code which was very helpful for writing IBIsCO. I wish to express my warm and sincere thanks to Mrs. Gabriele General for helping me in all administrative issues in the Technical University of Darmstadt and in settling my German social issues. I would like also to thank Dr. Michael Böhm and Miss. Sara Hadjiali for helping me to finalize this thesis. I would to thank Mr. Mohammad Alaghemandi for his assistances in numerous ways and suffering me during the last three years, and many thanks to my friends and all my colleagues for fine and warm working atmospheres and for all the fun we have had.

Last but not the least; I would like to thank my family for their understanding, endless patience, and encouragement when it was most required. I dedicate my thesis to my family and to my Angel, who is the essence of my life.

Curriculum Vitae

Personal Information

Name: Hossein Ali
Last name: Karimi Varzaneh
Place of birth: Varzaneh, Esfahan
Data of birth: 23/07/1981
Nationality: Iranian

School Education

1987-1992 **Shahid Torabiy School**, Varzaneh, Esfahan, Iran
Primary Student

1992-1995 **Shekh Jamalodin Asadabadi School**, Varzaneh, Esfahan, Iran
Secondary Student

1995-1999 **Enghelab Eslami School**, Varzaneh, Esfahan, Iran
Diploma Student

Higher Education

1999-2003 **Kashan University**, Kashan, Iran
Bachelor of Science Degree in Physics

2003-2006 **Institute for Advanced Studies in Basic Sciences**, Zanjan, Iran.
Master of Science in Physics

2006-2009 **Technical University Darmstadt**, Darmstadt, Germany
Theoretical Physical Chemistry, PhD student

Hossein Ali Karimi Varzaneh
Hiedenreich-Str. 44
64287 Darmstadt
Germany

Darmstadt, fri 22, May,2009

Erklärung

Ich erkläre hiermit, noch keinen Promotionsversuch unternommen zu haben.

(Hossein Ali Karimi Varzaneh)

Hossein Ali Karimi Varzaneh
Hiedenreich-Str. 44
64287 Darmstadt
Germany

Darmstadt, fri 22, May,2009

Eidesstattliche Erklärung

Ich erkläre hiermit an Eides Statt, dass ich meine Dissertation selbständig und nur mit den angegebenen Hilfsmitteln angefertigt habe.

(Hossein Ali Karimi Varzaneh)